

ABSTRACT

Title of Dissertation: **CASE STUDIES IN AGN FEEDBACK**

Robyn N. Smith
Doctor of Philosophy, 2022

Dissertation Directed by: **Professor Sylvain Veilleux**
Department of Astronomy

Galaxies in which the central supermassive black hole (SMBH) is actively accreting are referred to as active galactic nuclei (AGN) and are believed to play a crucial role in the evolution of both individual and clusters of galaxies. Empirically, the mass of the host galaxy and the mass of the SMBH are positively correlated. This is somewhat surprising given that the gravitational sphere of influence of the SMBH is orders of magnitude smaller than the host galaxy. The SMBH is believed to undergo periods of activity during which it is capable of powering galactic-scale outflows which in turn modulate star formation and therefore the overall mass of the host galaxy. Such processes are broadly referred to as feedback.

Clusters of galaxies are the largest gravitationally bound systems in the universe. The intracluster medium (ICM) in relaxed clusters is strongly centrally peaked and sufficiently dense that it is expected to cool rapidly (in cosmological terms). Such cooling should create streams of cool gas flowing to the brightest cluster galaxy (BCG) which in turn should fuel high rates of star formation. Little evidence of either has been found giving rise to the ‘cooling flow problem’. AGN are again invoked to explain the absence of this cooling flow. The BCGs hosting AGN, often with powerful radio jets, are believed

to inject energy into the ICM at a rate which can counteract the cooling. This cyclical nature of balancing the cooling is another form of AGN feedback.

In this thesis, we present case studies of three AGN which provide unique insight into these feedback processes. Chapter 2 presents evidence for a relativistic X-ray driven outflow on accretion disk scales in an ultraluminous infrared galaxy known to host a galactic-scale molecular outflow. The observational properties which make a galaxy an ideal candidate for detection of large-scale outflows are intrinsically at odd with the properties which are ideal for detecting small-scale outflows. IRASF05189-2524, the subject of Chapter 2, is one of only a handful of galaxies for which positive detection of outflows on both small- and large-scale exist.

Next, we turn our attention to AGN in BCGs and the cooling flow problem. Chapter 3 presents new *Chandra* observations of NGC 1275, the BCG in the famous Perseus Cluster. The high-cadence observing campaign finds X-ray variability on short intraweek timescales. The inclusion of archival observations reveals a general ‘harder when brighter’ trend. Examination of multiwavelength light curves finds a strongly correlated optical and γ -ray flare in late 2015 in which the optical emission leads the γ -ray emission by ~ 5 days. This robust ($> 3\sigma$) result is the first strong evidence of correlated emission with a time delay and lends support to the idea that the γ -ray emission is produced by synchrotron self-Compton upscattering.

In Chapter 4, we present new *Chandra* observations of the rare radio-quiet BCG quasar H1821+643. It is one of only two examples in the nearby universe of a highly luminous quasar with minimal radio jet activity at the center of a galaxy cluster. Despite observational challenges, we produce the first high-resolution spectrum of the quasar well-separated from the ICM in ~ 20 years. Our short-cadence observing campaign again reveals rapid variation on timescales corresponding to the light crossing time of the accretion disk. Although the flux varies, the spectrum is remarkably constant when compared to observations from previous decades.

The result of this thesis is to add to the existing body of knowledge of AGN feedback on both galaxy and galaxy cluster scales. These three AGN presented various observing challenges which required a combination of non-standard observational techniques and data reduction methods in order to maximize results with current X-ray instrumentation.

CASE STUDIES IN AGN FEEDBACK

by

Robyn N. Smith

Dissertation submitted to the Faculty of the Graduate School of the
University of Maryland, College Park in partial fulfillment
of the requirements for the degree of
Doctor of Philosophy
2022

Advisory Committee:

Professor Sylvain Veilleux, Chair/Advisor

Professor Christopher Reynolds, Advisor

Professor Richard Mushotzky

Professor Gordon Richards, External Examiner

Professor Gregory Sullivan, Dean's Representative

© Copyright by
Robyn N. Smith
2022

Preface

The research presented in this thesis is either published or in preparation for submission. Chapter 2 appears in *The Astrophysical Journal* as *IRASF05189-2524: Discovery of an X-ray Quasar Wind Driving the Cold Gas Outflow in the Ultraluminous Infrared Galaxy* (Smith et al., 2019) and is presented here with minimal modification. Chapters 3 and 4 are in preparation for submission. The NGC 1275 combined/time-averaged *Chandra* grating spectra described in Chapter 3 were also used in Reynolds, Smith et al. (2021) and Reynolds et al. (2020) for additional studies that are not reported in this thesis. The *Chandra* grating reduction pipeline developed for Chapter 3 was applied to archival *Chandra* data for H1821+643 and used by Sisk-Reynés et al. (2022) and Sisk-Reynés et al. (2022b, submitted) for studies not reported here.

Dedication

*To little girls who dream of doctorates
and the people who support them.*

Acknowledgments

A thesis does not occur in a vacuum, and there are many people with whom I share this accomplishment. I will forever be grateful to my advisor Professor Chris Reynolds for his unwavering belief in my abilities as a scientist, persistent patience, and endless words of encouragement. I would like to thank Professor Sylvain Veilleux for serving as the chair of my committee and for always pushing for a rigorous understanding of results while managing much of the logistics and paperwork associated with degree and department requirements. I would also like to acknowledge and thank Professors Stuart Vogel and Andy Harris not only for their steady leadership of the UMD Department of Astronomy but also for continually advocating for me and granting me a level of flexibility without which the completion of this thesis would not have been possible.

I'd like to thank Professor Gordon Richards for teaching me the art of writing a talk and what a healthy research group looks like in addition to his consistent support throughout both undergraduate and graduate school. Without the mentorship of Professor Sarah Gallagher, I may very well have dropped out of grad school in the first semester—thank you. Lastly, I would be remiss to leave out Mr. A, the science teacher who initially sparked my love for science and research.

Finally, the depth of my gratitude to my parents and grandmother knows no bounds for the amount of support and endless opportunities they provided. To my many friends in Philadelphia, thank you for welcoming me into your lives and inviting me on your

adventures. Lastly to Michelle and Maureen, who have always been there with food, somewhere to sleep, endless laughter, fulfilling conversations, and shoulders to cry on. I couldn't have done it without all of you.

Table of Contents

Preface	ii
Dedication	iii
Acknowledgements	iv
Table of Contents	vi
List of Tables	viii
List of Figures	ix
List of Abbreviations	xi
Facilities and Software	xiv
Chapter 1: Introduction	1
1.1 Supermassive Black Holes	1
1.2 What are Active Galactic Nuclei?	2
1.3 Motivation for AGN Feedback	3
1.3.1 The $M_{\text{BH}}-\sigma$ Relation & Radiative Feedback	5
1.3.2 The Cooling Flow Problem & Kinetic Feedback	6
1.4 AGN in X-ray	8
1.5 X-ray Instruments	9
1.5.1 CCDs	10
1.5.2 The <i>Chandra</i> X-ray Observatory	11
Chapter 2: IRASF05189-2524: Discovery of an X-ray Quasar Wind Driving the Cold Gas Outflow in the Ultraluminous Infrared Galaxy	18
2.1 Introduction	18
2.2 IRASF05189-2524	20
2.3 Observations and Data Reduction	22
2.3.1 <i>XMM-Newton</i>	22
2.3.2 <i>NuSTAR</i>	23
2.4 <i>XMM-Newton</i> Spectral Analysis	24
2.4.1 Broad-band Modeling	24
2.4.2 Modeling the Iron-K Region	27

2.4.3	Detailed Photoionization Modeling of the Fe K Absorber	34
2.4.4	Relativistic Reflection Model	35
2.5	<i>NuSTAR</i> Spectral Analysis	38
2.6	Discussion	42
2.6.1	Accretion Disk Wind	42
2.6.2	Connection with Galaxy-scale Outflows	46
2.7	Conclusions	49
2.8	Appendix: Outflow Energetics of the AGN Sample	51
Chapter 3: Correlated Variability in NGC 1275 at the Center of the Perseus Cluster		53
3.1	Object Overview	53
3.1.1	Radio Jet Structure	57
3.2	Observations and Data Analysis	61
3.2.1	New <i>Chandra</i> Observations	61
3.2.2	<i>Swift</i> XRT Archival Observations	68
3.2.3	<i>Fermi</i> LAT Observations	69
3.2.4	ASAS-SN Observations	72
3.3	X-ray Variability: The Disk-Jet Interplay	73
3.4	Correlated Variability Analysis	77
3.5	Discussion	85
3.6	Conclusions	87
Chapter 4: <i>Chandra</i> Study of Rare Brightest Cluster Galaxy Quasar H1821+643		89
4.1	Object Overview	89
4.2	New <i>Chandra</i> Observations	94
4.2.1	Data Reduction	95
4.2.2	Pileup Assessment	99
4.3	X-ray Light Curves	105
4.4	Time Series Analysis	112
4.4.1	Fractional Variability	113
4.4.2	Structure Function	115
4.5	Spectral Analysis	119
4.6	Discussion	127
4.6.1	Variability	127
4.6.2	Source Stability	127
4.6.3	Black Hole Mass Estimates	127
4.7	Conclusion	131
Chapter 5: Conclusions		132
5.1	Future Prospects	133
Bibliography		135

List of Tables

2.1	IRASF05189-2524 <i>XMM-Newton</i> and <i>NuSTAR</i> Observation Information	23
2.2	IRASF05189-2524 <i>XMM-Newton</i> Broad-Band Model Parameters	29
2.3	IRASF05189-2524 <i>XMM-Newton</i> 2-10 keV Model Parameters	33
2.4	IRASF05189-2524 <i>XMM-Newton</i> XSTAR Model Parameters	35
2.5	IRASF05189-2524 <i>XMM-Newton</i> <code>relxilllp</code> Model Parameters	39
2.6	Energetics of All Observed Outflows in IRASF05189-2524	45
2.7	Outflow Energetics of AGN Sample	51
3.1	NGC 1275 New <i>Chandra</i> Observations	62
3.2	NGC 1275 Archival <i>Swift</i> Observations	70
4.1	H1821+643 <i>Chandra</i> Observation Information	96
4.2	H1821+643 <i>Chandra</i> Flux & Photon Indices	107
4.3	H1821+643 X-ray Fractional Variability	115
4.4	H1821+643 Power Law Model Parameters	125
4.5	H1821+643 Relativistic Reflection Model Parameters	126
4.6	H1821+643 Black Hole Mass Estimates	130

List of Figures

1.1	Unification of AGN	4
1.2	The $M_{\text{BH}}-\sigma$ Relation	6
1.3	X-ray SED of AGN	9
1.4	ACIS Optical Blocking Filter Contamination	13
1.5	Sample ACIS HETG Dispersion Pattern	14
1.6	X-ray ASCA Grades	15
1.7	X-ray Pileup Spectra Example	16
1.8	X-ray Grade Migration	16
2.1	IRASF05189-2524 <i>XMM-Newton</i> EPIC Spectrum	25
2.2	IRASF05189-2524 <i>XMM-Newton</i> Broad-Band Model Residuals	28
2.3	IRASF05189-2524 <i>XMM-Newton</i> 2-10 keV Model Residuals in Iron Region	32
2.4	IRASF05189-2524 <i>XMM-Newton</i> XSTAR Model Residuals	36
2.5	IRASF05189-2524 Redshift of Iron Absorption	37
2.6	IRASF05189-2524 <i>NuSTAR</i> Spectrum	40
2.7	IRASF05189-2524 <i>XMM-Newton</i> & <i>NuSTAR</i> Joint Model Residuals	42
2.8	Outflow Velocity vs. Momentum Rate for AGN Sample	50
3.1	NASA Image of the Perseus Cluster	54
3.2	NGC 1275 Historical X-ray and Radio Light Curve	57
3.3	NGC 1275 Radio Structure Evolution	58
3.4	NGC 1275 Detailed Jet Structure	60
3.5	NGC 1275 Spectral Extraction Regions	64
3.6	NGC 1275 Background Renormalization	67
3.7	NGC 1275 Merged Image	68
3.8	NGC 1275 New <i>Chandra</i> Light Curve	73
3.9	NGC 1275 Flux vs. Γ	76
3.10	Blazar SED	77
3.11	Full Light Curve of NGC 1275 in Optical, X-ray, and γ -ray	78
3.12	DCF Results	79
3.13	NGC 1275 Light Curve with Correlated Variability	80
3.14	NGC 1275 γ -ray Light Curve PSD & PDF	82
3.16	Computed Time Lags from Simulated Spectra	84
3.17	New Jet Component Coincident with γ -ray Flare	88
4.1	H1821+643 <i>Chandra</i> Image with Radio Overlay	91

4.2	H1821+643 PSF Centroid Fitting	97
4.3	H1821+643 Source Extraction Regions	98
4.4	H1821+643 Spectral Pileup Assessment	100
4.5	H1821+643 Bad Grade Pileup Assessment	102
4.6	H1821+643 Grade 0 Spectrum	104
4.7	H1821+643 <i>Chandra</i> X-ray Light Curves	106
4.8	H1821+643 Structure Function	118
4.9	H1821+643 Spectral Data to Model Ratio	124

List of Abbreviations

'	arcminute
''	arcsecond
Å	angstrom
AAVSO	the American Association of Variable Star Observers
ACIS	Advanced CCD Imaging Spectrometer
AGN	active galactic nuclei
ALMA	Atacama Large Millimeter Array
APASS	the AAVSO Photometric All-Sky Survey
ARF	auxiliary response file
ASAS-SN	All-Sky Automated Survey for Supernovae
ASCA	Advanced Satellite for Cosmology and Astrophysics
<i>BBXRT</i>	Broad-Band X-ray Telescope
BHXR	black hole X-ray binary
BLR	broad line region
C-stat	Cash statistic
CALDB	calibration database
CCD	charged coupled device
CGRO	Compton Gamma Ray Observatory
CIAO	Chandra Interactive Analysis of Observations
CXC	<i>Chandra</i> X-ray Center
CXO	<i>Chandra</i> X-ray Observatory
DCF	discrete correlation function
EDSER	ACIS Energy-Dependent Subpixel Event Repositioning
EGRET	Energetic Gamma Ray Experiment Telescope
EPIC	European Photon Imaging Camera
ESA	European Space Agency
EW	equivalent width
<i>EXOSAT</i>	European X-ray Observatory Satellite

FIR	far infrared
FOV	field of view
FR I/II	Fanaroff-Riley type I/II
<i>HEAO</i>	High Energy Astrophysical Observatory
HEG	high energy grating
HETG	high energy transmission grating
HRC	high resolution camera
HRMA	high resolution mirror Assembly
<i>HST</i>	Hubble Space Telescope
IC	inverse Compton
ICM	intracluster medium
IFU	integral field unit
IR	infrared
ISCO	innermost stable circular orbit
ISM	interstellar medium
JAXA	Japan Aerospace Exploration Agency
M_{\odot}	solar mass
M_{BH}	black hole mass
MAGIC	Major Atmospheric Gamma Imaging Cherenkov Telescope
MARX	Model of AXAF Response to X-rays
mas	milliarcsecond
MEG	medium energy grating
MOS	metal oxide semi-conductor
NASA	National Aeronautics and Space Administration
NIFS	Near-infrared Integral Field Spectrograph
NIR	near infrared
NRL	narrow line region
<i>NuSTAR</i>	Nuclear Spectroscopic Telescope Array
PA	position angle
pc	parsec (kpc \rightarrow kiloparsec)
PDF	probability density function
PIMMS	Portable, Interactive Multi-Mission Simulator
PSD	power spectral density
PSF	point spread function

QSO	quasi-stellar object
RL	radio loud
RMF	response matrix file
rms	root mean square
<i>ROSAT</i>	Roentgen Satellite
RQ	radio quiet
SAS	science analysis system
SEC	synchrotron external Compton
SF	structure function
SMBH	supermassive black hole
SSC	synchrotron self-Compton
UFO	ultrafast outflow
UKIRT	United Kingdom Infrared Telescope
ULIRG	ultraluminous infrared galaxy
UV	ultraviolet
VERITAS	Very Energetic Radiation Imaging Telescope Array System
VLA	Very Large Array
VLBA	Very Large Baseline Array
VLBI	very long baseline interferometry
<i>XMM</i>	X-ray multi-mirror
XRT	X-ray Telescope
XSPEC	X-ray spectral fitting software
z	redshift
Z_{\odot}	solar metallicity

Facilities and Software

Facilities

1. ASAS-SN
2. *Chandra X-ray Observatory*
3. *Fermi Gamma-ray Space Telescope*
4. *Neil Gehrels Swift Observatory*
5. *NuSTAR*
6. *XMM-Newton*

Software

1. Astropy ([Astropy Collaboration et al., 2013, 2018](#))
2. CIAO ([Fruscione et al., 2006](#))
3. DELCgen ([Connolly, 2016](#))
4. FTOOLS ([NASA High Energy Astrophysics Science Archive Research Center, 2014](#))
5. marx ([Davis et al., 2012](#))
6. Matplotlib ([Hunter, 2007](#))
7. NumPy ([Harris et al., 2020](#))
8. pydcf ([Robertson et al., 2015](#))
9. SAOImageDS9 ([Joye & Mandel, 2003](#))
10. SAS (<https://www.cosmos.esa.int/web/xmm-newton/sas>)
11. SciPy ([Virtanen et al., 2020](#))
12. Sherpa ([Freeman et al., 2001](#))
13. XSPEC ([Arnaud, 1996a](#))
14. XSTAR ([Kallman & Bautista, 2001](#))

Chapter 1: Introduction

1.1 Supermassive Black Holes

It is now widely accepted that supermassive black holes reside in the centers of all massive galaxies (see e.g. [Kormendy & Richstone 1995](#)). Some of the most compelling evidence, both for the existence of black holes and their ubiquitous presence in galactic centers, was found in our own Milky Way Galaxy. Long-term monitoring of stellar orbits at the center of the Galaxy imply a central mass of $M = 4.3 \pm 0.01 \times 10^6 M_{\odot}$ ([Ghez et al., 2000](#); [Gravity Collaboration et al., 2022](#)). The high mass and small inferred spatial size ruled out suggested alternatives to black holes.

All black holes can be quantified by three properties—mass, angular momentum, and charge. Charge Q is a scalar quantity generally assumed to be $Q = 0$ since any charged astrophysical black hole would rapidly discharge to its environment. Angular momentum is a vector quantity, \vec{J} , more typically expressed as the dimensionless spin parameter $a = \vec{J}/M_{\text{BH}}$.

It is helpful to broadly split black holes into categories based on mass and accretion activity. Stellar mass black holes have typical masses ranging from $\sim 3 - 100 M_{\odot}$ and are believed to form from the collapse of massive stars. Supermassive black holes, the type that reside at the center of galaxies, have typical masses ranging from $\sim 10^5 - 10^{10} M_{\odot}$.

Understanding the formation of such massive black holes is very much an active area of research. Besides mass, we can consider whether or not a black hole is actively accreting matter. Those which are not are often referred to as quiescent, while those that are accreting matter are referred to as active. Black holes of any mass can be either quiescent or active with some cycling through periods of activity and quiescence on human timescales. The focus of this thesis will be on active supermassive black holes (SMBH) at the centers of other galaxies, referred to as active galactic nuclei (AGN).

1.2 What are Active Galactic Nuclei?

While black holes themselves do not emit any electromagnetic radiation, the energy released by accretion onto a black hole is immense. For AGN, this produces sufficient radiation to outshine the entire host galaxy with bolometric luminosities ranging from $\sim 10^{44} - 10^{48} \text{ erg s}^{-1}$. AGN are thus some of the most luminous and most distant observable objects in the universe.

Although not understood at the time, initial reports of objects that would be later considered AGN were identified via their strong, broad optical emission lines (Seyfert, 1943) and as bright radio point sources (e.g. Schmidt 1963). The former eventually became known as Seyfert galaxies and the latter QSOs for ‘quasi-stellar objects’. This early history hinted at the wide variety of observational characteristics across the entire electromagnetic spectrum that would eventually become associated with AGN.

The large number of observational characteristics in radio, infrared (IR), optical, ultraviolet (UV), X-ray, and γ -ray wavelengths which can be used to classify AGN resulted

in an extensive list of names and terminology, sometimes playfully referred to as an ‘AGN zoo’. A long-standing goal has therefore been a ‘unified model’ of AGN which can make sense of all of these properties in one coherent physical model (e.g. [Antonucci 1993](#); [Urry & Padovani 1995](#); [Netzer 2015](#); [Padovani et al. 2017](#)). This has been broadly accomplished by assuming we are looking at similar physical systems which are anisotropic and therefore appear very different when viewed from different angles.

Fig. 1.1 ([Beckmann & Shrader, 2012](#)) illustrates our understanding of a unified model of AGN. The core physical system is comprised of a central SMBH with a hot X-ray emitting corona (labelled as electron plasma in Fig. 1.1) and surrounding accretion disk. At a larger radius is a cool, dusty ‘torus’ and interspersed lie regions invoked to produce observed broad and narrow emission lines. Some AGN have radio jets. Note that those that do, are believed to have two symmetric jets; one jet is shown in Fig. 1.1 in order to include both jetted and non-jetted AGN in the diagram. Surrounding this physical model are the different viewing angles and the common AGN classifications associated with those viewing angles. This diagram is significantly over-simplified, particularly with regards to the exact nature and geometry of the corona, broad and narrow line regions, the torus, and the thickness of the accretion disk, but it provides a useful framework for further discussions.

1.3 Motivation for AGN Feedback

Powerful objects such as AGN must necessarily interact with their surrounding environment, and are believed to play a major role in the evolution of individual galaxies

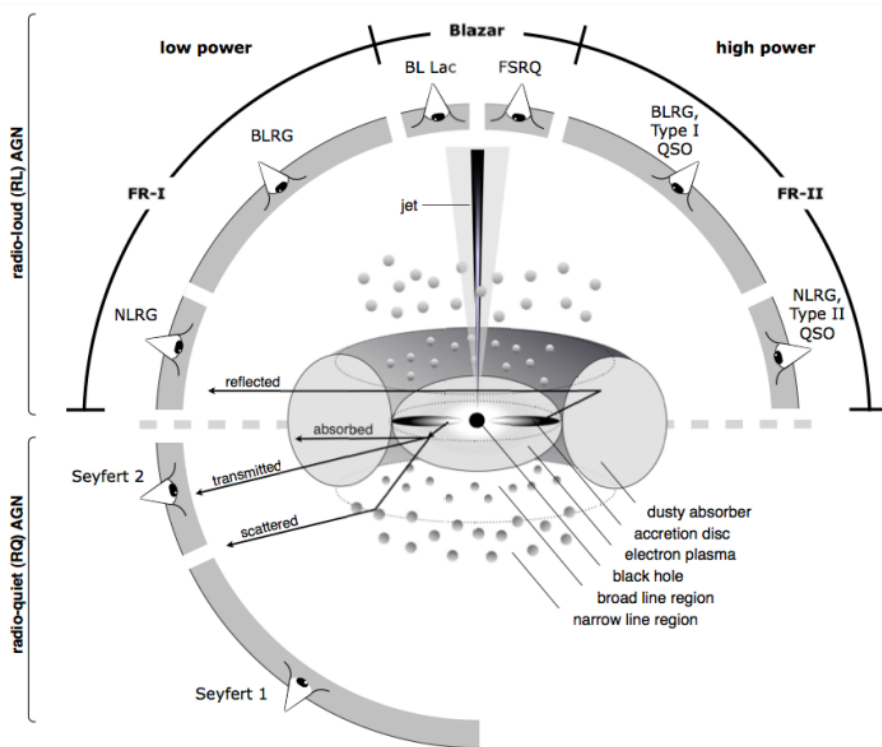


Figure 1.1: Illustration of the unified model of AGN reproduced from (Beckmann & Shrader, 2012). The core physical components of an AGN are the central black hole, corona (electron plasma), accretion disk, broad and narrow line regions, dusty torus, and optional radio jets. Note that AGN with jets are expected to have two symmetrical jets. Different viewing angles are labelled with their corresponding AGN classifications.

and galaxy clusters. The interaction of AGN with their host galaxy or galaxy cluster is broadly referred to as ‘feedback’. Below, we discuss the two most common types of feedback and the types of objects in which they are thought to occur.

1.3.1 The $M_{\text{BH}}-\sigma$ Relation & Radiative Feedback

Empirical studies revealed that the mass of the central SMBH is positively correlated with the mass of the bulge of the host galaxy (e.g. [Ferrarese & Merritt 2000](#); [Gebhardt et al. 2000](#)). This correlation is referred to as the $M_{\text{BH}}-\sigma$ relation and is shown in Fig. 1.2 (reproduced from [McConnell & Ma 2013](#)). Such a relationship is surprising given the many orders of magnitude that exist between the sub-parsec sphere of influence of the SMBH and the kiloparsec scale influence exerted by the host galaxy.

A leading explanation for the co-evolution of the SMBH and the host galaxy is via radiative mode (also quasar or wind mode) AGN feedback (see [Fabian 2012](#), [King & Pounds 2015](#), and references therein). In this picture, accretion onto the SMBH drives a fast outflow which collides with the interstellar medium (ISM) and can result in driving cool gas from the host galaxy which would otherwise form stars. This cool gas, however, is the same gas fuelling accretion onto the AGN. By growing, the SMBH will eventually deprive itself of fuel, thus modulating both the growth of the SMBH and the host galaxy.

Evidence for fast and ultrafast outflows (UFOs) driven by the SMBH are seen in X-ray observations as highly ionized blueshifted absorption lines ([Tombesi et al., 2010](#)). Large-scale galactic winds are also observed via absorption lines in the infrared, optical, and UV (see [Veilleux et al. 2005](#) and references therein). It is difficult to determine

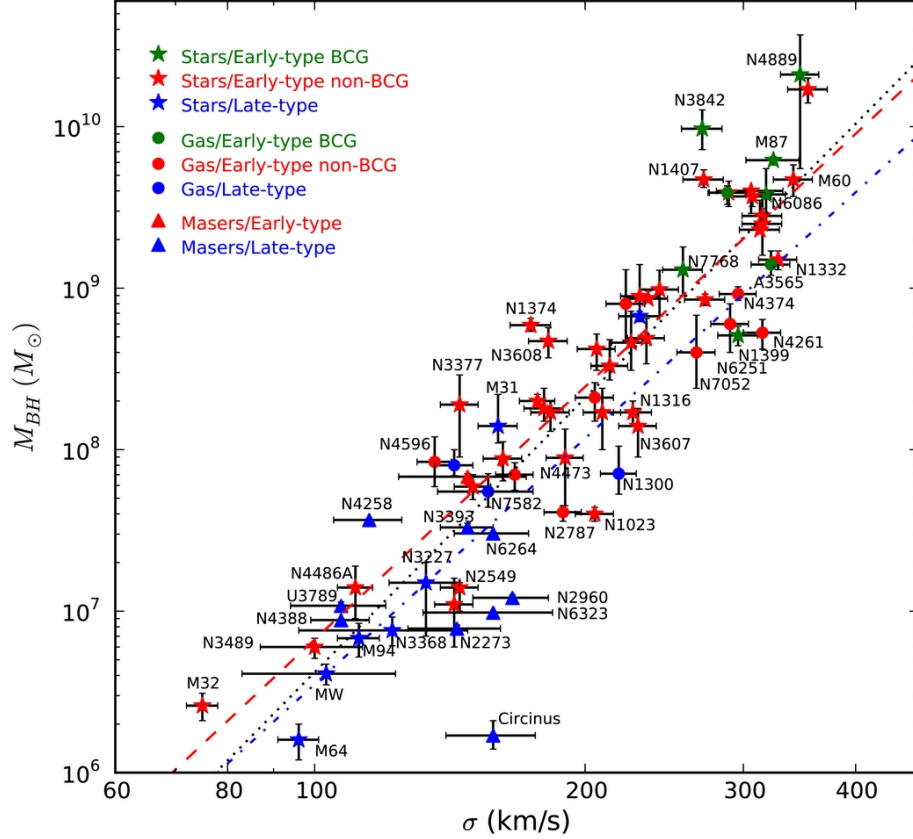


Figure 1.2: Positive correlation of the mass of the central SMBH and the mass of the bulge of the host galaxy as measured by stellar dispersion σ . Figure reproduced from [McConnell & Ma 2013](#).

whether these galactic winds are driven by SMBH outflows or by starbursts. Directly linking small- and large-scale outflows is challenging given that there are few objects in which X-ray and infrared absorption lines are simultaneously detectable. This discussion is continued in Chapter 2 which presents a study of one such object.

1.3.2 The Cooling Flow Problem & Kinetic Feedback

Galaxy clusters are the largest gravitationally bound objects in the universe. Roughly 50% of clusters are considered cool-core clusters where the intracluster medium (ICM) is characterized by a high density, low temperature core ($\sim 1-2$ keV; [Fabian 2012](#)) which

is strongly centrally peaked on the brightest cluster galaxy (BCG; [White et al. 1997](#); [Hudson et al. 2010](#); [McDonald et al. 2017](#)). The radiative cooling times of the ICM within the central 100 kpc of these clusters is cosmologically short ($< 10^9$ years) and led to predictions of massive cooling flows of gas into the BCG (see [Fabian \(1994\)](#) and references therein). X-ray observations revealed, however, that there is significantly less cool gas and star formation in the BCG than expected from such cooling flows ([Peterson & Fabian 2006](#); [Fabian 2012](#); [Liu et al. 2019](#)). This became known as the ‘cooling flow problem’. The leading solution to the cooling flow problem is that there must be a source heating the ICM.

The jetted radio-loud AGN frequently found in the BCG is believed to be the primary source of ICM heating via kinetic (also radio mode) feedback ([Fabian, 2012](#)). Observations show the jet interacting with the ICM via jet-blown bubbles ([Fabian et al. 2000](#); [Heinz et al. 2002](#); [Bîrzan et al. 2004](#)), sound waves and weak shocks ([Fabian et al. 2005](#); [Graham et al. 2008](#); [Million et al. 2010](#)), and AGN-driven turbulence ([Zhuravleva et al. 2014](#); [Hitomi Collaboration et al. 2016](#)). While it appears clear that the AGN is injecting heat into the ICM, it is less clear exactly how the AGN appropriately balances the cooling of the ICM. Presumably, if the AGN is fuelled directly from the ICM cooling process ([Allen et al. 2006](#); [Gaspari et al. 2013](#)) which in turn powers the jet, a self-regulated feedback loop could occur. New *Chandra* X-ray studies of BCG AGN are presented in Chapters 3 and 4.

1.4 AGN in X-ray

This thesis presents X-ray studies of AGN, thus it is relevant to briefly review the primary X-ray characteristics of AGN. X-ray flux is highly variable on short timescales implying that the emission region is located at small radii (Uttley & Mchardy 2004; Vaughan 2005). The X-ray spectrum is characterized by a hard power law, low energy soft excess, and a reflection component as shown in Fig. 1.3. The primary power law is attributed to the corona of hot electrons Compton upscattering optical and UV photons from the accretion disk. In photon units, the power law is described by a photon index ($dN/dE \propto AE^{-\Gamma}$) of $\Gamma \sim 1.9 - 2.0$ (Turner & Pounds, 1989). The reflection component is produced by the reprocessing of the power-law component by the accretion disk and other surrounding material. The main features of the reflection spectrum are the Compton hump around ~ 30 keV and an iron line around $E = 6.4 - 6.9$ keV. If the reflection is from in the inner regions of an accretion disk around a spinning black hole, then the reflection spectrum appears broadened and smeared. Even when we see a broadened iron line, there is often an additional narrow iron line at $E = 6.4$ keV corresponding to the $K\alpha$ fluorescence of neutral or low-ionization iron from larger radii. Finally, the origin of the soft excess is less understood, but may also be attributed to smeared reflection (Crummy et al., 2005) or smeared atomic or absorption lines (Czerny et al. 2003; Gierliński & Done 2004). It should be noted that not all components are seen in all sources or at all accretion states. Indeed, the presence or absence of such components are used to study properties such as black hole spin and the physical details of accretion onto SMBH.

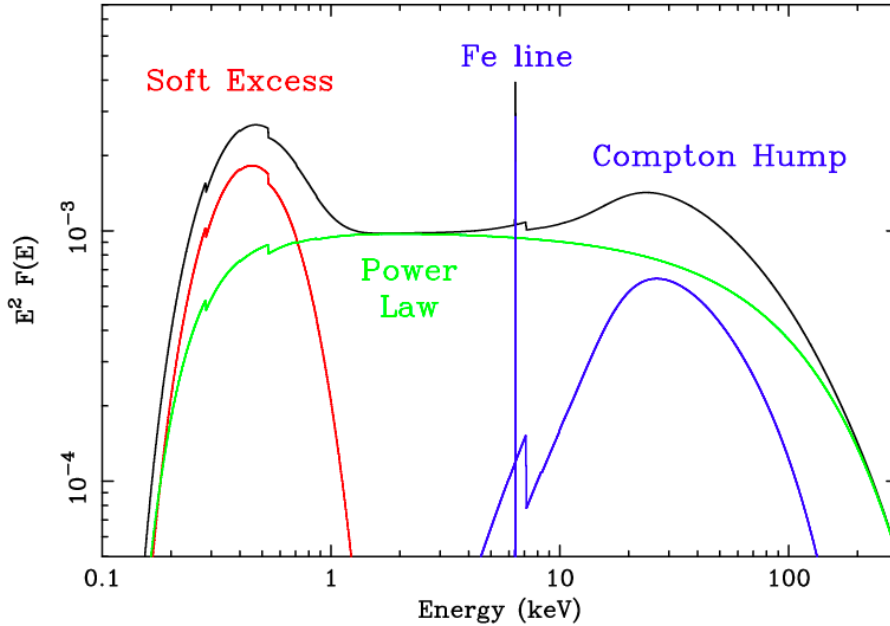


Figure 1.3: A typical X-ray SED of an AGN, reproduced from [Fabian 2006](#). The black line is the sum of components. The green line is the power law component attributed to the X-ray corona. The blue components are attributed to reflection and reprocessing of the corona from both the inner accretion disk and material at large radii. The red line is the soft excess whose origin is less understood, but may also be attributed to reflection.

1.5 X-ray Instruments

The study of astronomical X-rays provides unique technical challenges. Foremost, since the Earth's atmosphere blocks X-rays, all X-ray telescopes must be space-based. Secondly, the high-energy nature of X-rays requires a different optics approach. Visible light telescopes typically rely on mirrors which are positioned nearly perpendicular to incoming light. X-rays, however, are such short wavelength that they would be absorbed by such mirrors rather than being reflected and focused. To circumvent this issue, X-ray telescopes use series of nested parabolic and hyperbolic mirrors positioned such that incident photons just graze the reflective surface ([Wolter, 1952a,b](#)). The angle of incidence is roughly of order 1° or less. This type of mirror configuration produces a

focused image at a specific location in the telescope's field of view (FOV). Images formed away from the focal point suffer from noticeable aberrations that worsen as distance from the focal point increases.

1.5.1 CCDs

Having collected and focused the X-ray photons, we must detect them. Starting with the Advanced Satellite for Cosmology and Astrophysics (*ASCA*), launched in 1993, charge coupled devices (CCDs) have been the workhorse detector for X-ray astronomy. CCDs are sensitive photon detecting devices developed for the optical band in the 1970's and still used in most major observatory instruments today. A CCD is comprised of gate electrodes, an insulating layer, a photosensitive epitaxial silicon layer, and a bulk silicon substrate. Additionally, the CCD is divided into spatial elements called pixels which provide information about the location of incoming photons on the detector. When a photon strikes the photosensitive epitaxial layer, electrons can be produced via the photoelectric effect. The amount of photoelectrons produced (often referred to as an electron cloud) is measured as charge and, when used for X-ray detection, is directly proportional to the energy of the incident photon. Removal of an electron leaves behind a positive 'hole'. To prevent the negatively charged electron from recombining with the positive hole, gate electrodes apply an positive voltage to trap the photoelectrons in a potential well. Charges are permitted to accumulate for a given amount of time, called the integration or frame time, and are then transferred along adjacent pixels via alternating voltages in a 'bucket brigade' style read out process. Charges are often quickly transferred

to an inactive region of the CCD, the frame store, before being read out and stored by a local processor. The active portion of the CCD may return to observing while the frame store simultaneously reads out to the processor.

CCDs are considered front-illuminated when the gate electrode faces the source of light. In this position, incoming photons must pass through the gate structures before interacting with the photosensitive silicon. The gates may prevent some photons from being measured. Back-illuminated CCDs are flipped so that the bulk substrate is facing the light source. This requires most of the bulk substrate to be removed effectively resulting in directly exposing the photosensitive layer to incoming light. This does not result in a loss of photons as seen in front-illuminated CCDs, however, it can make back-illuminated CCDs slightly more sensitive to lower energy photons.

1.5.2 The *Chandra* X-ray Observatory

As a large portion of this thesis relies on technical knowledge of the *Chandra* X-ray Observatory (CXO), special consideration will be given to *Chandra* here in Chapter 1. *Chandra* launched on July 23, 1999 and is currently NASA's flagship X-ray telescope. The High Resolution Mirror Assembly (HRMA) is a Wolter-1 grazing incidence telescope consisting of four nested paraboloid-hyperboloid mirrors. A technical marvel, the mirrors are the smoothest and most precisely shaped mirrors ever created. *Chandra* has four instruments, the Advanced CCD Imaging Spectrometer (ACIS) and the High Resolution Camera (HRC), both of which can be used for imaging or high-resolution spectroscopy in conjunction with either the Low Energy Transmission Grating (LETG) or the High

Energy Transmission Grating (HETG). Further discussion will focus on ACIS and the HETG.

ACIS consists of ten CCDs split into two arrays: 1) ACIS-I has four CCDs in a 2×2 array used for imaging and 2) ACIS-S has six CCDs in a 1×6 array used for either imaging or spectroscopy with either the HETG or LETG. Each CCD is 1024×1024 pixels with each pixel corresponding to a size of $0.492''$. All of the ACIS-I CCDs are front illuminated. Four of the ACIS-S chips are front illuminated while two, including the chip with the aimpoint, are back illuminated. Since launch, the effective area of ACIS below 2 keV has continuously decreased due to build up of molecular material on the cold ACIS optical blocking filters. The HRC does not suffer from this due to its higher operating temperature. The effect of decreased effective area can be seen in spectra of calibration source Abell 1795 in Fig. 1.4. At this point, ACIS is no longer particularly sensitive below 0.5 keV but remains fully operational above 2 keV.

The ACIS-S array is specifically designed to work with the HETG, a slitless transmission grating spectrometer (Canizares et al., 2005). The HETG contains two gratings: the High Energy Grating (HEG; 0.8-10.0 keV) and the Medium Energy Grating (MEG; 0.4-5.0 keV). Although energy-dependent, the HETG provides an unparalleled resolving power ($E/\Delta E$) of 1000 at 1 keV and 660 at 0.826 keV for the HEG and MEG, respectively. Photons focused by the HRMA strike the gratings and are diffracted in one dimension by the dispersion angle β given by the grating equation

$$\sin(\beta) = \frac{m\lambda}{p} \quad (1.1)$$

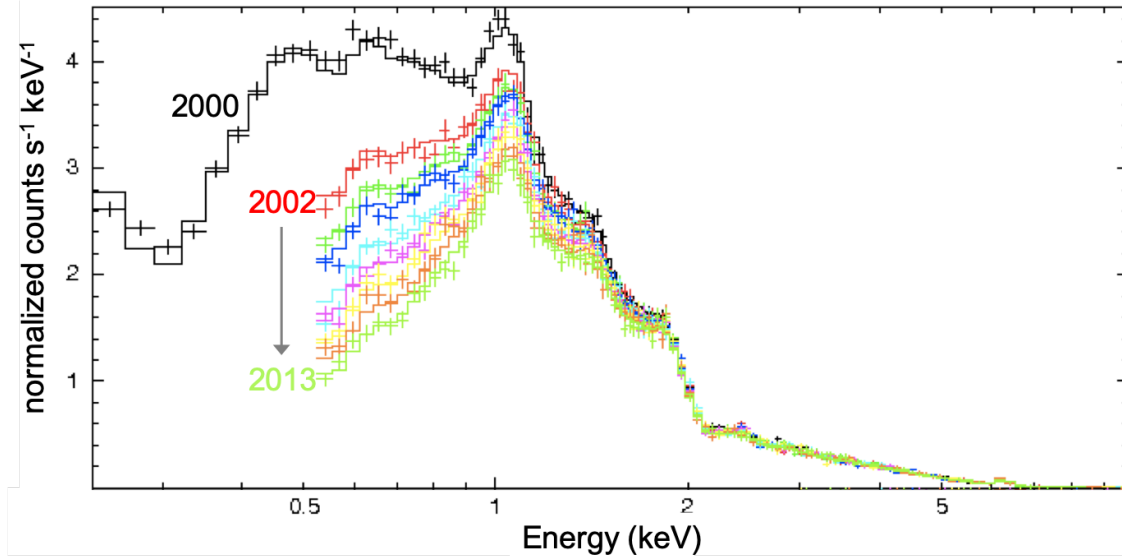


Figure 1.4: Observations spanning 13 years of calibration source Abell 1795 illustrate the decreased effective area of the ACIS detector below 2 keV due to the buildup of molecular contamination on the optical blocking filter. The instrument is not affected above 2 keV. Figure reproduced with modifications from [CXC POG, 2021](#).

where m is the integer order number of the spectrum, λ is the photon wavelength in angstroms, and p is period of the gratings. The period of the HEG grating is 2000.81 Å while the MEG is 4001.95 Å. The dispersed HETG spectra produce an ‘X’ shape (Fig. 1.5) on the CCDs with the HEG and MEG each producing spectra. An undispersed image ($m = 0$) is formed at the center of the dispersed spectra. Typical *Chandra* analysis utilizes the summed first order $m = \pm 1$ spectra. While the second and third order spectra have higher energy resolution, they typically do not have enough photons for a reasonable signal to noise ratio.

1.5.2.1 Pileup

Pileup is a form of saturation, a phenomenon present in all X-ray detectors, but will be discussed here using *Chandra* terminology. When a photon strikes the CCD and

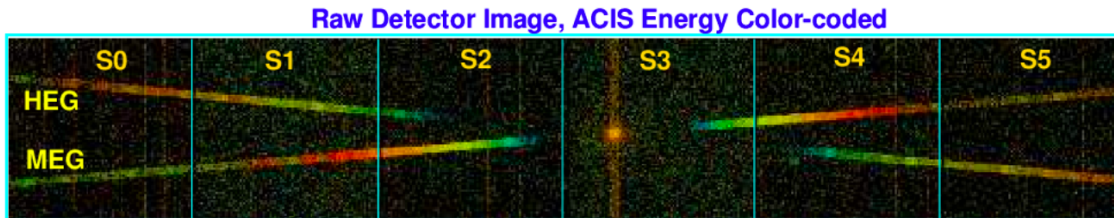


Figure 1.5: A colorized image of the HETG dispersed first order spectra on the ACIS-S detector (individual CCDs labeled as 'S#'). The HEG and MEG each produce a $m = \pm 1$ spectra (opposite sides of the 'X'). At the center is an undispersed zeroth order spectrum. The gratings produce second and third order spectra which are not visible due to their intrinsically lower intensity. Figure reproduced from [CXC POG, 2021](#).

interacts with the photosensitive silicon layer, the generated charge produces a variety of patterns. These patterns are graded and used to distinguish between astronomical sources of interest and sources of noise like cosmic rays. *Chandra* grades events based on 3x3 pixel “islands” centered on local charge maxima. The 256 possible grades are then binned into seven final grades which are used for event filtering. Grades 0, 2, 3, 4, and 6 are considered the set of ‘good’ grades for standard analysis in the sense that they are unlikely to be due to particle background events, cosmic rays, or other types of noise. Fig. 1.6 provides an example island for each of the seven final event grades.

Pileup occurs when two or more photons arrive in the same detector region within the same frame time and are read out as a single photon event (see e.g. [Ballet 1999](#); [Davis 2001](#)). This produces multiple noticeable and undesirable effects. First, the source spectrum is distorted and hardened—the registered energy is roughly equivalent of the sum of the individual photons thus shifting multiple lower energy photons to one higher energy photon. This can be referred to as energy migration. Second, the count rate is incorrectly measured as lower than its true value—instead of two or more photons measured per frame time, only one photon is measured per frame time. Fig. 1.7 illustrates

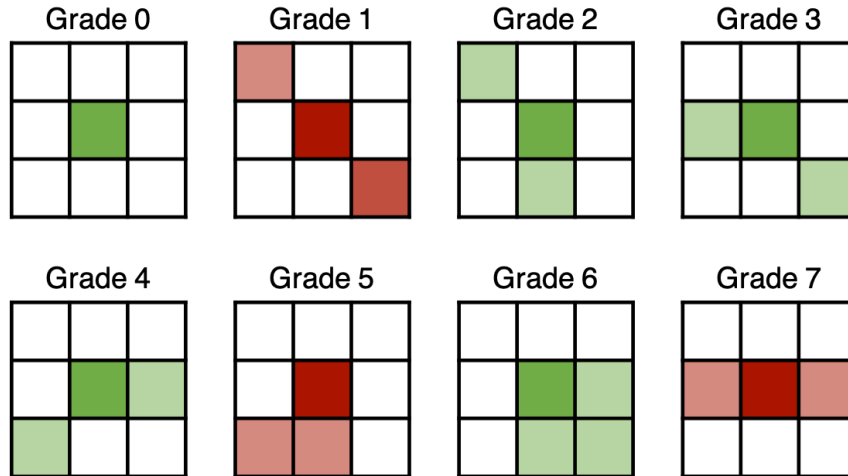


Figure 1.6: Samples of each of the 7 event grade classifications with good grades shown in green, bad grades shown in red. By definition, the brightest pixel is used to define the center of the 3x3 pixel island.

both of these concepts by the expected source spectrum to the measured source spectrum [Davis \(2001\)](#). Third, pileup causes a phenomenon referred to grade migration. [Fig. 1.8](#) illustrates how two photons which would individually produce good grades would instead be measured as a superposition of those good grades resulting in final classification as a bad grade. As true source photons are relegated to bad grades, they are removed from source analysis and result in incorrectly low flux estimations. Fourth, if pileup is sufficiently high, the piled up photons may be rejected entirely if the sum surpasses the on board energy threshold (~ 13 keV for *Chandra*) thus resulting in a image with a hole in the center (where pileup is always greatest) where no information is collected at all. Finally, pileup distorts the point spread function (PSF) of the source. Since pileup effects are most noticeable where the intrinsic count rate is highest, the center of the source is more highly piled up than the wings. Removing photons from the center of the PSF via pileup produces a PSF that is less strongly peaked and broader than the true PSF of the source.

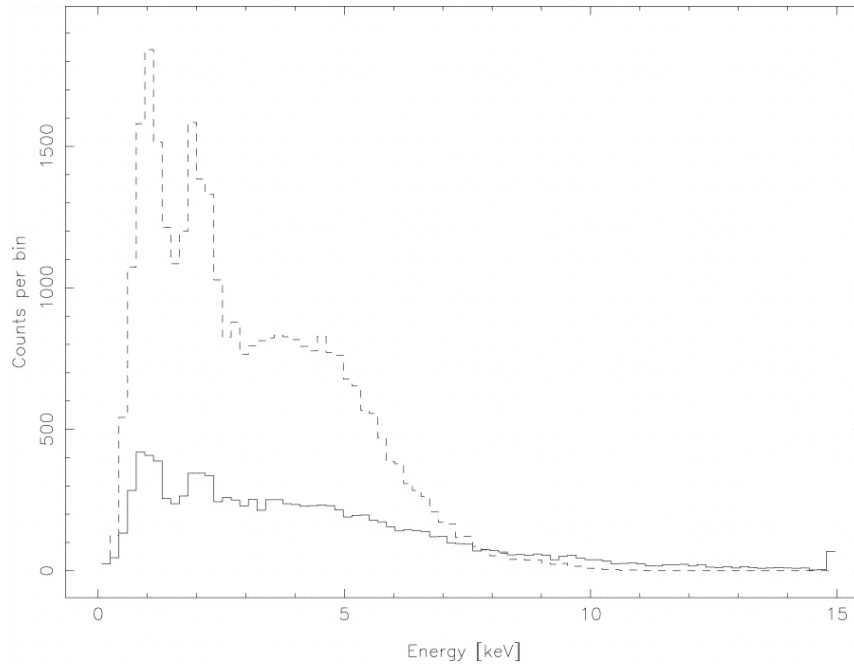


Figure 1.7: Examples of pileup on the X-ray spectrum of a quasar (Davis, 2001). Dashed lines indicate the predicted spectrum and count rates without pileup. Solid lines indicate the observed spectrum. The reduced count rate and high energy tail are direct results of pileup.

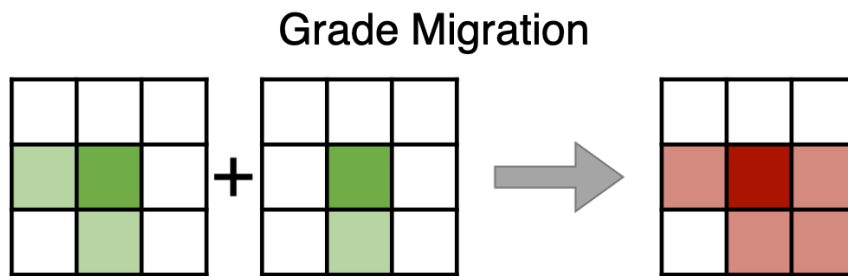


Figure 1.8: Visual guide to event grade migration caused by pileup. Two incident photons which would individually produce electron clouds corresponding to good event grades (green pixel islands at left). Instead, they strike the same region of the CCD within the same frame time and the combined electron cloud is recorded as one bad event grade and discarded.

In practice, it is not possible to avoid pileup for all sources, so various mitigation strategies are employed to produce the best results possible. Two of the most commonly used strategies with *Chandra* include using a subarray rather than the full detector or using the one of the transmission gratings. Using only a subarray of the detector reduces the frame time and thus the probability that two or more photons will arrive within that time. The transmission gratings effectively reduce the count rate by dispersing the incident photons. Less commonly used mitigation methods include continuous clocking mode—which produces the fastest frame and readout time but is only accomplished by moving from two spatial dimensions to one—and intentionally moving the source off-axis (away from the focal point) which spreads the counts out across a much larger PSF.

There exists no standard method for exactly quantifying the amount of pileup or exact spectral deformation caused by pileup. Often, one of the first indications of pileup is a trailed image, also called a read-out streak. It takes *Chandra* 40 μs to transfer accumulated charge from one row of pixels to the next. For a sufficiently bright source that is long enough for charge to accumulate as the pixels are being read out, thus producing measured charges along the column in which the center lies. Another way of diagnosing pileup is by examining the observed spectrum of the source. One proxy for estimating pileup is by calculating the ratio of bad grades to good grades throughout an image. Pileup is always worst at the core of the PSF. Comparing the grade ratio where there is known pileup to areas where there is assumed to be no pileup can indicate the severity of the grade migration and thus the amount of pileup. We return to a detailed discussion of pileup in Chapter 4 when presenting the analysis of new *Chandra* ACIS data for the bright quasar H1821+643.

Chapter 2: IRASF05189-2524: Discovery of an X-ray Quasar Wind Driving the Cold Gas Outflow in the Ultraluminous Infrared Galaxy

2.1 Introduction

In one possible evolutionary scenario, gas-rich galaxies merge together to form an obscured ultraluminous infrared galaxy (ULIRG) which evolves into a dusty quasar and then eventually an exposed optical quasar after shedding its gas and dust cocoon (e.g., [Hopkins et al. 2006](#); [Sanders et al. 1988](#); [Veilleux et al. 2002, 2009a,b](#)). This scenario may account for the intimate link between the mass of the stellar spheroid component of the host galaxy and that of the central supermassive black hole (SMBH) (e.g., [Ferrarese & Merritt 2000](#); [Gebhardt et al. 2000](#); [Silk & Rees 1998](#)) by invoking negative feedback of the active galactic nucleus (AGN) i.e. the AGN drives galactic winds which in turn may be able to quench the growth of both the SMBH and the stellar component of the host (e.g. [Fabian 1999](#); [King 2003](#); [King & Pounds 2003](#)).

Star formation is inhibited if the cold molecular gas out of which stars form is affected by such outflows. Far-infrared molecular spectroscopy of ULIRGs has revealed highly blueshifted absorption features indicative of high-velocity molecular outflows on scales of hundreds of parsecs which imply significant mass outflow rates ([González-](#)

[Alfonso et al., 2017](#); [Rupke et al., 2017](#); [Sturm et al., 2011](#); [Veilleux et al., 2017, 2013](#)).

Most models explaining the origin of these galactic outflows require a very fast ($v_{\text{out}} \sim 0.1c$) initial AGN accretion disk wind which shocks the surrounding interstellar medium (ISM) and forms a hot bubble which moves the molecular material (see [King & Pounds 2015](#) and references therein). The shock-driven galactic outflow can be divided into two distinct regimes: momentum-driven and energy-driven.

Momentum-driven outflows occur when the kinetic energy of the wind is mostly radiated away, in which case, only ram pressure exerts work on the surrounding ISM. Energy-driven outflows occur if the shocked ISM is not efficiently cooled and expands adiabatically as a hot bubble. The momentum rate of an energy-driven outflow is expected to be larger than that of a momentum-driven outflow and may approach values of $\dot{P} \simeq 10 L_{\text{AGN}}/c$ which is consistent with observations of several ULIRGs ([Cicone et al., 2014](#); [González-Alfonso et al., 2017](#); [Sturm et al., 2011](#)).

Galactic-scale outflows are common in U/LIRGs and often involve several gas phases: the molecular gas (e.g., [Fluetsch et al. 2019](#); [González-Alfonso et al. 2017](#); [Veilleux et al. 2013](#)), the neutral atomic gas ([Rupke et al., 2017](#); [Rupke & Veilleux, 2013](#); [Teng et al., 2013](#)), the warm ionized gas ([Rupke et al., 2017](#); [Rupke & Veilleux, 2013](#)), and sometimes even the hot ionized gas ([Liu et al. 2019](#); [Nardini et al. 2013](#); [Paggi et al. 2017](#); [Veilleux et al. 2014](#)). Conversely, outflows inferred from blueshifted Fe XXV/ XXVI absorption lines in the X-ray band at rest-frame energies $E > 7$ keV are observed in AGN at sub-parsec scales consistent with an accretion disk interpretation. These ultra-fast outflows (UFOs; [Gofford et al. 2013](#); [Longinotti et al. 2015](#); [Nardini et al. 2015](#); [Parker et al. 2017](#); [Tombesi & Cappi 2014](#); [Tombesi et al. 2011, 2010, 2015](#)),

have outflow velocities which are mildly relativistic ($v_{\text{out}} \sim 0.1c$). Confirming both a large-scale galactic outflow and sub-parsec scale accretion disk wind in the same object presents observational challenges requiring simultaneous detection of the outflow in the X-rays and at lower energies (mm-optical-IR).

IRAS F11119+3257 was the first such source in which both outflows were confirmed. Galactic outflows were found using OH absorption measurements with *Herschel* (Veilleux et al., 2013) and confirmed with CO(1–0) emission line measurements from deep *ALMA* observations (Veilleux et al., 2017). The UFO was initially detected with *Suzaku* (Tombesi et al., 2015) and later confirmed with *NuSTAR* observations (Tombesi et al., 2017). Mrk 231 is the second known object whose outflows were confirmed using *IRAM*, *Chandra*, and *NuSTAR* (Feruglio et al., 2015). Therefore, it is imperative to extend such studies to other sources in order to quantify the occurrence of such phenomena.

2.2 IRASF05189-2524

IRASF05189-2524 is a well-studied, nearby ($z = 0.0426$), late-stage merger ULIRG (Veilleux et al., 2002, 2006). It is an optical Seyfert 2 (Veilleux et al., 1999a), but contains hidden broad-line Pa β in the near-infrared (Veilleux et al., 1999b). With $\sim 70\%$ of its bolometric luminosity ($L_{\text{bol}} \sim 10^{12} L_{\odot}$) attributed to its AGN (Veilleux et al., 2009a), the AGN in IRASF05189-2524 is considered a quasar. A high-velocity, large-scale outflow has been detected in the neutral, ionized, and molecular gas phases (Bellocchi et al., 2013; González-Alfonso et al., 2017; Rupke et al., 2005, 2017; Teng et al., 2013; Veilleux et al., 2013; Westmoquette et al., 2012).

In the X-ray, IRASF05189-2524 is one of the brightest local ULIRGs. Archival *XMM-Newton* and *Chandra* observations derive an $E = 2\text{--}10$ keV continuum luminosity of $\sim 10^{43}$ erg s $^{-1}$ (Teng et al., 2009). The X-ray flux of IRASF05189-2524 is known to vary. The $E = 0.5\text{--}2$ keV flux was relatively constant during *XMM-Newton* observations in 2001 March, *Chandra* observations in 2001 October and 2002 January, and *Suzaku* observations in 2006 April. The $E = 2\text{--}10$ keV flux, however, was a factor of ~ 30 lower in the 2006 *Suzaku* than previously measured in the *XMM-Newton* and *Chandra* observations in 2001-02. In addition to the drop in flux, the 2006 *Suzaku* observation revealed a prominent $E = 6.4$ keV Fe K emission line not seen in the 2001-02 observations (Teng et al., 2009). Observations by *ASCA* in 1995 and *BeppoSAX* in 1999 found statistically significant unresolved iron line emission, but also confirmed strong continuum variability above $E = 2$ keV between the two observations (Severgnini et al., 2001). IRASF05189-2524 was observed by *NuSTAR* in 2013 February (21 ks) and October (25 and 8 ks) with a coordinated *XMM-Newton* observation during the 2013 October observation (31 ks; Teng et al. 2015). Minor flux variations detected between these observations were not found to be statistically significant, and the $E = 2\text{--}10$ keV flux was again consistent with the “high” state of the 2001-02 observations (Teng et al., 2015).

IRASF05189-2524 was detected by *Swift* BAT with a significance of 6σ at $E = 14\text{--}195$ keV and 4.2σ at $E = 24\text{--}35$ keV (Koss et al., 2013). In re-analyzing the 2013 *NuSTAR* and *XMM-Newton* observations, Xu et al. (2017) find that IRASF05189-2524 may be modeled above $E = 2$ keV by a broad iron line disk reflection. Xu et al. (2017) also find that possible features indicative of a high-velocity outflow in the Fe K band are not statistically required after the fit with a relativistic reflection dominated spectral

model. Data of higher quality are needed to confirm the possible existence of these spectral features.

2.3 Observations and Data Reduction

2.3.1 *XMM-Newton*

IRASF05189-2524 was observed by *XMM-Newton* for 98 ks on 2016 Sept. 6–7 (ObsID 0790580101). The observations were reduced using standard procedures with the *XMM-Newton* Science Analysis System v16.1.0. Soft proton flares were removed, and only single and double events were retained for the pn while single through quadruple events were retained for the MOS. The source was extracted using a 40'' radius circular region. The background was estimated from a source-free sky region of the same size. For the pn background, special care was taken to ensure that the background region was not located on parts of the CCD where there are known instrumental X-ray fluorescent lines (Freyberg et al., 2004), particularly the Cu-K α line around 8 keV. The final good exposure time for the pn was 74.3 ks. The MOS1 and MOS2 observations were reduced separately. Each MOS spectrum and light curve was inspected individually, and finding no gross variability between the two, they were combined using `epicspeccombine`. The final good exposure time for the combined MOS spectrum is 94.7 ks. Table 2.1 provides the final good exposure times and count rates for the *XMM-Newton* observation. The final spectrum for both the pn and MOS were grouped to a minimum of 50 counts per bin in order to ensure the use of the χ^2 statistics.

Table 2.1: Exposure times and count rates for *XMM-Newton* observation (ID 0790580101) and *NuSTAR* observation (ID 60201022002) of IRASF05189-2524.

Instrument	Exposure (ks)	Count Rate (0.5-2 keV)	Count Rate (2-10 keV ^a)
EPIC pn	74.33	0.393	0.315
EPIC MOS	94.71	0.251	0.212
FPMA (full)	144.1		0.067
FPMB (full)	143.9		0.061
FPMA (simultaneous)	45.39		0.073
FPMB (simultaneous)	45.31		0.066

^a Count rates for *NuSTAR* are calculated between 3–10 keV.

2.3.2 *NuSTAR*

IRASF05189-2524 was observed by *NuSTAR* for 144 ks on 2016 Sept. 5–8 (ObsID 60201022002). Spectra were created using HEASoft version 6.22 and CALDB version ‘20171002’ after initially producing cleaned event files with the tool `nupipeline`. For the screening parameters, we assumed “saacalc=2 saamode=optimized tentacle=yes” based on the *NuSTAR* SAA filtering report. From the cleaned event files, spectra and corresponding response matrices were then created using the `nuproducts` tool. The source region was chosen to be circular with a 60” radius, the background region was also circular with 121” radius. The resulting spectra have a net exposure of 144.1 ks for focal plane module (FPM) A and 143.9 ks for the FPMB. Due to differing orbits, the *NuSTAR* observation is only strictly concurrent with *XMM-Newton* for 45 ks. Table 2.1 provides the final good exposure times and count rates for the *NuSTAR* observation. All FPMA and FPMB spectra were grouped to a minimum of 25 counts per bin in order to ensure the use of the χ^2 statistics.

2.4 *XMM-Newton* Spectral Analysis

We perform our spectral analysis using XSPEC v12.10c (Arnaud, 1996b) using χ^2 statistics. All models take into account Galactic absorption with the `tbabs` model (Wilms et al., 2000) using a Galactic column density of $N_{\text{H,Gal}} = 1.66 \times 10^{20} \text{ cm}^{-2}$ (Kalberla et al., 2005). All parameters are given in the rest frame of IRASF05189-2524 ($z = 0.0426$). The full *XMM-Newton* EPIC spectrum of IRASF05189-2524 from 0.5–10 keV is presented in Fig. 2.1. All errors and limits are given at a level of 90% ($\Delta\chi^2 = 2.7$ for one degree of freedom). Statistical calculations were performed using XSPEC `error` and `steppar` commands avoiding local minima when searching χ^2 space. The difference in sensitivity of the pn and MOS spectra are due to the difference in effective area. The effective area of the MOS decreases more rapidly at higher energies than the pn.

2.4.1 Broad-band Modeling

We begin by joint modeling the EPIC pn and MOS spectra from 0.5–10 keV with a simple power law. This provides a poor fit ($\chi_{\text{red}}^2 = \chi^2/\nu = 11.93$) and is not considered further. The spectrum is indicative of a soft X-ray absorber (see Fig. 2.1), so our next model invokes a full covering neutral absorber (`zwabs` in XSPEC). While this provides a better fit ($\chi_{\text{red}}^2 = 6.47$), it is clear that the model is not accounting for any emission that is present at soft X-ray energies ($E < 2 \text{ keV}$) and is not considered further.

We then consider a neutral partial covering absorber (`zpcfabs`) which provides a significant improvement in the overall fit ($\chi_{\text{red}}^2 = 1501/948 = 1.58$; see Fig. 2.2a) although

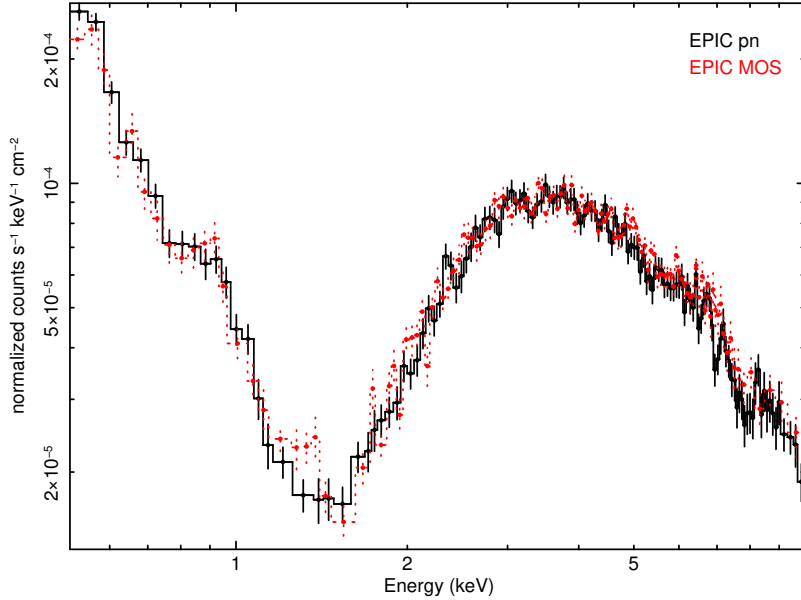


Figure 2.1: The *XMM-Newton* EPIC spectrum of IRASF05189-2524 from 0.5–10 keV in the rest frame ($z = 0.0426$). Additional binning has been applied for visual purposes.

there is still excess emission at soft energies. This model has a column density $N_{\text{H}} = (8.54 \pm 0.12) \times 10^{22} \text{ cm}^{-2}$, and the photon index, while high ($\Gamma = 2.29 \pm 0.01$), is not unreasonable given the large range of previously published values for IRASF05189-2524 (Ptak et al., 2003; Risaliti et al., 2000; Teng et al., 2015; Xu et al., 2017). We also test a continuum scattering model using two power laws with the same photon index, one with full neutral absorption and one with no absorption. The fit of this model is comparable to that with neutral partial covering absorption with no clear preference for either model. Although these models are phenomenologically distinct, they are mathematically equivalent, and we will continue our spectral analysis using neutral partial covering absorption.

Since IRASF05189-2524 is a ULIRG, we add a `mekal` component to account for the hot diffuse gas likely present in the host galaxy (see Fig. 2.2b). The best fitting `mekal`

component has a plasma temperature of $kT = 0.181 \pm 0.004$ keV while the neutral partial covering absorber has a column density of $N_{\text{H}} = (7.29 \pm 0.10) \times 10^{22} \text{ cm}^{-2}$. This improves the fit to $\chi_{\text{red}}^2 = 1050/946 = 1.11$ in addition to yielding a photon index of $\Gamma = 1.97 \pm 0.01$, much closer to the canonical value of $\Gamma = 2$ (e.g., [Nandra & Pounds 1994](#); [Reeves & Turner 2000](#)). Both neutral partial covering absorber models (with and without the `mekal` component) have a covering fraction of 98% with full covering excluded at the 90% level.

Next, we test an ionized partial covering absorber (`zxipcf`), which slightly improves the fit ($\chi_{\text{red}}^2 = 1034/945 = 1.09$; see Fig. 2.2c). The column density increases to $N_{\text{H}} = (11.06 \pm 1.10) \times 10^{22} \text{ cm}^{-2}$ with a low ionization parameter of $\log \xi = 0.59 \pm 0.05 \text{ erg s}^{-1} \text{ cm}$ and a covering fraction of 99% (full covering remains excluded at the 90% level). The plasma temperature of the `mekal` component decreases slightly to $kT = 0.147^{+0.016}_{-0.024}$ keV. Now, however, the continuum above $E = 8$ keV is noticeably underestimated (see Fig. 2.2c) while the photon index has steepened ($\Gamma = 2.49 \pm 0.12$). This is consistent with the ionized partial covering absorber compromising the continuum fit for the sake of the large contribution to the residuals at lower energies. For these reasons, we discard the model with the ionized partial covering absorber.

From the data-to-model ratios in Fig. 2.2, we find evidence for a possible absorption feature between $E \sim 7 - 8$ keV. We approximate this feature by adding a Gaussian to our model with a neutral partial covering absorber and `mekal` component (see Fig. 2.2d). The center of the line is located at $E = 7.81 \pm 0.10$ keV with a width of $\sigma = 103$ eV (90% upper limit $\sigma < 248$ eV) and an equivalent width of 56^{+37}_{-34} eV. This improves the fit by $\Delta\chi^2/\Delta\nu = 9/3$ which corresponds to a statistical requirement of 97% according to the

F-test ($> 2\sigma$). The column density is $N_{\text{H}} = (7.22 \pm 0.10) \times 10^{22} \text{ cm}^{-2}$, covering fraction is 98%, photon index $\Gamma = 1.94 \pm 0.01$, and plasma temperature $kT = 0.181 \pm 0.004 \text{ keV}$.

In our last broad-band model, we add an unresolved Gaussian emission line at $E = 6.70 \pm 0.06 \text{ keV}$ with a width frozen to $\sigma = 10 \text{ eV}$, consistent with iron K lines of highly ionized iron (Fe XVIII and above; [Kallman et al. 2004](#); see Fig. 2.2e). The addition of the emission line narrows the absorption feature to $\sigma = 78 \text{ eV}$ (90% upper limit $\sigma < 240 \text{ eV}$). The equivalent width of the absorption feature also decreases to $46^{+36}_{-39} \text{ eV}$ while the equivalent width of the emission feature is $35 \pm 17 \text{ eV}$. Using an F-test, the addition of a second Gaussian is statistically significant at a level of 99.7% ($\sim 3\sigma$). Other model parameters remain largely unchanged by the inclusion of an emission feature. The parameters of this best-fitting broad-band model ($\chi^2_{\text{red}} = 1028/941 = 1.09$) are presented in Table 2.2.

2.4.2 Modeling the Iron-K Region

To more closely model the iron-K region, we consider the pn and MOS only between $E = 2\text{--}10 \text{ keV}$, consistent with the methods presented in [Xu et al. \(2017\)](#) and [Braitto et al. \(2018\)](#). From Fig. 2.2, it is clear that the residuals are dominated by a complex array of features below $E = 2 \text{ keV}$, some of which may be due to a photoionized emitter. Modeling the soft X-ray emission does not impact results from the hard X-ray emission, although the inclusion of the softer energies may detrimentally influence the continuum estimation. Investigating the source of the soft X-ray emission is not our primary objective and is not

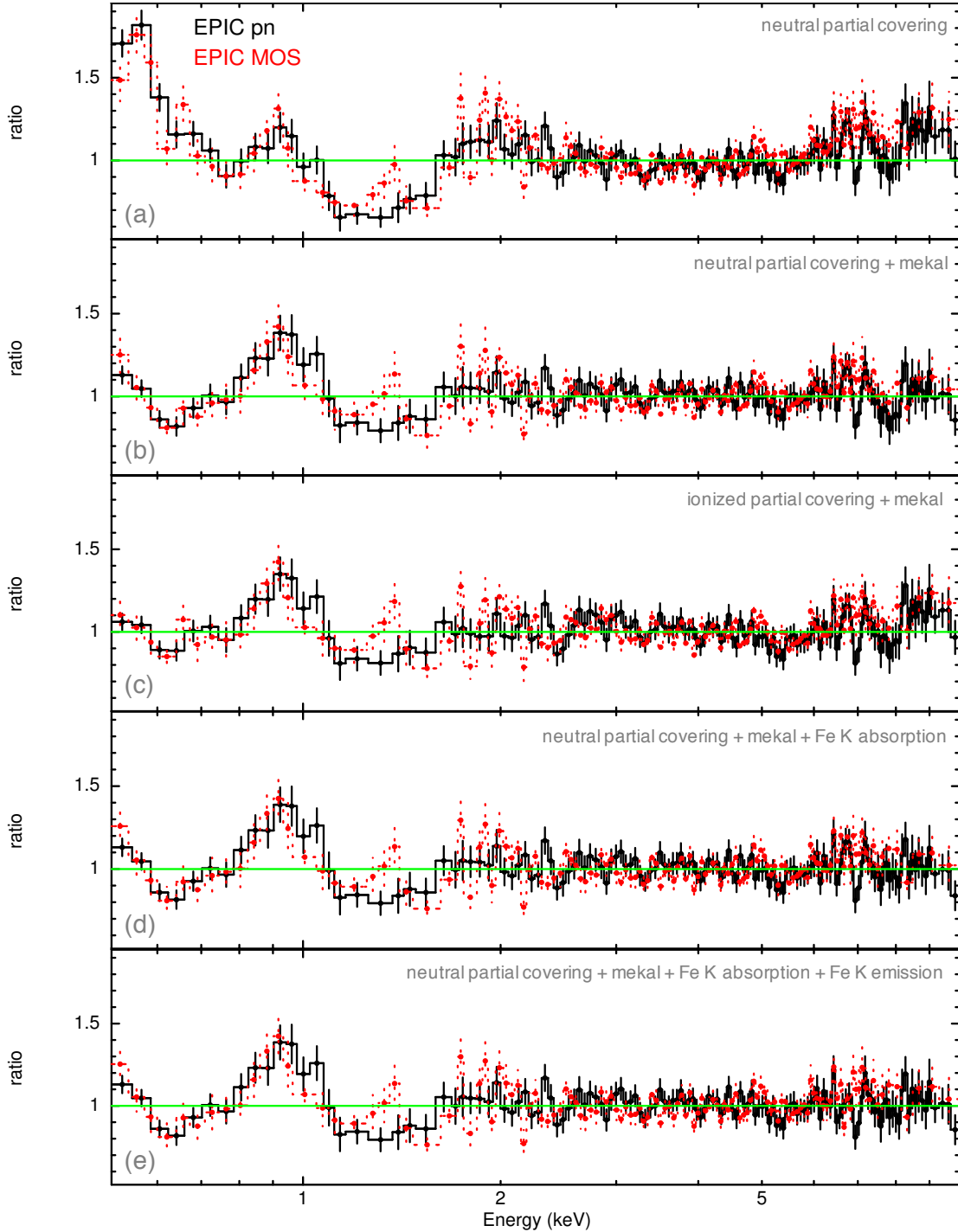


Figure 2.2: Data-to-model ratios for broad-band models; EPIC pn is plotted in black, the MOS in red. (a) a neutral partial covering absorber by itself does not account for excess emission below $E=1$ keV and underestimates the continuum above $E=8$ keV; (b) adding a mekal component to account for hot diffuse gas improves issues seen in (a); (c) testing a ionized neutral absorber results in an underestimate of the continuum above $E=8$ keV; (d) a Gaussian is added to (b) to model an absorption feature at $E=7.8$ keV; (e) a Gaussian is added to (d) to model an emission feature at $E=6.7$ keV.

Table 2.2: Parameters for the best-fitting broad-band model. All errors are given at the 90% level while limits are given at 90%.

Component	Parameter	Unit	Model	χ^2/ν	$\Delta\chi^2/\Delta\nu$
zpowerlw	Γ		1.97 ± 0.01	11334/950	...
	z^a		0.0426		
zpcfabs ^b	N_{H}	10^{22} cm^{-2}	7.26 ± 0.10	1933/948	9401/2
	Covering Fraction		0.984 ± 0.001		
	z^a		0.0426		
mekal	kT	keV	0.181 ± 0.004	1050/946	883/2
zgauss	Line E	keV	7.81 ± 0.06	1041/943	9/3
	σ	keV	<0.24		
	z^a		0.0426		
	EW	eV	-46^{+29}_{-36}		
zgauss	Line E	keV	6.70 ± 0.06	1028/941	13/2
	σ^a	keV	0.01		
	z^a		0.0426		
	EW	eV	35 ± 17		

^a Parameters frozen at their stated values.

^b The covering fraction for the neutral partial covering absorber is purely phenomenological; see §2.4.1 for information about a continuum scattering model.

considered further in this paper.

We begin modeling the iron-K region with a power-law continuum and a neutral partial covering absorber (see Fig. 2.3a). We do not include the `mekal` component, as it does not contribute above $E = 2$ keV. The column density is $N_{\text{H}} = (7.28^{+0.12}_{-0.27}) \times 10^{22}$ cm⁻² and the photon index $\Gamma = 1.94 \pm 0.02$. The covering fraction is 0.98 ± 0.01 .

Next, we add a Gaussian absorption feature at $E = 7.81 \pm 0.12$ keV with a width of $\sigma = 143^{+132}_{-98}$ eV and equivalent width of 72^{+42}_{-38} eV (see Fig. 2.3b). This improves the fit of the model ($\Delta\chi^2/\Delta\nu = 13/3$), and using an F-test, the addition is statistically significant at a level of 99.7% ($\sim 3\sigma$). The column density is $N_{\text{H}} = (6.96 \pm 0.12) \times 10^{22}$ cm⁻² and the photon index $\Gamma = 1.88 \pm 0.02$. The covering fraction is $0.984^{+0.014}_{-0.011}$ (full covering remains excluded at the 90% level).

Finally, we add a second Gaussian emission feature at $E = 6.70 \pm 0.06$ keV with a fixed width of $\sigma = 10$ eV (see Fig. 2.3c). This improves the fit of the model ($\Delta\chi^2/\Delta\nu = 9/2$), and using an F test, the addition is statistically significant at a level of 99.3%. The addition of a second Gaussian narrows the first Gaussian to $\sigma = 117$ eV (90% upper limit $\sigma < 257$ eV) and equivalent width of 61^{+40}_{-38} eV. The column density increases slightly to $N_{\text{H}} = (7.03^{+0.12}_{-0.29}) \times 10^{22}$ cm⁻² and the photon index steepens slightly to $\Gamma = 1.91 \pm 0.02$. The covering fraction remains at $0.984^{+0.014}_{-0.011}$ with full covering excluded at the 90% level. The final parameters for this best-fit model are provided in Table 2.3.

In order to better assess the significance of the detection of the Gaussian absorption feature at $E = 7.81$ keV, we run a series of detailed Monte Carlo simulations, according to the procedure described in Tombesi et al. 2010, quantifying the incidence of spurious lines when blindly searching for features between $E = 7$ -10 keV (rest frame). We adopt

the best fit model shown in Table 2.3 after removing the Gaussian absorption lines as our baseline model. We simulate a set of 1000 observations with both the EPIC pn and MOS detectors using the same observation times as given in Table 2.1 and grouping the spectra to a minimum of 50 counts per bin.

First, we fit the simulated data using our baseline model checking that the best fit values agree within the uncertainties with the input parameters used to generate the data. Then, we look for the probability of detecting an emission or absorption Gaussian feature between $E = 7-10$ keV due to random fluctuations of the simulated data. To do this, we add a Gaussian component to Model A with a line centroid restricted to fall between $E = 7-10$ keV in steps of 0.1 keV. The width of the Gaussian line is free to vary between $\sigma = 0-300$ eV. The line normalization is left free to vary during the fit between positive and negative values, thus allowing for the presence of emission or absorption features, respectively.

Using the value of $\Delta\chi^2 = 13$ as the threshold value, we find that 8 out of 1000 ($f = 0.008$) simulated spectra include spurious lines which improve the fit by a greater or equal amount. We derive the confidence level of the observed absorption line as $p = 1 - f = 0.992$, corresponding to 99.2% or 2.5σ .

The significant presence of an absorption feature above $E = 7$ keV could be indicative of an ultra-fast outflow. The strongest highly ionized iron transitions are Fe XXV He α ($E = 6.697$ keV) and He β ($E = 7.880$ keV) and Fe XXVI Ly α ($E = 6.966$ keV) and Ly β ($E = 8.250$ keV). For an absorption feature at $E = 7.8$ keV (rest-frame), only Fe XXV He α and Fe XXVI Ly α would produce an outflow with velocities of $v_{\text{out}} = 0.15c$ and $v_{\text{out}} = 0.11c$, respectively.

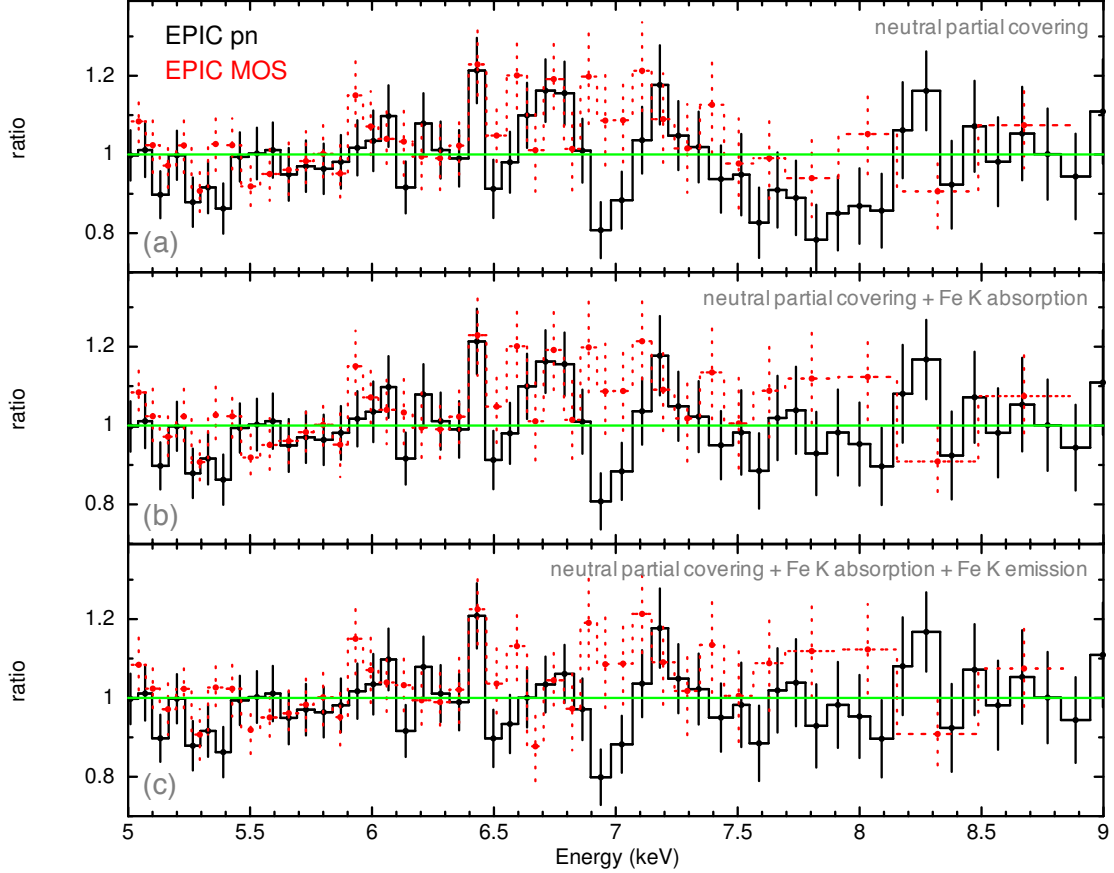


Figure 2.3: Data-to-model ratios for iron-K models ($E = 2\text{--}10$ keV); EPIC pn is plotted in black, the MOS in red. (a) a neutral partial covering absorber model; (b) an Gaussian absorption feature added at $E = 7.8$ keV which could be indicative of an ultra-fast outflow due to Fe XXV He α or Fe XXVI Ly α ; (c) a Gaussian emission feature added at $E = 6.7$ keV. Potential features at $E = 6.4$ keV, 6.95 keV, and 7.2 keV are not statistically significant.

We note an apparent narrow absorption feature at $E = 7$ keV. However, the EPIC pn and MOS data are not consistent at that energy, and any attempt to fit a Gaussian absorption feature is consistent with a width of $\sigma = 0$ eV. We conclude that this faint absorption feature may be due to random fluctuations. We also note apparent narrow emission features at $E = 6.4$ and 7.2 keV. These also are not statistically significant with the current data, but they are close to the expected energies for Fe K α and Fe K β . They will not be considered further here.

Table 2.3: Parameters for the best-fitting model from 2-10 keV. All errors are given at the 90% level while limits are given at 90%.

Component	Parameter	Unit	Model	χ^2/ν	$\Delta\chi^2/\Delta\nu$
zpowerlw	Γ		1.91 ± 0.02	4255/772	...
	z^a		0.0426		
zpcfabs ^b	N_H	10^{22} cm^{-2}	$7.03^{+0.12}_{-0.29}$	752/770	3503/2
	Covering Fraction		$0.984^{+0.014}_{-0.011}$		
	z^a		0.0426		
zgauss	Line E	keV	7.81 ± 0.12	739/767	13/3
	σ	keV	< 0.26		
	z^a		0.0426		
	EW	eV	-61^{+38}_{-40}		
zgauss	Line E	keV	6.70 ± 0.06	730/765	9/2
	σ^a	keV	0.01		
	z^a		0.0426		
	EW	eV	31 ± 18		

^a Parameters frozen at their stated values.

^b The covering fraction for the neutral partial covering absorber is purely phenomenological; see §2.4.1 for information about a continuum scattering model.

2.4.3 Detailed Photoionization Modeling of the Fe K Absorber

We perform a self-consistent photoionization modeling of the Fe K absorber using absorption tables generated with the photoionization code XSTAR (Kallman & Bautista, 2001) with standard solar abundances (Asplund et al., 2009). The output parameters of the XSTAR fit are the column density, ionization parameter, and the observed absorber redshift z_o . The ionization parameter is defined as $\xi = L_{\text{ion}}/(nr^2)$ erg s⁻¹ cm (Tarter et al., 1969), where L_{ion} is the ionizing luminosity from 1–1000 Ry¹ and r, n are the distance from the central source and the number density of the gas, respectively. The observed absorber redshift is related to the intrinsic absorber redshift in the source rest frame z_a as $(1 + z_o) = (1 + z_a)(1 + z_c)$, where z_c is the cosmological redshift of the source. The velocity can then be determined using the relativistic Doppler formula, $1 + z_a = [(1 - \beta)/(1 + \beta)]^{1/2}$, where $\beta = v/c$.

In order to best fit the observed width of the absorption feature, we consider three absorption tables with turbulent broadening velocities of 1000 km s⁻¹, 5000 km s⁻¹, and 10,000 km s⁻¹. All fits include the neutral partial covering absorber and a Gaussian emission line $E = 6.7$ keV. The XSTAR absorber well describes the observed absorption feature at $E = 7.8$ keV without the need for additional Gaussian components.

Our best-fit model has a $v_{\text{turb}} = 5000$ km s⁻¹. Model parameters are given in Table 2.4. Fig. 2.4 shows the data-to-model ratios of models with and without the XSTAR component. The redshift of the absorber is well constrained at $z_o = -0.071 \pm 0.012$ (see Fig. 2.5), which corresponds to an outflowing velocity of $v_{\text{out}} = 0.11 \pm 0.01c$. The

¹1 Ry $\equiv \frac{m_e c^4}{8\epsilon_0^2 h^2} = 13.6$ eV

Table 2.4: Parameters for the best-fitting XSTAR model. All errors are given at the 90% level while limits are given at 90%.

Component	Parameter	Unit	Model	χ^2/ν	$\Delta\chi^2/\Delta\nu$
zpowerlw	Γ		1.90 ± 0.02	4255/772	...
	z^a		0.0426		
zpcfabs ^b	N_{H}	10^{22} cm^{-2}	6.98 ± 0.11	753/770	3502/2
	Covering Fraction		$0.984^{+0.013}_{-0.010}$		
	z^a		0.0426		
zgauss	Line E	keV	6.70 ± 0.06	742/768	11/2
	σ^a	keV	0.01		
	z^a		0.0426		
	EW		-31^{+11}_{-50}		
XSTAR	N_{H}	10^{22} cm^{-2}	$26.7^{+22.5}_{-12.2}$	730/765	12/3
	$\log \xi$	$\text{erg s}^{-1} \text{ cm}$	$4.0^{+0.7}_{-0.1}$		
	z		-0.071 ± 0.012		
	v_{out}	c	0.11 ± 0.01		

^a Parameters frozen at their stated values.

^b The covering fraction for the neutral partial covering absorber is purely phenomenological; see §2.4.1 for information about a continuum scattering model.

ionization parameter of $\log \xi = 4.0^{+0.7}_{-0.1} \text{ erg s}^{-1} \text{ cm}$ indicates that the absorption feature is due to a mixture of both Fe XXV and Fe XXVI (Kallman et al., 2004). The covering fraction of the neutral partial covering absorber remains at $0.984^{+0.013}_{-0.010}$ with full covering excluded at the 90% level.

2.4.4 Relativistic Reflection Model

Using previous *XMM-Newton* and *NuSTAR* observations, Xu et al. (2017) found evidence for relativistic reflection. Although the lack of a clear broad Fe K emission line does not support interpreting the spectrum as dominated by relativistic reflection, we test

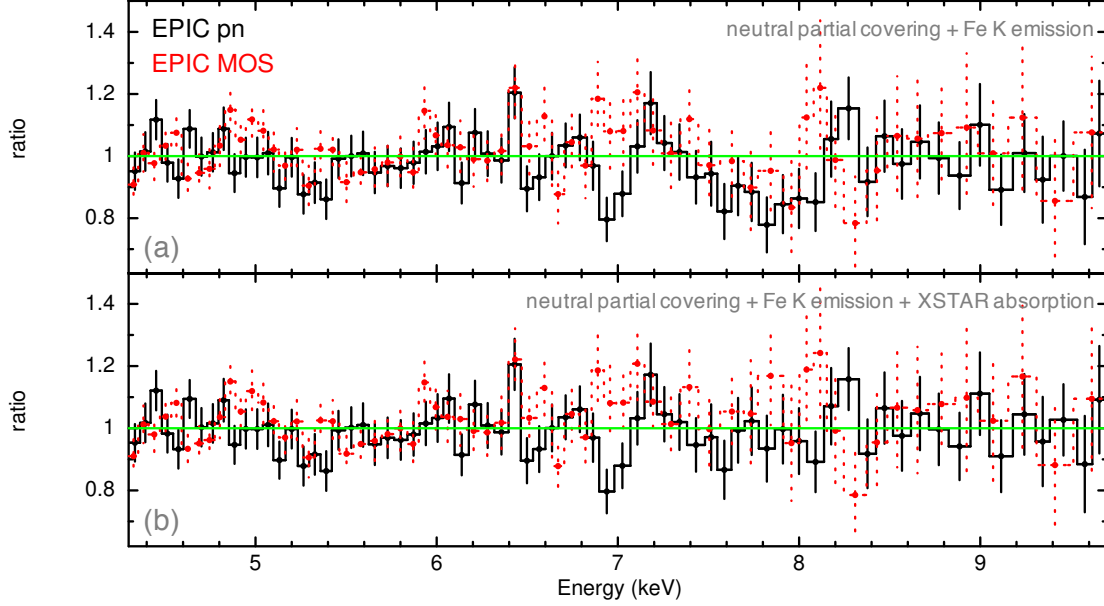


Figure 2.4: Model residuals are presented for two models which both include neutral partial covering and a Gaussian emission line at $E = 6.7$ keV. The model in the bottom panel includes an XSTAR absorption table which models the absorption feature at $E = 7.8$ keV.

that possibility in order to compare to the results presented in [Xu et al. 2017](#) by using the lamp-post geometry in the `relxill` code ([Dauser et al., 2014](#); [García et al., 2014](#)). This model (`relxilllp`) considers a lamp-post geometry in which the compact X-ray emitting source is located on the rotation axis of the black hole at a certain height specified in units of gravitational radii, $R_g = GM_{\text{BH}}/c^2$. The parameters of this model include: (1) h , the height of the source in R_g , (2) a , the dimensionless spin of the black hole, (3) i , the inclination with respect to the normal to the accretion disk, (4) R_{in} , the inner radius of the accretion disk, (5) R_{out} , the outer radius of the accretion disk, (6) z , the redshift of the system, (7) Γ , the power law index, (8) $\log \xi$, the ionization parameter of the accretion disk, (9) A_{Fe} , the iron abundance of the accretion disk, (10) E_{cut} , the observed high energy cutoff of the primary spectrum, (11) the reflection fraction (`refl_frac`), and (12) a model switch controlling the reflection fraction calculation (`fixReflFrac`).

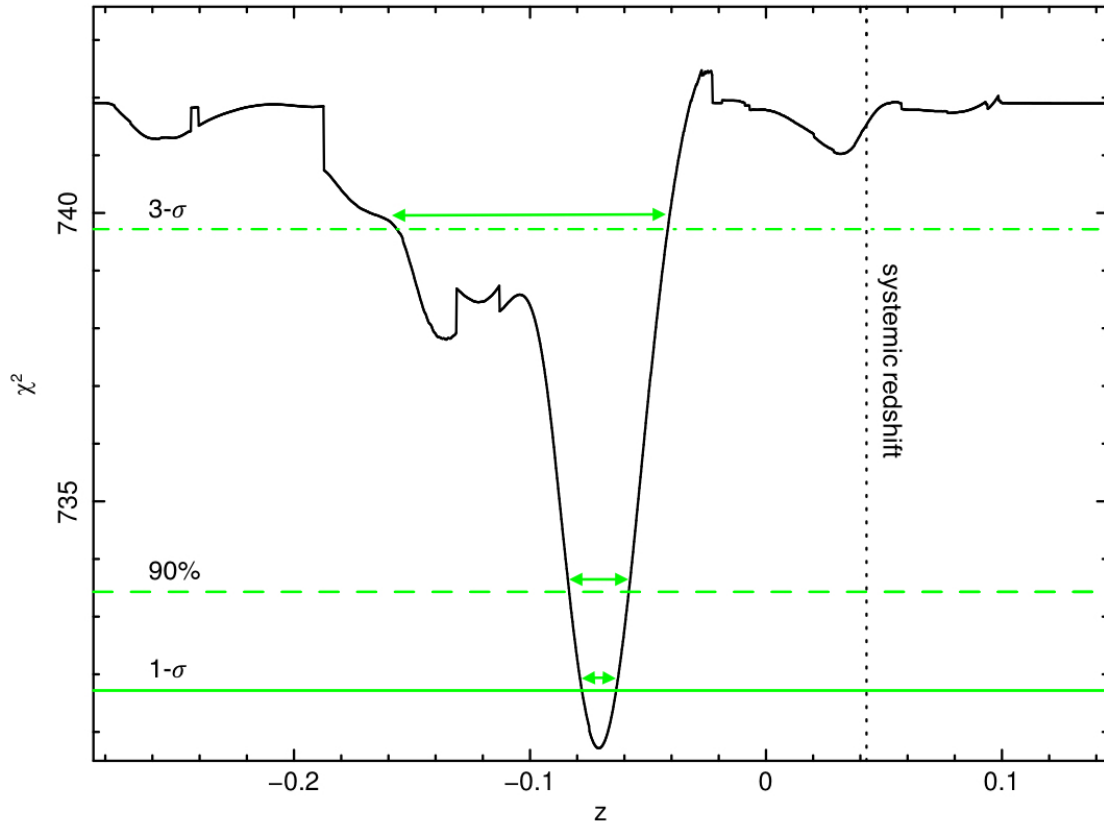


Figure 2.5: Using the XSPEC `steppar` command, the χ^2 statistic is plotted against the redshift of the XSTAR absorber modeling the Fe K absorption feature at 7.8 keV. The systemic redshift of IRASF05189-2524 ($z = 0.0426$) is shown with the vertical dotted line. The solid and dashed horizontal lines indicate the 1- σ , 90%, and 3- σ confidence ranges for the value of the redshift of the absorber, which is well-constrained at $z = -0.07$ in the observed frame corresponding to an outflowing velocity of $0.11c$.

We assume that the inner radius of the accretion disk extends to the ISCO and a typical outer disk radius of $R_{\text{out}} = 400 R_g$. During our analysis, models were not sensitive to the iron abundance, therefore, we fix the iron abundance at solar. We assume an energy cutoff $E_{\text{cut}} = 55$ keV, the value reported by [Xu et al. \(2017\)](#) whose spectral analysis extended to $E = 30$ keV. We set both the reflection fraction and the `fixRefFrac` switch to 1. Throughout our analysis, χ^2 was minimized by fixing the height of the illuminating source to $h = 2 R_g$, the minimum value permitted by the model.

A model including a neutral partial covering absorber and `relxilllp` provides a fit of $\chi^2/\nu = 741.5/767$. This is not statistically preferred over the models presented in §2.4.2 and §2.4.3 and is, in fact, worse than our model with an absorbed power law and iron K emission. We still provide full details of this best fit in [Table 2.5](#).

2.5 *NuSTAR* Spectral Analysis

We perform our spectral analysis using XSPEC v12.10c ([Arnaud, 1996b](#)) using χ^2 statistics. All models take into account Galactic absorption with the `tbabs` model ([Wilms et al., 2000](#)) using a Galactic column density of $N_{\text{H,Gal}} = 1.66 \times 10^{20} \text{ cm}^{-2}$ ([Kalberla et al., 2005](#)). All parameters are given in the rest frame of IRASF05189-2524 ($z = 0.0426$). All errors and limits are given at the level of 90% ($\Delta\chi^2 = 2.7$ for one degree of freedom). Statistical calculations were performed using XSPEC `error` and `steppar` commands avoiding local minima when searching χ^2 space.

The *NuSTAR* observation may provide a useful comparison for the results based on the *XMM-Newton* observation. However, we note that while *NuSTAR* may place

Table 2.5: Parameters for the best-fitting `relxilllp` model. All errors are given at the 90% level while limits are given at 90%. A full description of model parameters is given in §2.4.4.

Component	Parameter	Unit	Model	χ^2/ν	$\Delta\chi^2/\Delta\nu$
zpcfabs ^b	N_{H}	10^{22} cm^{-2}	7.29 ± 0.12	753/770	...
	Covering Fraction		$0.984^{+0.013}_{-0.009}$		
	z^{a}		0.0426		
relxillp	h^{a}	R_{g}	<16	742/767	...
	a		$0.62^{+0.13}_{-0.25}$		
	i	degrees	49 ± 4		
	R_{in}^{a}	R_{g}	-1		
	$R_{\text{out}}^{\text{a}}$	R_{g}	400		
	z^{a}		0.0426		
	Γ		1.94 ± 0.03		
	$\log \xi$	$\text{erg s}^{-1} \text{ cm}$	2.3 ± 0.5		
	A_{Fe}^{a}	solar	1		
	$E_{\text{cut}}^{\text{a}}$	keV	55		
	Reflection Fraction ^a		1		
	Fix Reflection Fraction ^a		1		

^a Parameters frozen at their stated values.

^b The covering fraction for the neutral partial covering absorber is purely phenomenological; see §2.4.1 for information about a continuum scattering model.

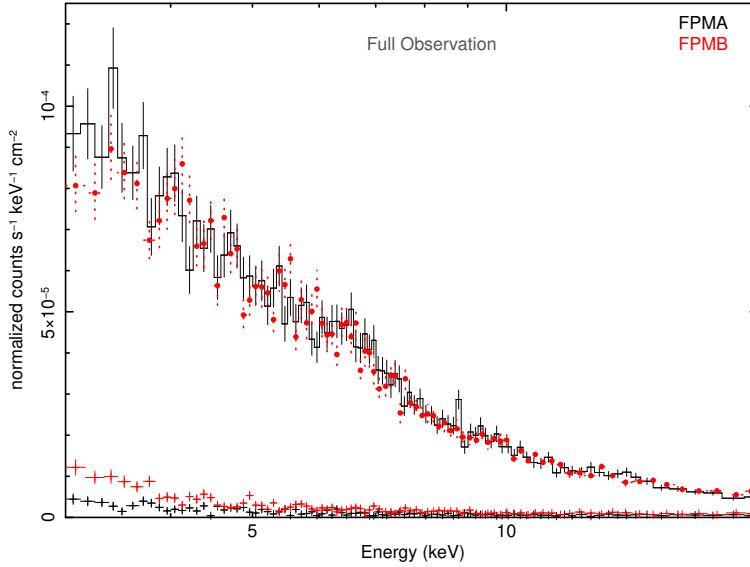


Figure 2.6: Spectra of the full *NuSTAR* observation between $E = 3 - 20$ keV (rest frame) with the FPMA and B shown in black and red, respectively. The background for each detector is also included.

helpful constraints on the high-energy continuum shape and broad spectral features, the energy resolution of *NuSTAR* is not well suited for the investigation of faint and narrow spectral lines like those found in the Fe K region of the *XMM-Newton* spectra. There is no unusually large flux variability over the course of the full *NuSTAR* observation, however it is important to keep in mind the likely variable nature of UFO absorption features (Matzeu et al., 2016). Features observed with *XMM-Newton* may or may not be present (or present with the same strength) during the *NuSTAR* exposure that is before and after the *XMM-Newton* observation. The spectra remain signal-dominated until $E = 20$ keV, but since our goal is to compare with *XMM-Newton*, we perform our spectral analyses in the mutual energy band from $E = 3-10$ keV (rest frame). Figure 2.6 shows the spectrum and background for the full *NuSTAR* spectrum.

Due to the short exposure time of the *NuSTAR* observation which is concurrent with *XMM-Newton*, the signal to noise is not sufficient to detect spectral lines. We therefore focus our analysis on the full *NuSTAR* spectrum. We begin our examination of the full *NuSTAR* spectrum by fitting the data with a power-law continuum and neutral partial covering absorber. Fig. 2.7 shows the ratio of this fit along with the *XMM-Newton* observation. We freeze the covering fraction of the neutral partial absorber to 0.984. This corresponds to the best fit value in models of the *XMM-Newton* observation (see §2.4) where the higher sensitivity in the soft energy band (i.e., $E < 3$ keV) provides tighter constraints on the covering fraction. Next, we add the two Gaussian features detected in *XMM-Newton*. Both the central energy values ($E = 7.8$ keV and 6.70 keV) and the widths ($\sigma = 0.12$ keV and 0.01 keV) of the Gaussian features were frozen to the values found in *XMM-Newton* because they are could not be constrained with *NuSTAR*. We do, however, allow the normalization of each Gaussian feature to vary between $[-1, 1]$ keV, thus allowing each Gaussian to be *either* an emission or absorption feature.

This model provides a reasonable fit to the data with a $\Delta\chi_{\text{red}}^2 = 1.03$. We find a steeper photon index of $\Gamma = 2.13 \pm 0.09$. The data are consistent with either an emission or absorption feature at the energy of $E = 7.81$ keV, with an equivalent width of 17.1 eV $^{+37.0}_{-40.7}$ eV. Note that at the 90% level, this is consistent with the *XMM-Newton* detection of an absorption feature, but the feature is not constrained in *NuSTAR* alone. The *NuSTAR* spectrum suggests an emission feature at $E = 6.70$ keV with an equivalent width of 75 eV ± 30 eV, also consistent with *XMM-Newton* at the 90% level.

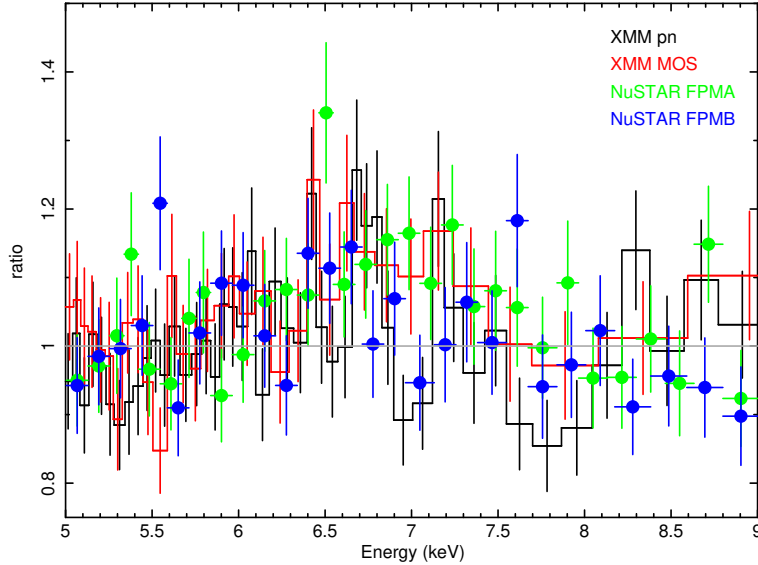


Figure 2.7: Model ratio of the full *NuSTAR* and *XMM-Newton* observations fit with a power-law and neutral partial covering absorber. Additional binning applied for visual purposes.

2.6 Discussion

2.6.1 Accretion Disk Wind

In §2.4, we report the analysis of the spectrum of IRASF05189-2524 with a new higher signal-to-noise *XMM-Newton* observation. We find that modeling the Fe K region of the spectrum with a self-consistent photoionization table generated with `XSTAR` indicates the presence of an outflowing accretion disk wind with a velocity of $v_{\text{out}} = 0.11 \pm 0.01c$.

We can estimate the energetics of the wind following the approach described in Tombesi et al. (2013, 2015, 2017). In our study of the energetics, we will use our best-fit model presented in §2.4.3 comprised of a neutral partial covering absorber, Gaussian Fe K emission line at $E = 6.7$ keV, and an `XSTAR` component modeling the Fe K absorption

feature at $E = 7.8$ keV.

There are multiple published values for the mass of the central SMBH in IRASF05189-2524². The photometrically derived black hole mass is estimated to be $M_{\text{BH}} = 20.8 \times 10^7 M_{\odot}$ (Veilleux et al., 2009b). Using the central velocity dispersions measured from the Ca II triplet line widths (Rothberg et al., 2013) and the $M_{\text{BH}} - \sigma$ relation (Tremaine et al., 2002), the mass is estimated to be $M_{\text{BH}} = 42 \times 10^7 M_{\odot}$ (Xu et al., 2017). Hereafter, we assume the black hole mass calculated in Veilleux et al. (2009b) $M_{\text{BH}} = 20.8 \times 10^7 M_{\odot}$ as a conservative estimate of the black hole mass and thus the X-ray wind energetics.

A lower limit on the radius of the wind can be derived from the radius at which the observed velocity corresponds to the escape velocity, $r_{\text{min}} = 2GM_{\text{BH}}/v_{\text{out}}^2 \simeq 5.08 \times 10^{15}$ cm. Converting to units of Schwarzschild radii ($R_{\text{S}} = 2GM_{\text{BH}}/c^2$), we obtain a wind launching radius $r \geq 83 R_{\text{S}}$ from the central SMBH. An upper limit on the radius of the wind can be derived from the definition of the ionization parameter (ξ) as long as the thickness of the absorber does not exceed its distance to the SMBH, $N_{\text{H}} \simeq n\Delta r < nr$ (e.g. Crenshaw & Kraemer 2012). This assumption is consistent with a disk wind observed close to its launching region. Using the XSPEC `lumin` command and an unabsorbed power law model, we calculate the ionizing luminosity between 1–1000 Ry to be $L_{\text{ion}} = 8.15 \times 10^{43}$ erg s⁻¹. Using the column density and ionization parameter from our best-fit model (Table 2.4) and the definition of the ionization parameter, we find $r_{\text{max}} = L_{\text{ion}}/\xi N_{\text{H}} = 3.05 \times 10^{16}$ cm or $r \leq 497 R_{\text{S}}$.

²Dasyra et al. (2006) derive a dynamical mass estimate of $M_{\text{BH}} = 2.95 \times 10^7 M_{\odot}$ using CO as a tracer of young stellar velocity dispersions. This method is now understood to systematically underestimate the black hole masses of actively star-forming galaxies like IRASF05189-2524 because the CO is tracing only the *young* stellar population rather than the older stellar population whose movement is more indicative of the central mass.

In calculating the energetics, we will only consider the lower limit on the radius of the UFO. Although the estimate of the upper limit is robust, it is far greater than the true location of the outflow. The mass outflow rate of the wind can be estimated considering the equation $\dot{M}_{\text{out}} = 4\pi\mu m_p r N_{\text{H}} C_{\text{F}} v_{\text{out}}$ where $\mu = 1.4$ is the mean atomic mass per proton, m_p is the proton mass, and C_{F} is the wind covering fraction (Crenshaw & Kraemer, 2012). Assuming spherical symmetry, the solid angle subtended by the wind is $\Omega = 4\pi C_{\text{F}}$. We conservatively assume $C_{\text{F}} \simeq 0.5$ estimated from the fraction of sources with detected UFOs and warm absorbers (e.g., Crenshaw & Kraemer 2012; Gofford et al. 2013; Tombesi & Cappi 2014; Tombesi et al. 2013, 2010). Using the range of launching radii calculated above, we find a mass outflow rate of $\dot{M}_{\text{out}} \gtrsim 1.0 M_{\odot} \text{ yr}^{-1}$.

Conservatively assuming that the outflow has reached a terminal velocity, the kinetic (or mechanical) power of the wind can be derived as $\dot{E}_{\text{K}} = \dot{M}_{\text{out}} v_{\text{out}}^2 \gtrsim 3.6 \times 10^{44} \text{ erg s}^{-1}$. The momentum rate (or force) of the wind is estimated to be $\dot{P}_{\text{out}} = \dot{M}_{\text{out}} v_{\text{out}} \gtrsim 2.2 \times 10^{35} \text{ dyne}$. IRASF05189-2524 has a bolometric luminosity $L_{\text{bol}} = 6.47 \times 10^{45} \text{ erg s}^{-1}$ of which 71% is attributed to the AGN ($L_{\text{AGN}} = 4.6 \times 10^{45} \text{ erg s}^{-1}$; Veilleux et al. 2009b). Comparing the wind energetics to the AGN luminosity, we find $\dot{E}_{\text{K}} \gtrsim 8\% L_{\text{AGN}}$ and $\dot{P}_{\text{out}} \gtrsim 1.4 L_{\text{AGN}}/c$. These calculated values are in line with those found in studies with larger samples of disk winds in Seyferts and luminous quasars (e.g., Fiore et al. 2017; Gofford et al. 2015; Nardini et al. 2015; Tombesi et al. 2012, 2015). The accretion disk wind is consistent with having a momentum rate comparable to the AGN radiation pressure, and the energetics are high enough to influence AGN feedback (e.g. Di Matteo et al. 2005; Gaspari et al. 2011; Hopkins & Elvis 2010).

Table 2.6: Location and energetics of the hot ionized disk wind (UFO) and multi-phase galaxy-scale outflows in IRASF05189-2524. Errors are reported when provided in the appropriate references. References: 1) [Smith et al. 2019](#); 2) [Fluetsch et al. 2019](#); 3) [González-Alfonso et al. 2017](#); 4) [Rupke et al. 2017](#).

Gas Phase	r_{wind}^a (pc)	v_{wind}^a (km s ⁻¹)	\dot{M}_{wind} (M_{\odot} yr ⁻¹)	\dot{P}_{wind} (10^{34} dyn)	$\dot{E}_{K,\text{wind}}$ (10^{42} erg s ⁻¹)	Reference
hot ionized	0.002–0.010	33,000 ± 3000	1.0–6.3	22–130	360–2150	1
neutral	3000	560	96 ⁺¹² ₋₆	59 ⁺⁹ ₋₄	38 ⁺⁷ ₋₃	4
warm ionized	3000	423	2.5 ^{+0.44} _{-0.69}	0.78 ^{+0.14} _{-0.22}	0.21 ^{+0.04} _{-0.05}	4
molecular (CO)	189	491	219	68	17	2
molecular (OH)						
low-velocity	170	200	120	16	1.6	3
high-velocity	340	550	150	52	14	3
total			269 ⁺¹⁹ ₋₁₃₁	68 ⁺¹⁴ ₋₃₀	16 ⁺⁴ ₋₇	3

^a Radius of wind used for calculation of energetics.

^b Velocities from Reference 1 are the average over all spaxels of the second component central velocity.

2.6.2 Connection with Galaxy-scale Outflows

Galaxy-scale outflows have been observed in IRASF05189-2524 in neutral, warm ionized, and molecular gas phases (Fluetsch et al., 2019; González-Alfonso et al., 2017; Rupke et al., 2017). Results from the relevant observations are included in Table 2.6. Energetics derived from the neutral and warm-ionized outflowing gas are based on the ground-based integral field spectroscopy (IFS) of Rupke et al. (2017). These observations are limited by the seeing ($\sim 1''$) which sets an artificial minimum radius $r \sim 400$ pc. The adopted radius for the neutral and warm-ionized gas are directly measured from IFS data and are virtually the same. However, a detailed inspection of the neutral and warm-ionized gas phases reveals that they differ in spatial distribution. Note that the warm ionized gas phase is negligible compared to the other phases of the large-scale outflow, so it will not be considered any further in our discussion.

The energetics for the molecular outflows are derived using OH and CO as tracers for H₂. OH absorption features are detected against the unresolved continuum emission in *Herschel* far-infrared spectra (González-Alfonso et al., 2017). The dimensions and energetics of the OH outflow are derived by carefully comparing the velocity profiles of four ground-state and radiatively excited transitions of OH and the predictions from spherically symmetric radiative transfer models. OH molecular tracers are sensitive to the dense molecular gas in the nucleus, so this gas component does not extend much beyond $r \sim 500$ pc. The CO energetics are derived from millimeter wave interferometry of spatially resolved CO emission lines, and the adopted radius is directly measured from these data (Fluetsch et al., 2019). As seen in Table 2.6, there is good agreement between

the different tracers. To simplify our discussion of the energetics, we take the average of the momentum rates for the neutral and two molecular outflows ($\dot{P}_{\text{out,av}} = 65 \times 10^{34}$ dyn) since these phases likely provide measurements of the same outflow at different epochs (i.e. distances from the center). We similarly take the average of the outflow velocity for the neutral, molecular CO, and high-velocity molecular OH outflows ($v_{\text{out,av}} = 534$ km s⁻¹).

To compare the energetics of the X-ray outflow with the galaxy-scale outflow, we consider two different ways to drive a galaxy-scale outflow. In the case of a momentum-driven outflow, we expect $\dot{P}_{\text{outer}} \simeq \dot{P}_{\text{inner}}$ where “outer” refers to the galaxy-scale outflow and “inner” refers to the inner X-ray wind (Faucher-Giguère & Quataert, 2012; Zubovas & King, 2012). In §2.6.1, we derive $\dot{P}_{\text{inner}} \gtrsim 22 \times 10^{34}$ dyn, while the momentum rate for the galactic scale outflows are consistently measured as $\dot{P}_{\text{outer}} \sim 65 \times 10^{34}$ dyn (Table 2.6). This gives $\dot{P}_{\text{outer}}/\dot{P}_{\text{inner}} \sim 3$, however, given the large uncertainties in the momentum rate estimates, our data are not inconsistent with a momentum-driving scenario.

For an energy-driven outflow, conservation of energy gives $\frac{1}{2}\dot{M}_{\text{inner}}v_{\text{inner}}^2 = \frac{1}{2}f\dot{M}_{\text{outer}}v_{\text{outer}}^2$ where “outer” refers to the galaxy-scale outflow and “inner” refers to the inner X-ray wind. The efficiency factor, f , is limited to $[0,1]$ where $f = 0$ and $f = 1$ are two extremes indicating either full dissipation or conservation of kinetic power within the outflow, respectively. Using the expression for the momentum rate, this can be rewritten as $\dot{P}_{\text{inner}}v_{\text{inner}} = f\dot{P}_{\text{outer}}v_{\text{outer}}$. Thus, the expected momentum rate for the large-scale outflow in an energy-driven outflow is given as $\dot{P}_{\text{outer}} = f(v_{\text{inner}}/v_{\text{outer}})\dot{P}_{\text{inner}}$. The efficiency factor can be interpreted as the ratio between the covering fractions of the inner and outer outflows or the fraction of the kinetic energy of the inner X-ray wind that

goes into bulk motion of the swept-up molecular material.

Using average values for the large-scale galactic outflows along with the lower limit of the momentum rate for the UFO, we obtain $f = 0.05$. This low efficiency value could be the result of a highly clumpy interstellar medium or if the covering fraction of the large-scale outflow is low (Hopkins et al., 2016; Wagner et al., 2012, 2013). We note that the ratio of the momentum rate of the molecular outflow to the momentum rate of UFO ($\dot{P}_{\text{mol}}/\dot{P}_{\text{UFO}} \sim 0.5\text{-}3$) is approximately of order unity within the errors. Richings & Faucher-Giguère (2018) find that $\dot{P}_{\text{mol}}/\dot{P}_{\text{UFO}}$ of order unity could still be attributed to an energy-driven outflow where the thermalized mechanical energy is mostly lost through efficient cooling due to in-situ formation of molecular gas within the outflow.

Additionally, we note that a purely IR radiation driven molecular outflow (as opposed to mechanical acceleration; see e.g. King & Pounds 2015) is not preferred, but not strictly ruled out. In such a scenario, the momentum of the molecular outflow is given by $\dot{P}_{\text{mol}} \sim (1 + \eta\tau_{\text{IR}})(L_{\text{IR}}/c)$ where theoretically $\eta \sim 0.5\text{-}0.9$ (Ishibashi et al., 2018; Zhang & Davis, 2017) and τ_{IR} is the optical depth in the infrared. For IRASF05189-2524, $L_{\text{IR}} = 1.38 \times 10^{12} L_{\odot}$ (González-Alfonso et al., 2017) which implies $\tau_{\text{IR}} \sim 3\text{-}5$, and thus requires significant IR trapping.

Finally, we consider IRASF05189-2524 in the context of nine other sources which have observed UFOs and large-scale galactic outflows with good constraints on their spatial scales. Fig. 2.8 shows the momentum rate against the velocity of the outflow while §2.8 includes detailed information and references for each object. It is clear that some objects reside in the momentum-driven regime while others are more consistent with the energy-driven scenario suggesting that there is a range of efficiency factors ($f \sim$

0.001–0.5) that likely depend on specific physical conditions in each object.

2.7 Conclusions

We present new *XMM-Newton* and *NuSTAR* observations of the galaxy merger IRASF05189-2524 a ULIRG and optical Seyfert 2. Testing multiple spectral models yields a best-fit model consisting of a highly ionized absorber with either an absorbed power law and neutral partial covering absorber or a neutral absorber and scattered emission. We find evidence for a blueshifted Fe K absorption feature at $E = 7.8$ keV (rest-frame) which implies an ultra-fast outflow with $v_{\text{out}} = 0.11 \pm 0.01c$.

We calculate that the UFO has a mass outflow rate of $\dot{M}_{\text{out}} \gtrsim 1.0 M_{\odot} \text{ yr}^{-1}$, a kinetic power of $\dot{E}_{\text{K}} \gtrsim 3.6 \times 10^{44} \text{ erg s}^{-1}$ (8% L_{AGN}), and a momentum rate (or force) of $\dot{P}_{\text{out}} \gtrsim 22 \times 10^{34} \text{ dyne}$ ($1.4 L_{\text{AGN}}/c$). Observed large-scale galactic outflows in IRASF05189-2524 have an average momentum rate of $\dot{P} = 68 \times 10^{34} \text{ dyne}$, yielding $\dot{P}_{\text{inner}}/\dot{P}_{\text{outer}} \sim 3$. Given the large uncertainties in the momentum rate estimates, $\dot{P}_{\text{inner}}/\dot{P}_{\text{outer}}$ is not inconsistent with unity, or a momentum-driven scenario. In the energy-driven outflow scenario, the fraction f of the kinetic energy in the inner X-ray wind that goes into bulk motion of the large-scale outflow is $f \sim 0.05$. Such a low efficiency could be attributed to a highly clumpy interstellar medium or if the covering fraction of the large-scale outflow is low or if the hot gas has efficiently cooled leading to an in-situ formation of the molecular outflow.

We compare the outflow in IRASF05189-2524 to nine other objects with observed UFOs and large-scale galactic outflows with solid constraints on the outflow energetics.

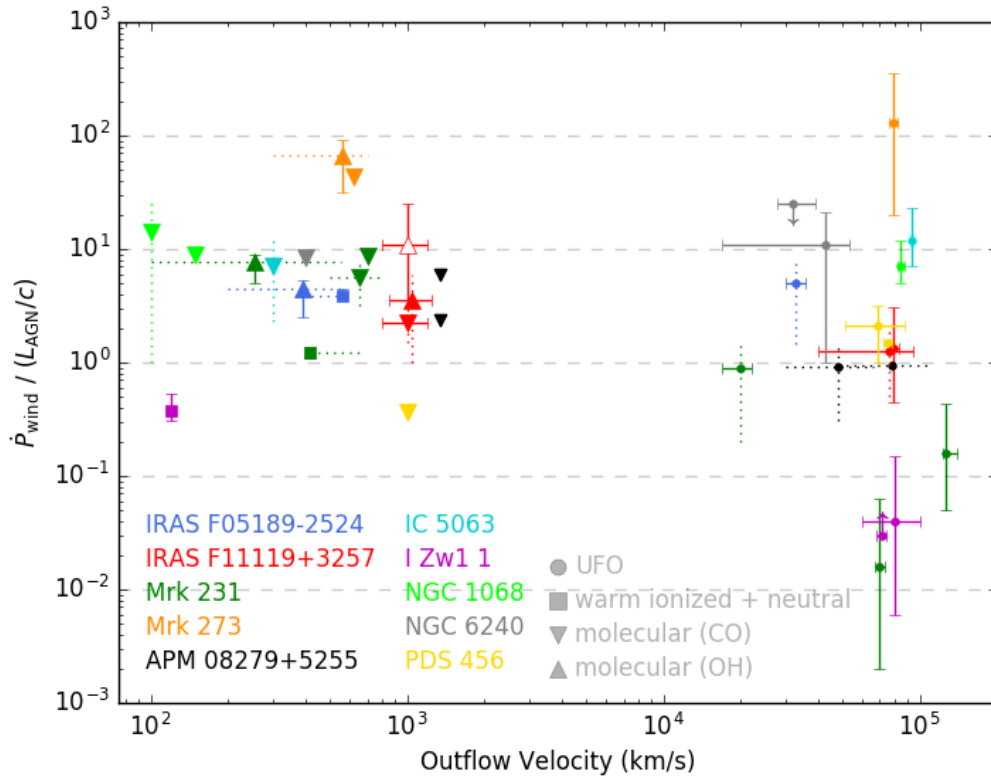


Figure 2.8: The momentum rate (\dot{P}_{wind}) normalized by the momentum of the radiation (L_{AGN}/c) is plotted against the wind outflow velocity for ten objects with observed ultra-fast outflows and large-scale galactic outflows with good constraints on their spatial scales. Solid error bars indicate that upper and lower errors were calculated whereas dotted error bars indicate that only a range of values was provided. Arrows indicate limits. UFO measurements are plotted as circles, warm ionized and neutral gas as squares, the molecular (CO) as downward triangles, and the molecular (OH) as upward triangles. For molecular measurements, filled symbols indicate a time-averaged momentum rate whereas an “instantaneous” or local momentum rate. See Table 2.7 in §2.8 for more details and references for each specific object.

We find that there is a range of efficiency factors ($f \sim 0.001\text{--}0.5$) and driving mechanisms that likely depend on specific physical conditions in each object. While this remains a small sample, it is an important step towards building a comprehensive sample which can be used to further probe the complex relationships of AGN and galaxy co-evolution.

2.8 Appendix: Outflow Energetics of the AGN Sample

Table 2.7: Outflow velocities and momentum rates for ten objects with observed ultra-fast outflows and large-scale galactic outflows with good constraints on their spatial scales. Errors are presented when published by their respective authors. For simplicity, objects with both warm ionized and neutral observed outflows were plotted as a single data point in Fig. 2.8. References: 1) This paper; 2) [Bischetti et al. 2019](#); 3) [Cicone et al. 2014](#); 4) [Feruglio et al. 2015](#); 5) [Feruglio et al. 2017](#); 6) [Fluetsch et al. 2019](#); 7) [García-Burillo et al. 2014](#); 8) [González-Alfonso et al. 2017](#); 9) [Luminari et al. 2018](#); 10) [Mizumoto et al. 2019](#); 11) [Nardini et al. 2015](#); 12) [Rupke et al. 2017](#); 13) [Tombesi et al. 2015](#); 14) [Tombesi et al. 2017](#); 15) [Veilleux et al. 2017](#).

Object	Gas Phase	v_{wind} (km s^{-1})	$\dot{P}_{\text{wind}}^{\text{a}}$ (L_{AGN}/c)	Ref.
IRASF05189-2524	hot ionized	$33,000 \pm 3,000$	1.44–8.48	1
	neutral	560	$3.85^{+0.59}_{-0.26}$	12
	warm ionized	423	0.05 ± 0.01	12
	molecular (CO)	491	4.44	6
	molecular (OH)	200–550	$4.44^{+0.91}_{-1.96}$	8
IRAS F11119+3257	hot ionized	$76,500 \pm 3,300$	$1.30^{+1.70}_{-0.90}$	13
	hot ionized	$76,000^{+18,000}_{-35,000}$	0.5–2	14
	molecular (CO)	1000 ± 200	1.5–3.0	13
	molecular (OH)	1000 ± 200	$11^{+14.1}_{-7.5}$	15
	molecular (OH)	1000 ± 200	1.0–6.0	15
Mrk 231	hot ionized	$20,000^{+2,000}_{-3,000}$	0.2–1.6	4 ^b
	hot ionized	$127,000^{+13,000}_{-4,000}$	$0.16^{+0.27}_{-0.11}$	10
	hot ionized	$70,000 \pm 3,000$	$0.016^{+0.048}_{-0.014}$	10
	neutral	416	$1.23^{+0.15}_{-0.08}$	12

	warm ionized	672	0.008 ± 0.001	12
	molecular (CO)	500–800	3.2–8.0	4 ^b
	molecular (CO)	700	8.7	3 ^b
	molecular (OH)	100–550	$7.74^{+2.68}_{-1.05}$	8
Mrk 273	hot ionized	$79,000 \pm 3,000$	130^{+220}_{-110}	10
	molecular (CO)	620	43	3 ^b
	molecular (OH)	300–700	67^{+25}_{-35}	8
APM 08279+5255	hot ionized	48,000–108,000	0.95	5
	hot ionized	30,000–66,000	0.3–1.5	5
	molecular (CO)	1340	2.37	5
	molecular (CO)	1340	5.97	5
IC 5063	hot ionized	$93,000^{+1,300}_{-1,400}$	12^{+11}_{-5}	10
	molecular (CO)	300	2.3–12.0	3 ^b
I Zw 1	hot ionized	$80,000 \pm 20,000$	$0.04^{+0.11}_{-0.03}$	10
	hot ionized	$71,000 \pm 3,000$	>0.03	10
	neutral	120	$0.37^{+0.15}_{-0.07}$	12
NGC 1068	hot ionized	$84,000^{+3,000}_{-2,000}$	7^{+5}_{-2}	10
	molecular (CO)	100	1–27	7
	molecular (CO)	150	9	3 ^b
NGC 6240	hot ionized	$43,000^{+10,000}_{-26,000}$	11 ± 10	10
	hot ionized	$32,000^{+7,000}_{-4,000}$	<25	10
	molecular (CO)	400	8	3 ^b
PDS 456	hot ionized	$69,000 \pm 18,000$	2.1 ± 1.1	9
	hot ionized	$75,000 \pm 3,000$	1.5	11
	molecular (CO)	1000	0.36	2

^a $\dot{P}_{\text{wind}} = \dot{M}_{\text{wind}} v_{\text{wind}}$; $\dot{E}_{\text{wind}} = \frac{1}{2} \dot{M}_{\text{wind}} v_{\text{wind}}^2$

^b CO-based molecular outflow momentum rates from these references were divided by a factor of 3 so that they are on the same scale as the other measurements.

Chapter 3: Correlated Variability in NGC 1275 at the Center of the Perseus Cluster

3.1 Object Overview

NGC 1275 is the brightest cluster galaxy (BCG) of the Perseus Cluster, the closest ($z = 0.0176$; [Hitomi Collaboration et al. 2016](#)) massive ($M = 6.6 \pm 0.4 \times 10^{14} M_{\odot}$; [Simionescu et al. 2011](#)) cool-core cluster. The Perseus Cluster is the X-ray brightest cluster in the sky and the quintessential source for studying AGN-cluster feedback. NGC 1275 hosts an AGN considered a Seyfert Type 1.5 based on its broad optical emission lines ([Ho et al., 1997](#); [Véron-Cetty & Véron, 2010](#)), but is more often classified as a blazar due to its rapid continuum variability and polarization (see e.g. [Angel & Stockman 1980](#); [Pronik et al. 1999](#)). There are asymmetric radio jets extending from kpc scales down to pc scales, similar to a Fanaroff-Riley type I (FR I) radio galaxy with the jet axis near the line of sight ([Pedlar et al. 1990](#); [Asada et al. 2006](#)). The radio component of NGC 1275 is designated 3C 84. Deep *Chandra* observations of the Perseus Cluster (Fig. 3.1) reveal that the central region of the cluster is dominated by thermal emission from the ICM cooling flow ([Churazov et al., 2003](#); [Fabian et al., 2011](#)) and that the radio lobes are aligned with 15 kpc diameter bubbles in the hot ICM ([Fabian, 2006](#); [Fabian et al., 2000](#)). Further from the

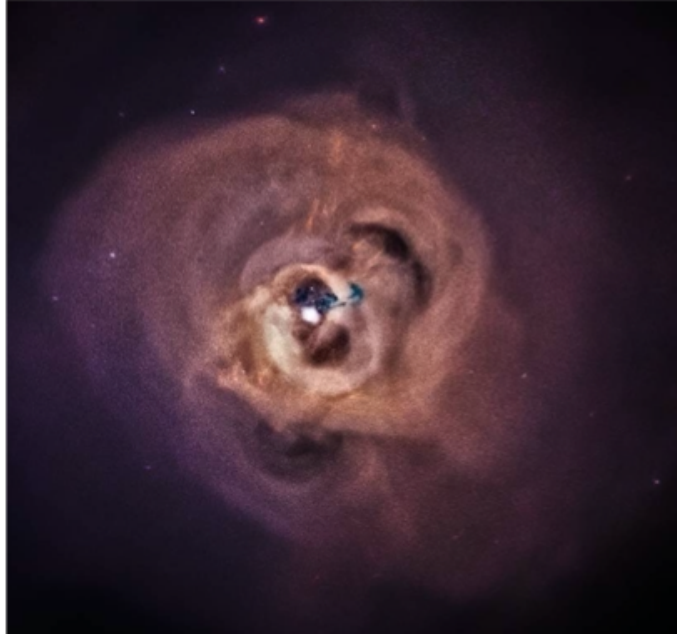


Figure 3.1: *Chandra* ACIS X-ray image of the Perseus Cluster with >1 Ms exposure. Recent bubbles aligned with current jet activity are pronounced in the center of the cluster. Relic bubbles at larger radii are also visible. The interaction of the radio jet with the ICM forming the bubbles is thought to be the mechanical AGN feedback responsible for injecting heat into the cluster ICM. Image credit: NASA/CXC/SAO/E.Bulbul

center of the cluster are “ghost” bubbles that are not aligned with the current jet structure and are thought to be relics of previous jet activity. Similar bubbles are found in the ICM of other large galaxy clusters. [Bîrzan et al. \(2004\)](#) find that the estimated power needed to inflate the bubbles is tightly correlated with the cooling luminosity of cluster. This relationship provides strong evidence for mechanical feedback from the AGN to counteract the cooling of the ICM.

Studies of NGC 1275 at various wavelengths of have increased our understanding of the physical composition of the complex AGN/cluster system. Near-infrared integral field unit data taken with the United Kingdom Infrared Telescope (UKIRT) Imaging Spectrometer (UIST) revealed spatially resolved nuclear ro-vibrational molecular hydrogen (H_2) emission ([Wilman et al., 2005](#)). This H_2 emission is suggested to originate from

part of a clumpy disk rotating about the radio-jet axis. The change in velocity of H_2 across the nucleus implies a black hole mass of $M_{\text{BH}} = 3.4 \times 10^8 M_{\odot}$ (Wilman et al., 2005). High spatial resolution data from the *Gemini North* Near-infrared Integral Field Spectrograph (NIFS) revealed molecular material forming a rotating circumnuclear disk with radius $r \sim 50$ pc (Scharwächter et al., 2013). The dynamics of such a disk imply a total enclosed mass, which can be interpreted as an upper limit on the black hole mass, of $M = 8_{-2}^{+7} \times 10^8 M_{\odot}$. Scharwächter et al. (2013) argue that the H_2 lines are shock excited and estimate the circumnuclear disk contains $\sim 4 \times 10^8 M_{\odot}$ of molecular gas orbiting the SMBH. Additionally, they find evidence for a retrograde streamer of molecular gas.

Nagai et al. (2019) present Atacama Large Millimeter Array (ALMA) data that traces the circumnuclear molecular gas with $\text{CO}(2-1)$, $\text{HCN}(3-2)$, and $\text{HCO}^+(3-2)$ lines with a spatial resolution of 20 pc. They also find a complex set of molecular filaments and a cold rotating molecular disk extending 100 pc from the SMBH. Nagai et al. (2019) highlight the similarity of this filament structure with predictions from the cold chaotic accretion model presented by Gaspari et al. (2017). The ALMA data imply that the rotational axis of the molecular disk is consistent with the axis of the radio jet, suggesting that we are seeing the outer regions of the SMBH accretion flow which preserves its orientation close to the black hole. Nagai et al. (2019) report 300-600 km s^{-1} blueshifted absorption of $\text{HCN}(3-2)$ and $\text{HCO}^+(3-2)$ against the radio continuum of the pc-scale jet emission suggesting a fast molecular outflow from the AGN with an H_2 column density $N_{\text{H}_2} \approx 1.32 \times 10^{22} \text{ cm}^{-2}$. Additional evidence of this fast molecular outflow is found in new *Gemini* NIFS data showing a high velocity dispersion component of the H_2 line which extends across the $3'' \times 3''$ field of view (Riffel et al., 2020).

Recent detailed analysis of the 2017 time-averaged *Chandra* High Energy Transmission Grating (HETG) spectrum (data described in §3.2.1) find evidence that 15%-20% of the X-ray emission is absorbed a cold atomic and/or molecular column density of $N_{\text{H}} \approx 8 \times 10^{22} \text{ cm}^{-2}$ suggesting that some of the X-ray emission is absorbed by molecular gas found in NIR observations (Reynolds et al., 2021). The *Chandra* data definitely rule out the possibility of the entire X-ray source being absorbed by molecular gas with a column density of $N_{\text{H}} \approx 2 \times 10^{22} \text{ cm}^{-2}$ as seen by ALMA towards the pc-scale jet (Nagai et al., 2019). Additionally, the time-averaged spectrum shows no evidence of photoionized absorption indicative of outflows seen in approximately half of all Seyfert AGN (Reynolds 1997; Tombesi et al. 2013; Laha et al. 2021).

Between 1970 and 2000, the X-ray and 90 GHz radio flux of NGC 1275 decreased by roughly an order of magnitude (Fig. 3.2; Fabian et al. 2015). Radio VLBA monitoring revealed that the flux began to increase gradually around 2005 followed by a rapid increase around 2008 (Suzuki et al., 2012). NGC 1275 was definitely detected at GeV γ -ray energies at the beginning of the *Fermi* mission (Abdo et al., 2009). Subsequent monitoring shows both gradual and rapid variations/flares on timescales as short as a week (Kataoka et al. 2010; Brown & Adams 2011; Hodgson et al. 2018). The detection with *Fermi* is of note given that NGC 1275 was tentatively detected by the COS-B satellite between 1975-1982 (Strong & Bignami, 1983), but not by CGRO-EGRET between 1991-2000 (Reimer et al., 2003) even though the flux measured by *Fermi* by 2008 was seven times greater than EGRET's upper limit. Thus we can infer that the γ -ray emission from NGC 1275 is also highly variable on decade timescales. NGC 1275 was first detected at TeV energies by the Major Atmospheric Gamma Imaging Cherenkov (MAGIC) Telescope (Aleksić et al.,

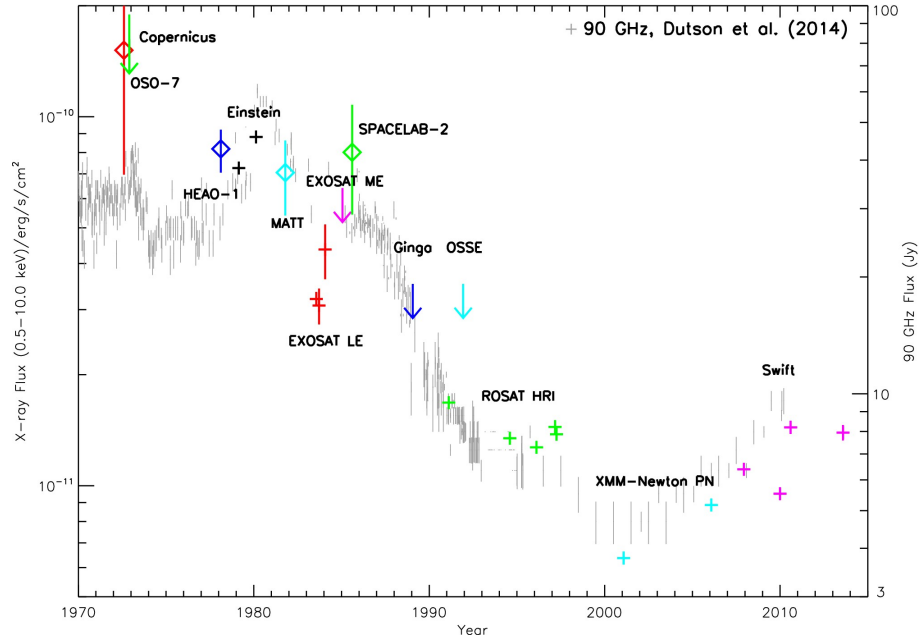


Figure 3.2: Historical light curve of NGC 1275 from 1970-2015. Gray points are 90 GHz radio measurements (Dutson et al., 2014). Various X-ray and γ -ray instruments are plotted and labeled as individual points. The radio and high energy emission have varied together over decade timescales, including a dramatic order of magnitude decrease in flux between 1980-2000. Figure reproduced from Fabian et al. 2015.

2012, 2014). In 2016-2017, several bright and rapid TeV flares were detected by the Very Energetic Radiation Imaging Telescope Array System (VERITAS; Mirzoyan 2016, 2017; Mukherjee & VERITAS Collaboration 2016, 2017). Much work has been dedicated to understanding connections between radio, X-ray, and γ -ray emission from NGC 1275 in order to better understand the physical mechanisms of the AGN.

3.1.1 Radio Jet Structure

There exists a large body of literature dedicated to understanding the complex structure of the radio jet in NGC 1275, which has changed appreciably on human timescales. Early Very Long Baseline Interferometry (VLBI) revealed complex structure on milliarcsec (mas) scales (Pauliny-Toth et al., 1976). The source at that time was dominated by an

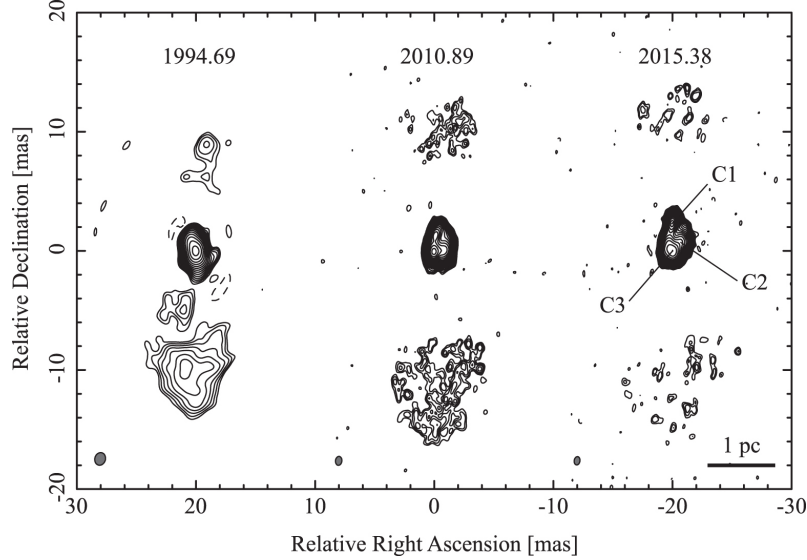


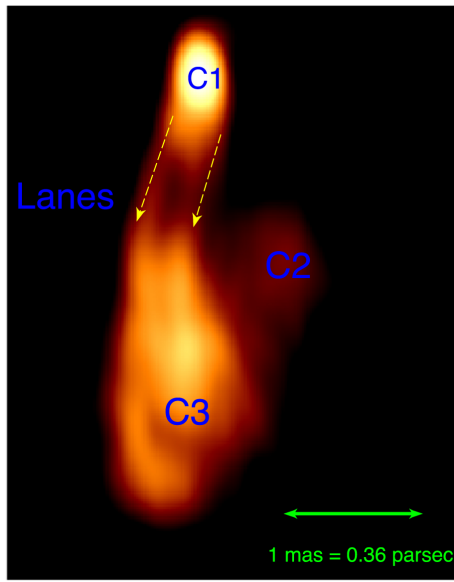
Figure 3.3: 15 GHz VLBA data of the core and lobe structure of the radio jet in NGC 1275. The asymmetric lobes have been fading for at least two decades. Figure reproduced from [Kino et al. 2017](#).

inverted core with a second component located 1 mas (0.4 pc) away with a position angle (PA) of 210° ([Unwin et al. 1982](#); [Readhead et al. 1983a,b](#)). On scales of 10-15 mas (4-6 pc), VLBI traced out fainter knots tracing out a likely jet channel south (PA of 170 - 180°) from the inverted core which apparently connects to the kpc-scale jet with a PA of 170° ([Pedlar et al., 1983](#)). Continued VLBI monitoring showed complex motions and flux variations of these jet components ([Wright et al. 1988](#); [Marr et al. 1989](#); [Krichbaum et al. 1992](#)). The northern counter-jet was detected with VLBI at 22 GHz by [Vermeulen et al. \(1994\)](#). The inverted spectrum of the counter-jet suggested the influence of free-free absorption by an ionized screen with temperature $T \sim 10^4$ K and column density $N_{\text{H}} \sim 10^{23} \text{ cm}^{-2}$ ([Vermeulen et al. 1994](#); [Walker et al. 2000, 1994](#)). Given that the free-free screen absorbs the counter-jet but not the jet suggests that it is part of the outer region of the accretion disk.

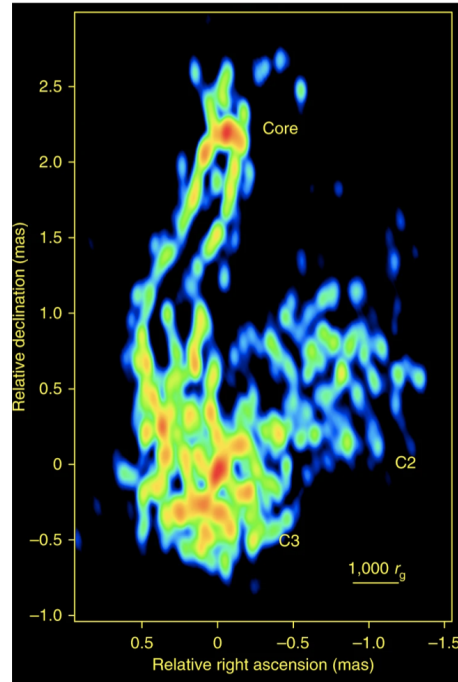
As seen in Fig. 3.2, high-frequency 90 GHz radio monitoring showed that the

AGN faded appreciably from early VLBI studies to a minimum around the year 2000 (Dutson et al., 2014; Fabian et al., 2015). Monitoring at 15 GHz shows the pc-scale radio lobes fading over two decades (Fig. 3.3a; Kino et al. 2017). Since then, unusual amounts of activity have been reported in the core of the jet. A new jet component (C3) was discovered in 22 GHz VLBI data to be moving away from the core (C1) with a PA of 180° (Nagai et al., 2010). Initially believed to have launched in 2005, subsequent analysis of higher resolution 43 GHz data revealed that C3 was already distinct from C1 as early as 2003 November (Suzuki et al., 2012). A 43 GHz image of the core with main components labeled is shown in Fig. 3.4 (reproduced from Hodgson et al. 2021). A third core component, C2, is a faint, relatively stationary emission region with a PA of $\sim 40^\circ$ which is thought to correspond to previous jet activity (Nagai et al., 2010).

The emerging picture is that C3 is the working surface of a new radio lobe associated with renewed jet activity (Nagai et al. 2016; Kino et al. 2017). As of 2016, C3 was approximately 3 mas (1 pc projected distance) due south of the core C1. Monitoring by the Korean VLBI Network (KVN) supports this picture thus far. KVN data show weaker features in the jet that propagate from the core with apparent speeds of $0.2-0.9c$ until they near C3 at which point they deflect and/or break apart. The interaction of these smaller features with C3 are associated with radio flares that are often coincident with a major γ -ray flare (Hodgson et al., 2018, 2021). In 2015 August, Kino et al. (2018) report that the location of C3 moves eastwards by 0.4 mas before continuing to propagate to the south, suggesting that the jet's working surface is pushing into a clumpy and dense medium; the density required to provide the necessary ram pressure corresponds to $n \sim 4 \times 10^3 - 2 \times 10^5 \text{ cm}^{-3}$, suggesting of a clumpy molecular medium. Nagai et al.



(a)



(b)

Figure 3.4: The radio emission from NGC 1275 is dominated by a bright, compact core, labeled C1 in these diagrams. Component C3 is believed to have been launched from C1 in late 2003 corresponding to the increase in radio emission which broadly continues today. (a) Stacked 43 GHz image reproduced from [Hodgson et al. 2021](#). (b) RadioAstron imaging revealing the collimation of the jet to within a few hundred r_g of the black hole. Reproduced from [Giovannini et al. 2018](#).

(2014) reported a cylindrical jet profile on scales $\gtrsim 10^3 r_g$. VLBI imaging from the orbiting radio telescope RadioAstron ([Kardashev et al., 2013](#)) permitted detailed study of the collimation profile of the jet from $\sim 10^2 - 10^4 r_g$ from the black hole ([Giovannini et al., 2018](#)), thus providing evidence for strong collimation of the jet to within a few hundred r_g of the core (see Fig. 3.4b, reproduced from [Giovannini et al. 2018](#)).

Multiwavelength observations of NGC 1275 strive to understand the many emission mechanisms present in this complex source, often by studying correlated variability as it gives insight into which emission mechanisms work in tandem. Much of this literature will be discussed in subsequent sections alongside new variability results presented in this

chapter.

3.2 Observations and Data Analysis

3.2.1 New *Chandra* Observations

We present *Chandra* High Energy Transmission Grating (HETG) observations of NGC 1275 taken as part of a Cycle-19 Large Project. Observations were taken in 15 segments (ObsIDs) between 2017 October 24 and 2017 December 5 for a total good exposure time of ~ 490 ks. Dates and observation exposures are given in Table 3.1. The large number of observations in a relatively short period of time provides an unprecedented cadence for studying short-term X-ray variability in this object.

To reduce the risk of mild pileup, we turned off the two outer ACIS-S chips (S0 and S5) and used 1/2 subarrays on the remaining four chips resulting in a reduced frame readout time of 2.4 seconds. Turning off the outer chips does negatively impact observing the softest regions of the spectrum, but the contaminant build up on the ACIS optical blocking filters unavoidably removes those soft photons anyway.

Utilizing the HETG dispersed spectrum on ACIS-S provides a unique opportunity to produce a high-quality, high-resolution spectrum of the AGN isolated from the surrounding cluster, which until now, has affected previous low-pileup spectral observations (e.g. Churazov et al. 2003; Berg et al. 2017; Hitomi Collaboration et al. 2018). Examining the image of ObsID 20841 in Fig. 3.5, we see it is dominated by the zeroth order image of the Perseus Cluster and even the famous bubbles are visible. There are two two-sided dispersed spectra of the bright central AGN emission, one from the High Energy Grating

Table 3.1: Information for 15 new *Chandra* observations of NGC 1275 including 2-10 keV flux and photon index Γ from a model consisting of a single power-law modified by Galactic absorption. Errors are given at $1-\sigma$. Of note is the high temporal cadence of the observations as well as the similar roll angle of the spacecraft during all observations.

ObsID	Start Date (yyyy-mm-dd)	MJD	Exposure (ks)	Roll Angle (deg)	HEG Count Rate (cnt/s)	2-10 keV Flux ($\times 10^{-11}$ erg cm $^{-2}$ s $^{-1}$)	Γ
20823	2017-10-24	58050.5	53.18	142	0.086 \pm 0.002	2.31 \pm 0.04	1.93 \pm 0.03
20450	2017-10-27	58053.1	29.58	142	0.082 \pm 0.004	2.07 \pm 0.06	1.87 \pm 0.04
20826	2017-10-28	58055.0	29.58	142	0.093 \pm 0.004	2.30 \pm 0.05	2.00 \pm 0.04
20451	2017-10-30	58056.0	36.47	151	0.091 \pm 0.003	2.41 \pm 0.05	1.89 \pm 0.03
20837	2017-10-31	58057.6	34.50	151	0.094 \pm 0.003	2.45 \pm 0.06	1.92 \pm 0.03
20838	2017-11-01	58058.4	24.67	151	0.089 \pm 0.004	2.22 \pm 0.06	1.93 \pm 0.04
20839	2017-11-03	58060.6	21.72	151	0.096 \pm 0.005	2.33 \pm 0.07	1.94 \pm 0.04
20840	2017-11-04	58061.5	20.74	151	0.094 \pm 0.005	2.26 \pm 0.08	1.98 \pm 0.04
20449	2017-11-06	58063.7	45.31	165	0.088 \pm 0.003	2.37 \pm 0.05	1.88 \pm 0.03
20841	2017-11-09	58066.3	54.16	165	0.088 \pm 0.002	2.45 \pm 0.04	1.86 \pm 0.03
20842	2017-11-10	58067.3	18.33	165	0.089 \pm 0.005	2.08 \pm 0.08	1.89 \pm 0.05
20843	2017-11-11	58068.2	22.11	165	0.086 \pm 0.005	2.13 \pm 0.07	1.88 \pm 0.04
20824	2017-12-02	58089.3	49.25	220	0.092 \pm 0.003	2.52 \pm 0.05	1.90 \pm 0.03
20827	2017-12-04	58091.1	16.95	220	0.087 \pm 0.006	2.01 \pm 0.07	1.91 \pm 0.05
20844	2017-12-05	58092.1	34.50	220	0.091 \pm 0.003	2.37 \pm 0.06	1.92 \pm 0.03

(HEG) and one from the Medium Energy Grating (MEG), which are clearly visible. The HETG is a slitless grating array and therefore also disperses the extended ICM of the cluster, however, it is clear that the dispersed emission of the AGN is distinct and can be well isolated from the ICM emission. Additionally, order sorting of the spectra, where only photons with CCD-detected energies compatible with their spatial position along the dispersion spectrum are accepted, further isolates the AGN spectrum from the ICM.

Utilizing the HETG dispersed spectrum on ACIS-S provides a unique opportunity to produce a high-quality, high-resolution spectrum of the AGN isolated from the surrounding cluster, which until now, has affected previous low-pileup spectral observations (e.g. [Churazov et al. 2003](#); [Berg et al. 2017](#); [Hitomi Collaboration et al. 2018](#)). Examining the image of ObsID 20841 in Fig. 3.5, we see it is dominated by the zeroth order image of the Perseus Cluster and even the famous bubbles are visible. There are two two-sided dispersed spectra of the bright central AGN emission, one from the High Energy Grating (HEG) and one from the Medium Energy Grating (MEG), which are clearly visible. The HETG is a slitless grating array and therefore also disperses the extended ICM of the cluster, however, it is clear that the dispersed emission of the AGN is distinct and can be well isolated from the ICM emission. Additionally, order sorting of the spectra, where only photons with CCD-detected energies compatible with their spatial position along the dispersion spectrum are accepted, further isolates the AGN spectrum from the ICM.

All data were reprocessed with CIAO-4.12 ([Fruscione et al., 2006](#)) and CALDB v4.9.1. Data reduction followed standard procedures¹ with three exceptions. First, we reduce the width of the spectral extraction regions by half using `width_factor_hetg`

¹https://cxc.cfa.harvard.edu/ciao/threads/spectra_hetgacis/

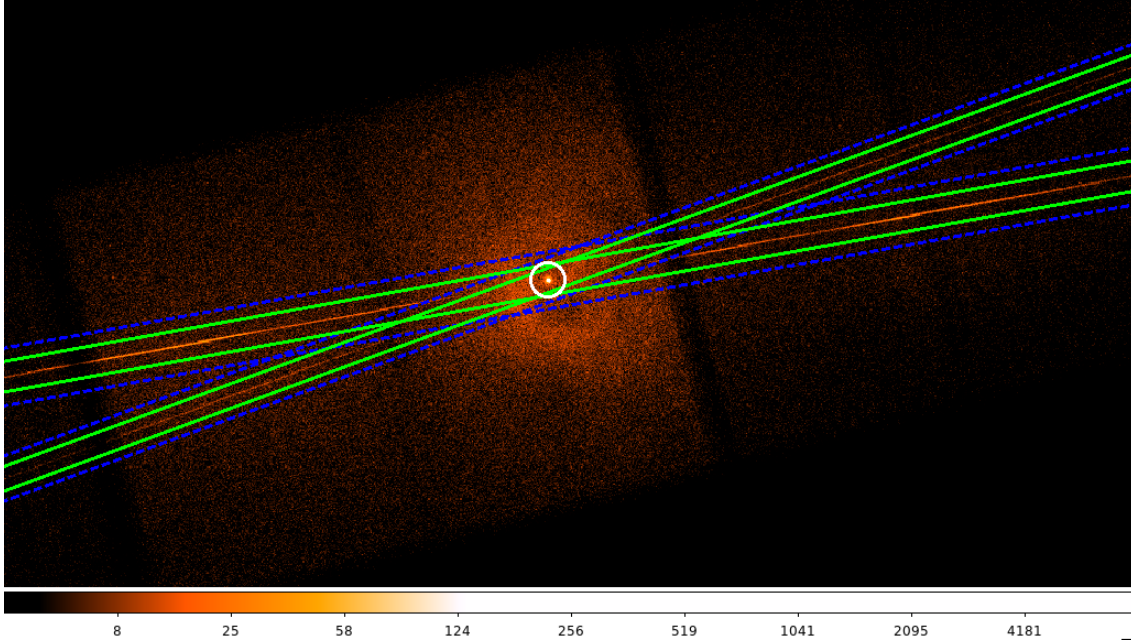


Figure 3.5: Image of ObsID 28041 overlaid with both the default wider spectral extraction region (blue) and the narrower extraction region (green) used in our analysis. Both regions use the same default circular source region (white). Narrowing the spectral extraction region reduces the overlap of the regions toward the source. Even in a single observation, the bubbles of the Perseus Cluster are visible in the zeroth order image.

= 18. This reduces the overlap of the MEG and HEG spectral regions toward the center of the dispersion pattern which reduces noise at higher energies in the HEG thus allowing spectral fitting up to 9 keV. The difference in width of the spectral regions is shown in Fig. 3.5.

Second, the standard algorithm for automatically locating the zeroth order image failed for most ObsIDs, likely due to confusion from the high-surface brightness of the extended ICM emission. An incorrect location would cause a misidentification of the center of the dispersed spectrum leading to an incorrect wavelength scale used for translating the location of the dispersed spectrum to an energy. The automatic location was corrected by manually setting the zeroth order location in `tgdetect` to the coordinates of the nucleus of NGC 1275 as determined by the spacecraft astrometry. Then, a sub-pixel

image (see §4.2.1) was visually inspected to ensure that the zeroth order image is correctly centered on the AGN point source within 0.2'' or less. Extracting the spectra produce a +1 and -1 order spectra for each the HEG and MEG. The +/-1 order spectra are summed for each ObsID. Each ObsID was combined using the CIAO `combine_grating_spectra` command to produce a single time-averaged HEG and MEG spectrum for NGC 1275. Second and third order spectra were extracted and examined but did not contain sufficient signal to noise to be useful and will not be discussed further.

An initial fit of the time-averaged spectra with a single power law with Galactic absorption ($N_{\text{H}} = 1.32 \times 10^{21} \text{ cm}^{-2}$; Kalberla et al. 2005) revealed 10%-15% excess energy in three regions: 1) below 1.3 keV in the MEG, 2) between 2.2-2.5 keV in both the MEG and HEG, and 3) from 6-7 keV in the HEG. The structure from 6-7 keV corresponds to the known iron $K\alpha$ fluorescent line from cold gas near the AGN (Hitomi Collaboration et al., 2018; Reynolds et al., 2021). The lower energy residuals closely mirror structure seen in the background spectra (see Fig 3.6a) suggesting that the standard grating extraction algorithms underestimated the background normalization. The true background for the AGN spectrum is mainly comprised of dispersed (and some zeroth order) ICM emission which is centrally peaked around the AGN. The actual extracted background spectrum, however, must be extracted from rectangular regions parallel and adjacent to the spectral extraction regions. Due to the offset position of these background regions, they necessarily under-predict the dispersed ICM emission (since the underlying emission is centrally-peaked), thus leading to background regions with incorrect normalization. The correct normalization cannot be easily calculated given that it is a non-trivial function of the ICM spatial and spectral structure.

Instead, we pursue an empirical approach to estimating the appropriate normalization of the background by stepping through a range of background renormalization values for both the HEG and MEG. For each combination of values, we calculate the C-statistic of the power law fit (see Fig. 3.6b). We find that the C-statistic is minimized if the HEG and MEG backgrounds are both scaled up by a factor of 1.96 which corresponds to setting AREASCAL = 0.51 in the events file header. This renormalization of the background reduces the residuals from the power law fit to 3%-5%. We validated this process using MARX (Davis et al., 2012) to simulate an HETG observation of a Perseus-like cluster with the following components: 1) a point-like AGN with a power law spectrum with a photon index $\Gamma=1.9$, 2) an ICM core described by a β -profile with a core radius of 2' and an optically thin thermal plasma spectrum with temperature $kT = 4$.keV, and 3) a model of the ICM bubble structure made up of two annular rings offset to just overlap at the AGN with an inner radius of 0.6', an outer radius of 1', and an optically thin thermal plasma spectrum with temperature $kT = 2$ keV. The β -profile is the isothermal surface brightness profile of the cluster defined by Cavaliere & Fusco-Femiano (1976) as $S = S_0[1 + (r/a)^2]^{-3\beta+1/2}$ where S_0 , a , and β are free parameters. In this model, a is the radius of the X-ray core and a typical value of β is $\sim 2/3$ (see Arnaud 2009 and references therein). The simulated spectra were extracted from the simulated events file using the same process as the real data. Analysis of the simulated spectra confirm that the cluster emission leads to a systematic underestimate of the normalization of the background by a factor of ~ 2 .

Power law fits to the individual ObsIDs revealed excess residuals in the same energy bands as the time-averaged spectrum; however, there was insufficient signal to noise in

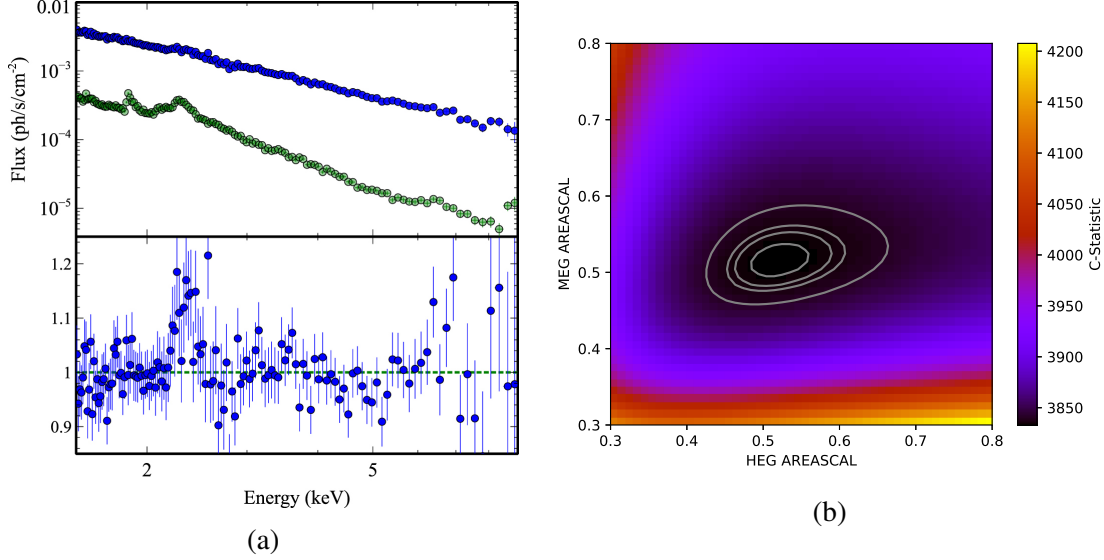


Figure 3.6: Left: Time-averaged HEG spectrum (blue) of NGC 1275 fit with a single power law and using the default background normalization (green). The significant residuals in the bottom panel at ~ 2.5 keV mirror a feature in the background spectrum. Figure reproduced from Reynolds et al. 2020. Right: C-statistic values for different background normalizations of the HEG and MEG. Contours are shown at 1-, 90%, 2- σ , and 3- σ . The model residuals are minimized with AREASCAL values of 0.51 for both the HEG and MEG.

individual observations to empirically assess the background normalization. We therefore apply the same background renormalization derived from the time-averaged spectrum to each individual observation. Given the asymmetric nature of the cluster ICM, the amount of ICM dispersed along with the AGN depends only on the roll angle of the spacecraft. Both in Table 3.1 and Fig. 3.6, we see that the roll angle of all 15 observations are quite similar, therefore the background renormalization of the observations are sufficiently similar to not impact broad-band measurements of flux.

Once the background renormalization was applied to each observation, the HEG and MEG were jointly fit with a model consisting of a single power law with Galactic absorption ($N_{\text{H}} = 1.32 \times 10^{21} \text{ cm}^{-2}$). The MEG was fit between 1.5-6 keV (observed frame), and the HEG was fit from 2-7.5 keV (observed frame). The best fit was determined

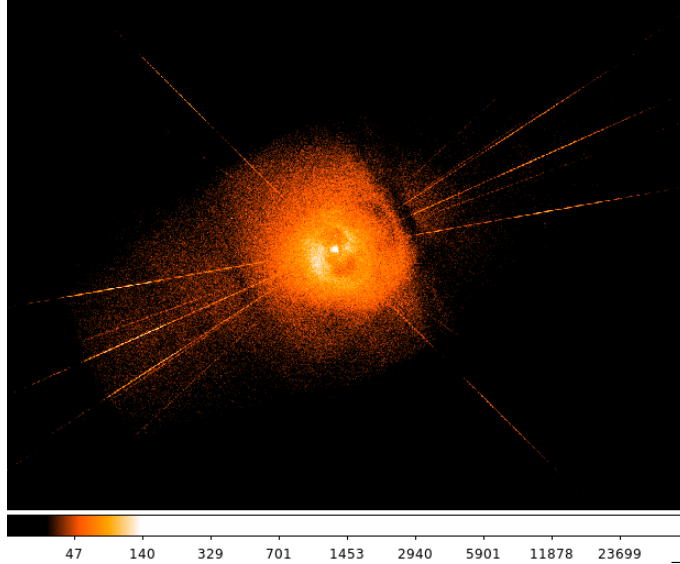


Figure 3.7: Merged *Chandra* image of NGC 1275. The famous structure of the Perseus Cluster is clearly visible in the zeroth order image. We can see that the roll angles of the observations are similar given that most of the dispersed spectra are grouped running from bottom left to upper right. That and the fact that the zeroth order image is not noticeably distorted support using the time-averaged background renormalization on individual observations.

by minimizing the C-statistic appropriate for Poisson distributed data. Flux and photon index measurements are given in Table 3.1. All errors are quoted at $1-\sigma$.

3.2.2 *Swift* XRT Archival Observations

We analyzed archival *Swift* XRT (Burrows et al., 2005; Gehrels et al., 2004) data of NGC 1275 to add a longer-term view of the X-ray properties to complement the short timescale *Chandra* study. When searching the archive, we require that the entire cluster core falls within the XRT. Further limiting the archival data to those taken in the two-dimensional photon-counting (PC) mode yielded 67 observations taken from July 2007 to February 2017. ObsID 00032691001 and 00049799002 were excluded due to low exposure time. Windowed-timing (WT) mode data were excluded as its one-dimensional

imaging make separating the nuclear point source from the surrounding cluster unreliable.

We use a circular source extraction region centered on NGC 1275 with a radius of 22". For each observation above the suggested threshold where pileup may occur ($\sim 0.5 \text{ ct s}^{-1}$)², we inspected the spectrum and found no instances of spectral hardening indicative of pileup. We use an annular background extraction region with an inner radius of 35" and outer radius of 60" which includes the surrounding Perseus Cluster.

Spectra were fit from 0.5-6.0 keV (observed frame) with a single power law with Galactic absorption. Results from the spectral analysis including 2-10 keV flux and photon index Γ are presented in Table 3.2.

3.2.3 *Fermi* LAT Observations

The Large Area Telescope (LAT) is the primary instrument on the *Fermi Gamma-ray Telescope* covering approximately 20% of the sky from 20 MeV to 300 GeV (Atwood et al., 2009). NGC 1275 has been a monitored source since the beginning of the *Fermi* mission. We use fully reduced data from the monitoring light curve from August 2008 to December 2018 provided by Dr. Bindu Rani (GSFC); a full description of *Fermi* LAT data reduction may be found in Hodgson et al. (2018). Source event class photons were analyzed using the standard SCIENCETOOLS (v10.r0.p5) and instrument response functions P8R2_SOURCE_V6. A circular region of interest with a radius of 20° was centered at the position of NGC 1275 and analyzed using a maximum-likelihood algorithm (Mattox et al., 1996). A constant uncertainty (15%) light curve above 100 MeV was generated using the adaptive binning method following Lott et al. (2012).

²The *Swift* Technical Handbook version 17.0

Table 3.2: Archival *Swift* XRT PC-mode observation information. Errors are given at $1-\sigma$.

ObsID	Start Date		Exposure (ks)	2-10 keV Flux	
	(yyyy-mm-dd)	(MJD)		($\times 10^{-11}$ erg cm $^{-2}$ s $^{-1}$)	Γ
00036524001	2007-07-13	54294.7	5.85	1.27 \pm 0.09	1.67 \pm 0.06
00036524002	2007-12-06	54440.7	3.56	1.86 \pm 0.15	1.90 \pm 0.06
00030354003	2009-12-30	55195.1	4.33	1.72 \pm 0.11	1.62 \pm 0.06
00031770001	2010-07-22	55399.9	2.20	2.39 \pm 0.16	1.84 \pm 0.06
00031770002	2010-07-24	55401.9	2.05	2.99 \pm 0.19	1.67 \pm 0.06
00031770003	2010-07-26	55403.6	2.05	1.94 \pm 0.16	1.84 \pm 0.06
00031770004	2010-07-28	55405.9	2.18	2.21 \pm 0.17	1.70 \pm 0.06
00031770005	2010-07-30	55407.7	2.13	1.78 \pm 0.16	1.85 \pm 0.07
00031770006	2010-08-01	55409.2	2.12	1.48 \pm 0.14	1.86 \pm 0.08
00031770007	2010-08-03	55411.1	2.41	1.90 \pm 0.16	1.76 \pm 0.06
00031770008	2010-08-05	55413.6	2.00	1.81 \pm 0.17	1.85 \pm 0.08
00031770009	2010-08-07	55415.1	2.11	2.23 \pm 0.16	1.81 \pm 0.06
00031770010	2010-08-09	55417.7	2.12	2.00 \pm 0.14	1.78 \pm 0.07
00091128001	2011-07-05	55747.1	1.02	1.60 \pm 0.23	1.75 \pm 0.11
00091128002	2011-07-06	55748.0	1.35	1.36 \pm 0.25	1.62 \pm 0.17
00091128003	2011-07-07	55749.2	1.77	1.83 \pm 0.18	1.56 \pm 0.08
00091128004	2011-07-09	55751.2	3.48	1.67 \pm 0.13	1.64 \pm 0.06
00091128005	2011-07-10	55752.1	4.92	1.51 \pm 0.10	1.71 \pm 0.05
00049799001	2013-04-04	56386.5	0.79	2.12 \pm 0.29	1.53 \pm 0.12
00049799003	2013-07-12	56486.0	0.95	2.18 \pm 0.30	1.61 \pm 0.12
00049799004	2013-07-14	56487.4	5.28	2.05 \pm 0.11	1.66 \pm 0.04
00049799005	2013-07-26	56500.0	3.08	2.29 \pm 0.16	1.81 \pm 0.05
00049799006	2013-08-01	56505.1	1.57	2.34 \pm 0.19	1.65 \pm 0.07
00092034001	2015-02-11	57064.4	2.00	2.67 \pm 0.18	1.74 \pm 0.06
00092034002	2015-03-15	57096.0	2.15	2.78 \pm 0.20	1.52 \pm 0.06
00092034003	2015-07-25	57228.1	2.01	2.84 \pm 0.21	1.68 \pm 0.06
00092034004	2015-08-18	57252.0	2.01	2.11 \pm 0.26	1.39 \pm 0.10
00092034005	2015-09-16	57281.6	1.38	1.40 \pm 0.24	1.49 \pm 0.15

ObsID	Start Date		Exposure (ks)	2-10 keV Flux	
	(yyyy-mm-dd)	(MJD)		($\times 10^{-11}$ erg cm $^{-2}$ s $^{-1}$)	Γ
00081530001	2015-11-03	57329.2	6.43	2.10 \pm 0.09	1.74 \pm 0.04
00034380001	2016-02-19	57437.9	2.47	2.47 \pm 0.19	1.58 \pm 0.06
00034380002	2016-02-21	57439.7	2.48	2.19 \pm 0.20	1.55 \pm 0.07
00034380004	2016-02-23	57441.4	2.42	2.61 \pm 0.19	1.48 \pm 0.06
00034380005	2016-02-25	57443.7	2.76	1.92 \pm 0.18	1.53 \pm 0.08
00034380006	2016-02-26	57444.7	2.78	2.74 \pm 0.17	1.52 \pm 0.06
00034380007	2016-02-29	57447.9	1.70	2.46 \pm 0.21	1.59 \pm 0.07
00034380008	2016-03-02	57449.4	2.38	2.49 \pm 0.19	1.43 \pm 0.07
00034380010	2016-03-03	57450.8	2.03	2.63 \pm 0.21	1.43 \pm 0.07
00034380009	2016-03-04	57451.0	2.49	2.21 \pm 0.15	1.58 \pm 0.07
00034404001	2016-03-05	57452.1	3.98	2.07 \pm 0.15	1.58 \pm 0.06
00034380012	2016-03-06	57453.8	2.36	2.53 \pm 0.17	1.57 \pm 0.06
00034380013	2016-03-08	57455.4	2.91	2.33 \pm 0.16	1.58 \pm 0.06
00034380014	2016-03-10	57457.2	2.24	2.84 \pm 0.20	1.51 \pm 0.06
00034404002	2016-03-10	57457.6	0.72	2.37 \pm 0.34	1.57 \pm 0.12
00034380015	2016-03-12	57459.0	2.29	2.61 \pm 0.22	1.56 \pm 0.06
00034404003	2016-03-16	57463.5	2.19	2.33 \pm 0.20	1.51 \pm 0.07
00034765001	2016-10-30	57691.0	1.97	2.81 \pm 0.23	1.62 \pm 0.06
00034765002	2016-10-31	57692.1	1.98	3.04 \pm 0.19	1.64 \pm 0.05
00034765003	2016-11-01	57693.1	1.88	2.96 \pm 0.21	1.70 \pm 0.06
00034765004	2016-11-02	57694.1	1.64	2.66 \pm 0.22	1.62 \pm 0.07
00034765005	2016-11-03	57695.1	1.61	2.08 \pm 0.32	1.42 \pm 0.14
00034765006	2016-11-04	57696.1	1.70	3.21 \pm 0.24	1.68 \pm 0.06
00034765007	2016-11-05	57697.1	1.81	3.19 \pm 0.22	1.62 \pm 0.06
00034765008	2016-11-06	57698.1	2.01	2.83 \pm 0.20	1.65 \pm 0.06
00034765009	2016-11-07	57699.1	1.96	3.93 \pm 0.26	1.62 \pm 0.05
00034765010	2016-11-08	57700.1	1.61	3.01 \pm 0.22	1.72 \pm 0.06
00034765011	2016-11-09	57701.1	1.54	2.54 \pm 0.20	1.82 \pm 0.07
00034765012	2016-11-10	57702.1	1.94	3.24 \pm 0.21	1.64 \pm 0.05
00087312001	2016-12-31	57753.0	0.96	4.47 \pm 0.37	1.50 \pm 0.07

ObsID	Start Date		Exposure (ks)	2-10 keV Flux	
	(yyyy-mm-dd)	(MJD)		($\times 10^{-11}$ erg cm $^{-2}$ s $^{-1}$)	Γ
00087311001	2017-01-01	57754.3	0.63	5.12 \pm 0.45	1.51 \pm 0.08
00087311002	2017-01-02	57755.2	0.80	4.78 \pm 0.40	1.50 \pm 0.07
00087311003	2017-03-15	57828.0	1.08	3.00 \pm 0.26	1.66 \pm 0.07
00087312002	2017-03-21	57833.2	1.47	2.99 \pm 0.25	1.54 \pm 0.07
00087311004	2017-03-21	57833.8	0.87	2.80 \pm 0.32	1.56 \pm 0.09
00087311005	2017-03-24	57836.5	2.42	2.32 \pm 0.20	1.61 \pm 0.07
00087312003	2017-03-25	57837.2	0.81	2.13 \pm 0.28	1.67 \pm 0.11
00087312004	2017-03-26	57838.0	4.80	2.31 \pm 0.12	1.64 \pm 0.04
00087312005	2017-03-31	57843.2	2.14	2.43 \pm 0.18	1.65 \pm 0.06

3.2.4 ASAS-SN Observations

ASAS-SN is an optical all sky survey automatically surveying the entire sky to $\sim 18^{\text{th}}$ magnitude every night using a global network of 24 telescope stations (Kochanek et al., 2017; Shappee et al., 2014). Each station is comprised of four 14-cm telescopes each with a camera with $\sim 8''$ pixels. The Sky Patrol online interface³ provides real-time aperture photometry light curves from ASAS-SN images for any position in the sky. NGC 1275 was observed in the V band with the bb camera 121 times between late 2014-early 2019. The bb camera is part of the station located at the Haleakala Observatory, Hawai‘i hosted by Las Cumbres Observatory. The V band photometry is calculated with a $16''$ radius aperture and is calibrated against the APASS catalog (Henden & Munari, 2014). Due to the large pixel scale, the optical photometry of the AGN is contaminated by the host galaxy, and we make no attempt to remove it. For our purposes, we are only

³<https://asas-sn.osu.edu/>

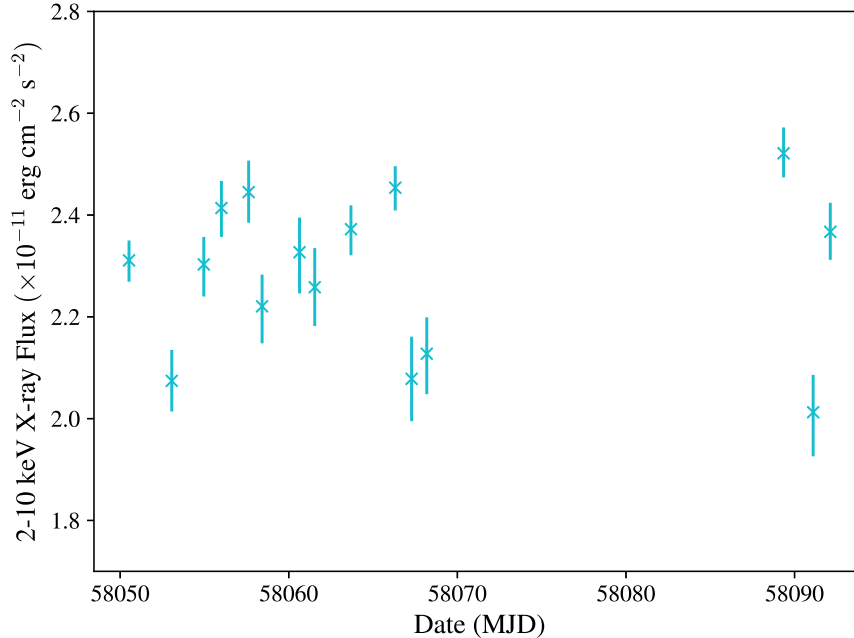


Figure 3.8: X-ray light curve of NGC 1275 from our 6-week long HETG *Chandra* observing campaign. This is the first high-cadence high-resolution light curve of NGC 1275 with minimal ICM contamination from the Perseus Cluster.

concerned with relative variability which can be entirely attributed to the AGN since the host galaxy is not expected to vary, especially on year timescales. We therefore use the ASAS-SN photometry measurements as provided.

3.3 X-ray Variability: The Disk-Jet Interplay

We present in Fig. 3.8 the 2-10 keV light curve of NGC 1275 from a yearlong *Chandra* HETG observing campaign. This is the first robust light curve of the central AGN with minimal contamination from the surrounding ICM of the Perseus Cluster. We find $\sim 10\%$ variation about the mean on short (intraweek) timescales. We can compare this to the light crossing time of the black hole event horizon. Using a derived stellar velocity dispersion, Riffel et al. (2020) estimate the mass of the SMBH in NGC

1275 to be $M_{\text{BH}} = 1.1_{-0.5}^{+0.9} \times 10^9 M_{\odot}$. If take the diameter of the black hole to be twice the Schwarzschild radius $2R_{\text{S}} = 4GM/c^2$, we find a light crossing time of $t_{\text{cross}} = 4GM/c^3 \sim 6$ hours. Thus if we attribute the X-ray emission to the inner accretion disk, the fastest variability we observe in the HETG data ($\sim 20\%$ in 36 hours) corresponds to the light crossing time at a radius of $\sim 10R_{\text{S}}$.

We also consider the relationship between the photon index and 2-10 keV X-ray flux. To extend our analysis, we include the archival *Swift* XRT PC-mode observations. In X-ray terminology, a ‘harder’ photon index describes a shallower power law (relatively less ‘soft’ low-energy X-ray to ‘hard’ high-energy X-ray) while a ‘softer’ photon index describes a steeper power law. Many studies have tried to assess the relationship between photon index and flux (or luminosity) and have arrived at varying conclusions reporting either ‘softer when brighter’ or ‘harder when brighter’ (see e.g. [Gu & Cao 2009](#); [Sobolewska & Papadakis 2009](#); [Younes et al. 2011](#)). The difference in correlation may be related to the classification of the AGN. Analogies have been made between AGN and black hole X-ray binaries (BHXRb) which display a cyclical pattern in hardness vs. flux dictated by the manner of accretion and jet activity (see [Remillard & McClintock \(2006\)](#) and references therein).

Fig. 3.9 shows the 2-10 keV X-ray flux vs photon index Γ for the archival *Swift* and new *Chandra* observations. Sparse *Swift* observations from mid-2007 to mid-2016 show a consistent trend of being harder when brighter (Fig. 3.9 top panel). We note that that several of these *Swift* observation groups were triggered by increases in *Fermi* γ -ray flux ([Fukazawa et al., 2018](#)) which can be seen by comparing the top and bottom panels in Fig. 3.11. The underlying dependence on γ -ray flux may impact the overall trends in

photon index.

In the bottom panel of Fig. 3.9, we find distinctly different trends over a much shorter period of time (~ 1 year). An unusually bright X-ray flare was captured by *Swift* in 2017 January, again in response to a *Fermi* γ -ray trigger (see Fig. 3.11). This flare was unusually hard and bright in the X-ray band (yellow points in bottom panel of Fig. 3.9). Interestingly, the flux and photon index of NGC 1275 is roughly the same immediately before and after the flare. The next group of observations following the 2017 flare are the new *Chandra* HETG observations. These are slightly lower in flux but much softer than the *Swift* immediately following the flare. We note that no attempt has been made to cross-calibrate *Swift* and *Chandra*, and the large difference in photon index should be viewed cautiously. Regardless, we can now show for an individual AGN evidence of it moving in both directions along a ‘harder when brighter’ trend.

We can form an explanation for the trend by referring to a general diagram of a blazar spectral energy distribution (SED), shown in Fig. 3.10. X-ray observations of blazars can often reside in the valley between the radio synchrotron emission from the jet and the γ -ray inverse Compton scattering emission from the jet. Residing at the bottom of the valley is the X-ray emission from the corona and inner accretion disk. We can imagine the photon index becoming softer if the contribution from the jet had decreased sufficiently so that the disk emission would dominate the X-ray band. Conversely, an increase in overall jet activity would increase both the synchrotron and inverse Compton contribution, effectively swamping the disk component and resulting in a harder photon index. In this sense, we can view Fig. 3.9 as an indication of whether the X-ray emission is disk- or jet-dominated.

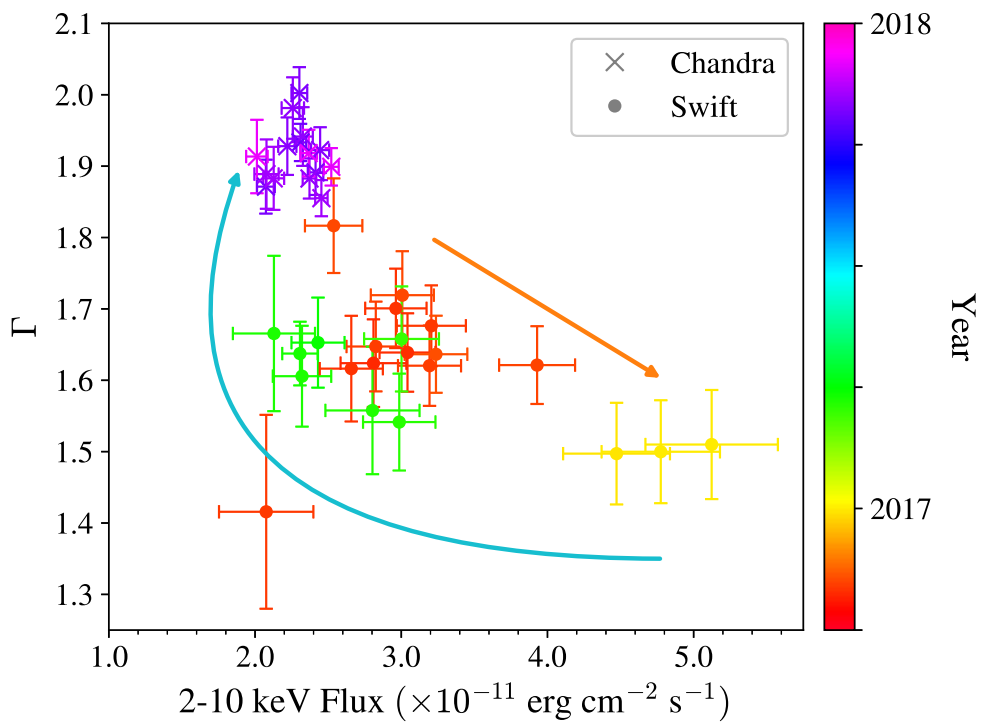
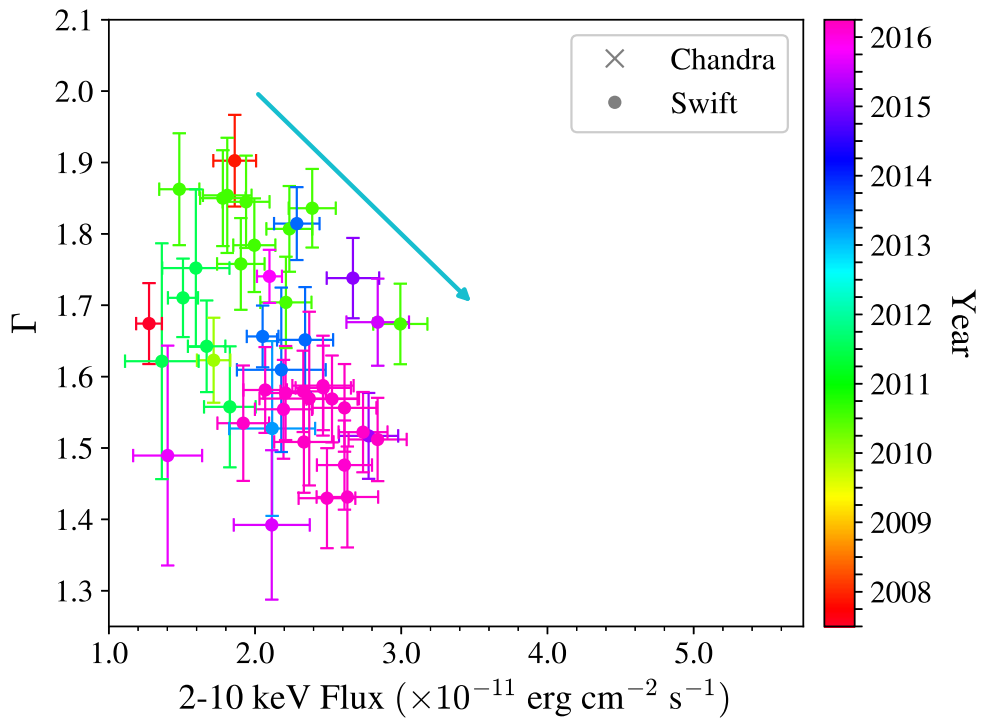


Figure 3.9: Figures of flux vs. Γ for NGC 1275. Observations are colored by date and arrows indicate relative trends with time.

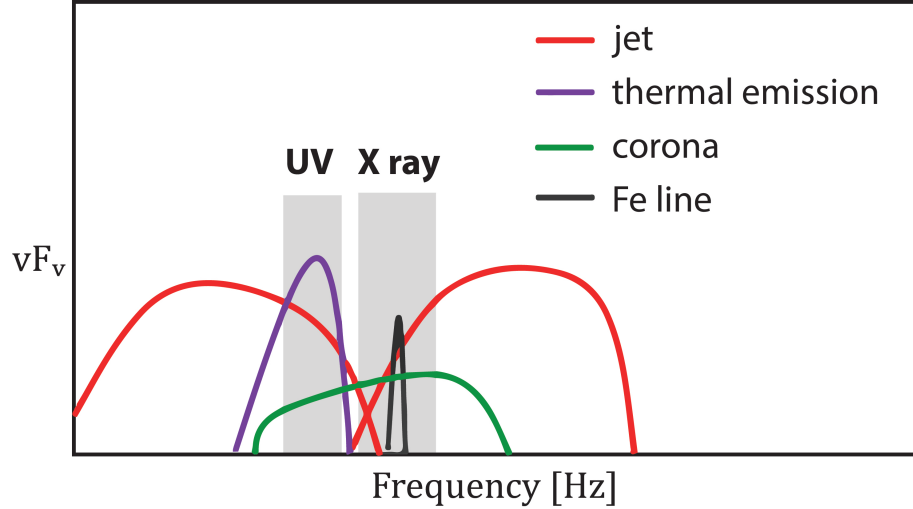


Figure 3.10: Spectral Energy Distribution (SED) diagram for NGC 1275 (and blazars more generally) reproduced from [Imazato et al. \(2021\)](#). The low energy jet emission observed in radio is due to synchrotron emission. The high energy jet emission observed in X-ray and γ -ray is due to inverse Compton scattering.

3.4 Correlated Variability Analysis

Both the optical and γ -ray emission from NGC 1275 are thought to be dominated by the jet ([Fukazawa et al., 2018](#)), the former coming from synchrotron processes and the latter from inverse Compton scattering. Thus, it is interesting to examine the temporal correlations between these bands; this is facilitated by the long ASAS-SN and *Fermi* light curves. In order to explore temporal correlations between the *Fermi* γ -ray and ASAS-SN optical light curves, we use the discrete correlation function (DCF) developed for unevenly sampled light curves ([Edelson & Krolik, 1988](#)). Figure 3.11 shows the X-ray (*Chandra* and *Swift*), optical (ASAS-SN), and γ -ray (*Fermi*) light curves from mid-2007 to 2019. Although it would be interesting to examine correlations with X-ray emission, the X-ray light curve is too sparsely sampled for DCF analysis.

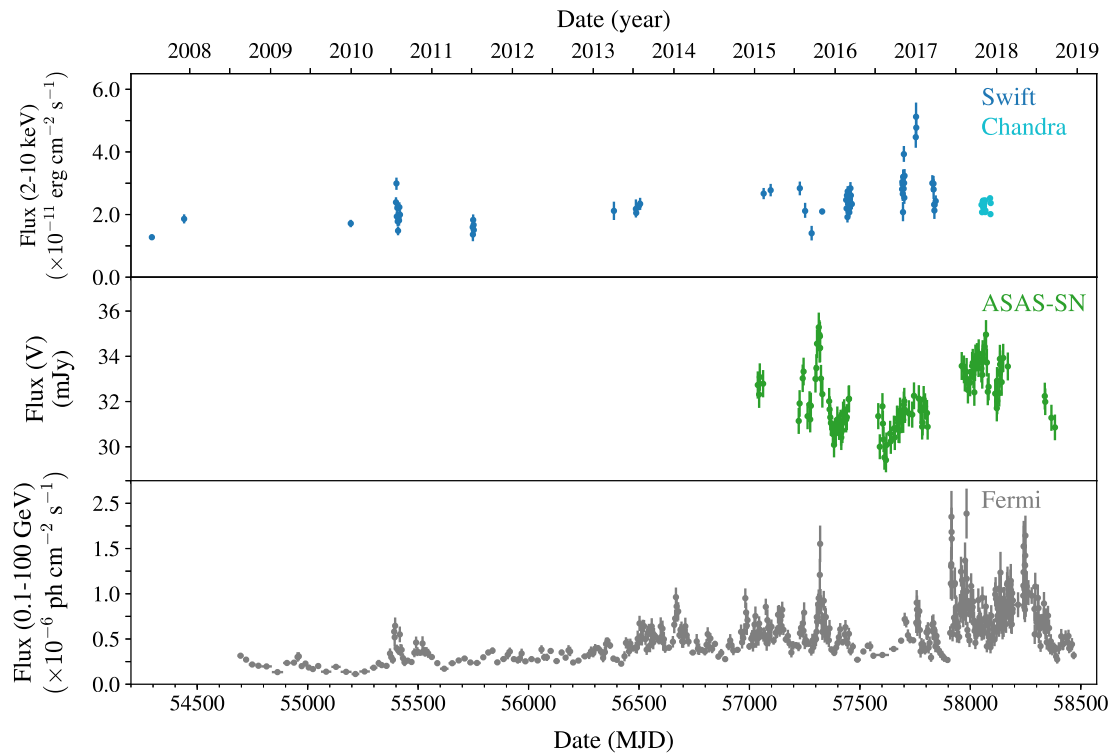


Figure 3.11: Light curve of NGC 1275 from mid-2007 to 2019 including archival *Swift* X-ray observations (blue, top panel), new *Chandra* X-ray observations (cyan, top panel), ASAS-SN optical data (green, middle panel), and *Fermi* γ -ray observations (gray, bottom panel). Host galaxy emission has not been removed from the ASAS-SN observations.

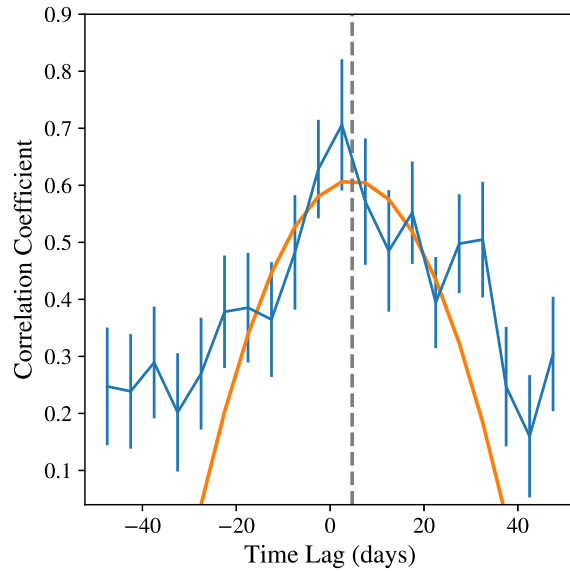


Figure 3.12: Results from discrete correlation function analysis between the ASAS-SN optical and *Fermi* γ -ray light curves. The correlation coefficients (blue) are fit with quadratic (orange) to determine the peak and corresponding time lag (gray dashed vertical) between the two spectra. We find that the optical light curve leads the γ -ray light curve by ~ 5 days from mid-2015 to mid-2016.

Instead, we turn our focus to the optical and γ -ray light curves. Using the DCF applied to the complete ASAS-SN and *Fermi* light curves, we find evidence of the optical light curve leading the γ -ray emission by ~ 5 days. Results from the DCF analysis are shown in Fig. 3.12 where the correlation coefficient for time lags within ± 20 days is fit with a quadratic to determine the lag time. This correlation is primarily driven by a single large optical and γ -ray flare, shown in Fig. 3.13, that occurred in 2015 October. The γ -ray flare correlated with the optical emission is identified as G4 in Hodgson et al. (2018), and they find that the γ -ray flare is coincident with the onset of a long lasting radio flare at 1 mm wavelengths. We note in Fig. 3.13 a smaller ‘flare’ occurring roughly ~ 80 days before G4 in which the optical emission also appears to lead the γ -ray emission. Hodgson et al. (2018) do not identify this feature as a bona fide γ -ray flare, but this does contribute

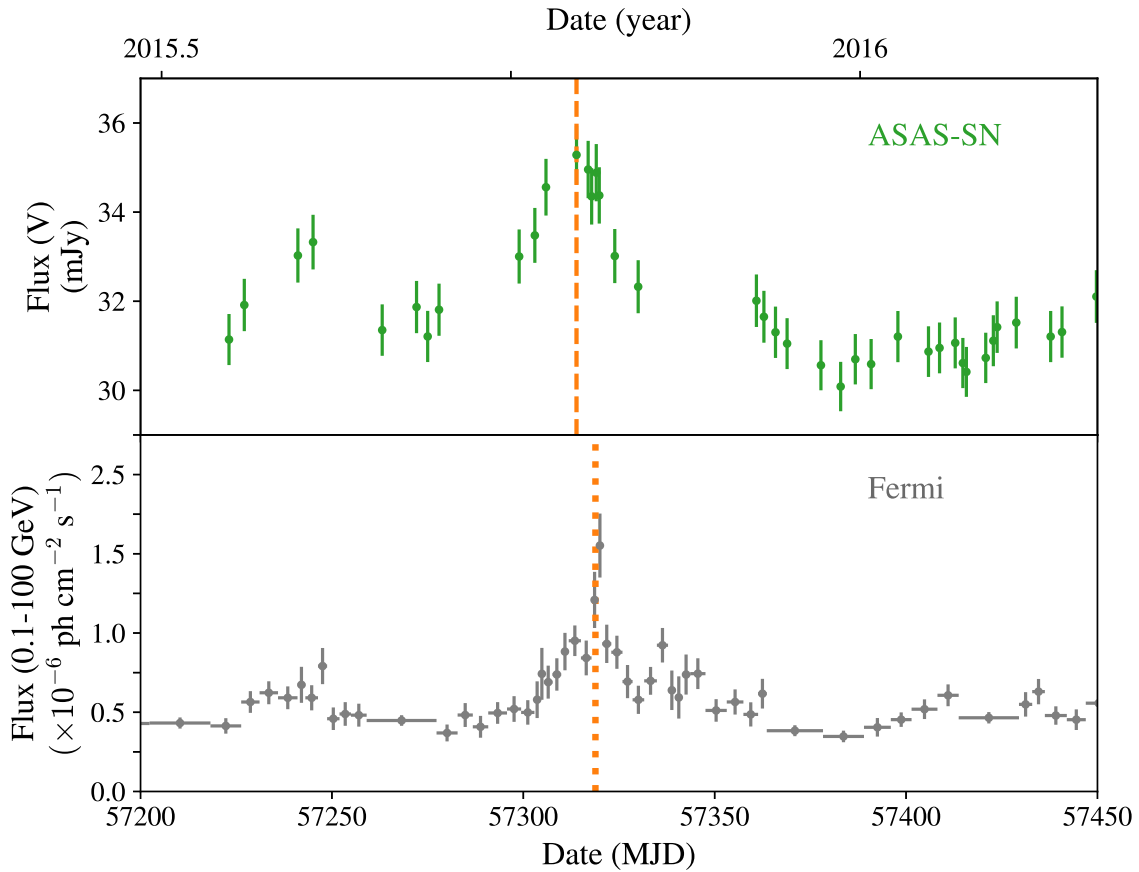


Figure 3.13: Light curve of ASAS-SN optical data (green, top panel) and *Fermi* γ -ray data (gray, bottom panel) from mid-2015 to mid-2016. Orange, dashed or dotted vertical lines indicate the peak of the optical and γ -ray flare, respectively. This section of the light curve is driving the observed time lag of ~ 5 days.

to our DCF results. Interestingly, aside from these two features in late 2015 - early 2016, the optical and γ -ray light curve do not appear obviously correlated at all. Discussion of these results is deferred to §3.5.

To test the robustness of the inferred optical/ γ -ray time lag, we simulated 10 000 light curves using DELightcurveSimulation (DELCgen; Connolly 2016), a Python implementation of the method described in Emmanoulopoulos et al. (2013). When simulating light curves, DELCgen preserves the power spectral density (PSD) and probability density

function (PDF) of the input data light curve. We assume that the observed optical and γ -ray light curves are generated by the same underlying PSD and PDF, and use the *Fermi* light curve to determine the PSD and PDF since it is sampled at higher frequency and over a longer time period.

The PSD can be estimated by the modulus-squared of the discrete Fourier transform of the observed light curve. This method requires an evenly sampled light curve, so we interpolated the adaptively binned *Fermi* light curve with a daily cadence using a cubic spline. We fit the resulting estimated PSD using a smoothly bending power-law defined as

$$\mathcal{P}(\nu) = \frac{A\nu^{-\alpha_{\text{low}}}}{1 + (\nu/\nu_{\text{bend}})^{\alpha_{\text{high}} - \alpha_{\text{low}}}} + c \quad (3.1)$$

where parameters A , ν_{bend} , α_{low} , α_{high} , and c correspond to normalization, bend frequency, low- and high-frequency slopes, and a constant representing the Poisson noise level, respectively. Using a non-linear least squares fit, we find the PSD is well fit by $A = 10.6$ days, $\nu_{\text{bend}} = 0.012 \text{ day}^{-1}$, $\alpha_{\text{low}} = 0.09$, $\alpha_{\text{high}} = 2.36$, and $c = 1 \times 10^{-10}$ days. The PDF of the γ -ray light curve was fit with a lognormal distribution with parameters shape = 0.418, location = -7.188, and scale = 4.439. Fig. 3.14 shows best fits to the PSD and PDF calculated with the interpolated 1-day *Fermi* γ -ray light curve.

With the observed PSD and PDF determined, 10 000 individual light curves were simulated using DELCgen with a cadence of 0.1 day. We assume each simulated light curve to represent a ‘true’ underlying light curve of the AGN which is then filtered to match the dates of the observed *Fermi* and ASAS-SN light curves. The fluxes of the date-filtered simulated light curves are then passed through typical response functions

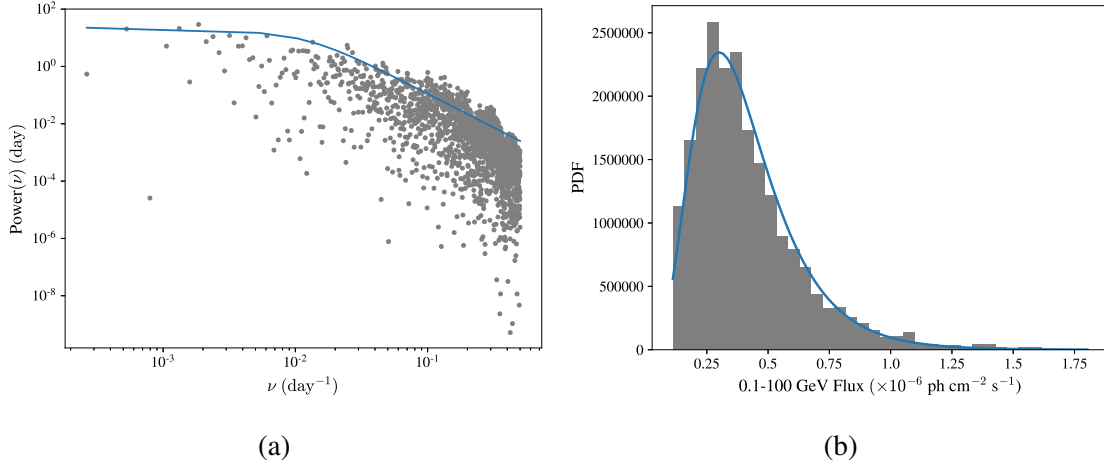


Figure 3.14: (a) The power spectral density (PSD) calculated using the interpolated 1-day *Fermi* γ -ray light curve and fit with a bending power law. (b) The power density function calculated using the interpolated 1-day *Fermi* γ -ray light curve and fit with a lognormal distribution. Both of these model fits were used as input parameters for simulating 10 000 light curves to test our ~ 5 day DCF time lag result.

for *Fermi* and ASAS-SN in order to calculate appropriate Poisson-distributed errors on the simulated fluxes. Thus, each simulated light curve produces both a simulated γ -ray and optical light curve with no intrinsic time delay between them. Fig. 3.15 provides an example of taking a simulated light curve (middle panel) and filtering it to create simulated γ -ray and optical light curves (bottom panel). We note that the simulated optical light curve only models the variable component whereas the real optical light curve includes a constant contribution from the host galaxy. This discrepancy results in an apparently higher amplitude of optical variability in the simulated light curve. However, the increased amplitude does not affect our analysis since the DCF is only sensitive to the variable component anyway.

Fig. 3.16 shows the histogram of time lag peaks for the ten thousand light curve pairs. As expected, the time lag peaks are roughly normally distributed around a time lag of zero, the true intrinsic time lag between the simulated γ -ray and optical light curves.

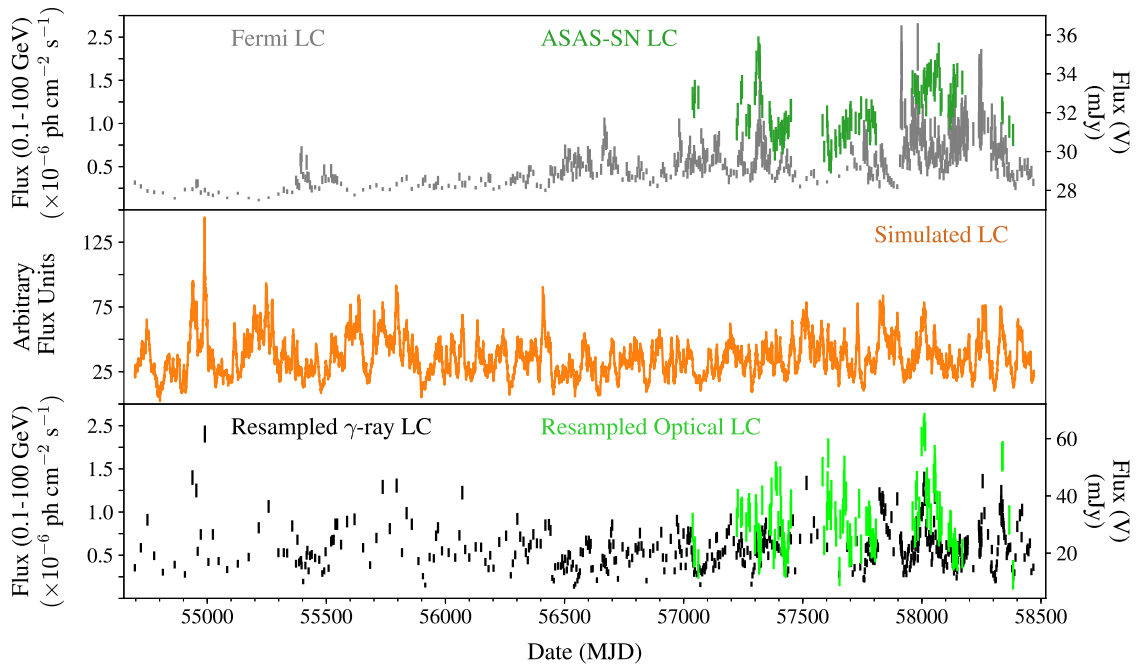


Figure 3.15: Top panel: Observed ASAS-SN optical light curve (green) and *Fermi* γ -ray light curve (gray). Middle panel: One of ten thousand simulated light curves (orange) which preserve the power spectrum and probability density function of the observed light curves. Bottom panel: Final simulated optical (lime) and γ -ray (black) light curves after the single simulated light curve has been date filtered to match the observed ASAS-SN and *Fermi* light curves. Simulated fluxes are also passed through respective telescope response functions and appropriate errors added.

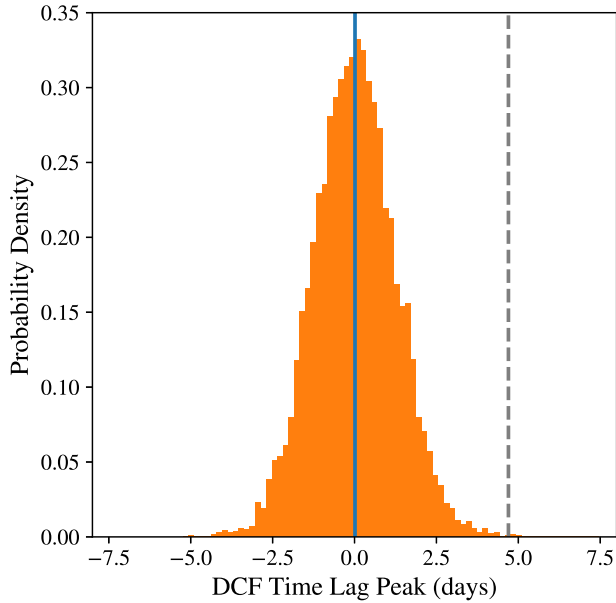


Figure 3.16: Histogram of time lags calculated from ten thousand simulated spectra with no intrinsic time lag. The distribution is approximately normal about zero (cyan vertical line). The gray, dashed, vertical line indicated the ~ 5 day time lag observed in our data. Eight out of ten thousand simulated spectra with no intrinsic time lag produced a measurable time lag greater than ~ 5 days.

Other time lags are found due to a combination of the observing cadence of each light curve, the response functions of the respective telescopes, the amount of time over which observations are available, and the overlap between the two telescopes, among many other factors. The gray vertical dashed line in Fig. 3.16 indicates the time lag found between our observed *Fermi* and ASAS-SN light curves. In our simulation, only eight sets of simulated light curves produced a time lag of larger than 4.7 days when the true simulated AGN light curve had time lag of zero, thus showing that our result of the optical emission leading the γ -ray emission from mid-2015 to mid-2016 by ~ 5 days is significant at a level of 99.92% ($> 3\sigma$).

3.5 Discussion

Our *Chandra* HETG observing campaign produced the first high-resolution spectrum of the AGN in NGC 1275 with minimal contamination from the ICM of the Perseus Cluster and provides a new view of the X-ray variability on day-to-week timescales. We find that NGC 1275 moves on the flux-hardness plane following a general trend of being harder when brighter. This behavior is likely due to the varying contributions of the hard jet and soft disk/corona components. Correlated but time-delayed changes in the relative ratio of the jet to the disk component would be seen as loops or circular motion in the flux-hardness plane. We see tentative evidence for this following an unusually bright X-ray flare in 2017, but this result may be sensitive to cross-calibration issues between *Chandra* and *Swift*. Using the photon index and flux to assess the relative contributions of the jet and disk/corona is an interesting area for future study.

In studying the ASAS-SN optical and γ -ray *Fermi* light curves, we find a highly correlated flare in late 2015 with the optical flare leading the γ -ray flare by ~ 5 days. This result is significant at a level of 99.92% following our Monte-Carlo analysis. While apparent correlations between the optical and γ -ray light curves have been noted ([Aleksić et al., 2014](#)), there have been no previous claims of a short time lag between the two.

Any interpretation of this result must begin with the double-peaked (in νF_ν) jet SED characteristic of blazars (see Fig. 3.10). The optical emission of the low frequency peak is produced by synchrotron emission while the γ -ray emission of the high energy peak is produced by inverse Compton (IC) scattering, presumably by the same electrons producing the synchrotron emission. In such models, there remains a question of where

the low energy photons that seed the IC process originate. Are they the synchrotron photons themselves, so-called synchrotron self-Compton (SSC) emission, or are they external photons such as the CMB or emission from the host galaxy (synchrotron external Compton, SEC)? Our result has potential to shed some light on this question.

We can imagine the following possible scenario to explain the observed optical/ γ -ray delay in flare G4. A knot in the jet (i.e. a blob of fast moving jet plasma) hits the nearly stationary matter in C3. This knot is strongly shocked, increasing its magnetic field which in turn results in an immediate increase in synchrotron emission. Some fraction of these synchrotron photons will then get Compton-upscattered after travelling roughly the size of the knot. Given our measured delay between the γ -ray and optical, we can infer from this picture that the light crossing time of the knot is ~ 5 light days. [Hodgson et al. \(2018\)](#) find that component C3 is moving slowly with measured apparent velocities of $\sim 0.1-0.2c$. We assume that the collision of the relativistic knot with C3 results in post-shocked material that is, at most, only mildly relativistic. Thus the Lorentz factor $\gamma = 1/\sqrt{1 - v^2/c^2}$ is nearly 1 and relativistic effects are not relevant when interpreting the light crossing time.

The above scenario only works if the IC emission is due to synchrotron self-Compton. If instead the γ -ray emission is produced from the Compton-upscattering of external radiation, we would expect the γ -ray flux to rise simultaneously with the increase in optical synchrotron emission. Thus our measured time lag between the γ -ray and optical emission could provide some support to the SSC model.

We note that the radio core of NGC 1275 was unusually active during the period of correlated optical and γ -ray variability. [Hodgson et al. \(2021\)](#) find that the G4 γ -ray flare corresponds to the emergence of a new component, termed EB2, in C3 (see Fig. 3.17,

reproduced from [Hodgson et al. 2021](#)). Flare G4 and the emergence of EB2 occur during the same period where [Kino et al. \(2018\)](#) report a ‘flip’ of the jet head. [Hodgson et al. \(2021\)](#) argue that the ‘flip’ of the jet is actually the emergence of the new EB2 component in a different location than previous activity. The emergence of this new component is also coincident with the increase in 43 GHz flux termed R4. The radio flare, however, is a much slower flare with a sharp increase in flux lagging G4 by ~ 100 days before peaking in mid-2016.

Additionally, [Hodgson et al. \(2021\)](#) find that previous γ -ray flares G1, G2, G3 occur when a small ‘knot’ traveling from C1 to C3 flares at 43 GHz, flares in γ -ray, then splits into two distinct radio emission regions, and then quickly dissipates. While ASAS-SN does not cover the time periods where G1-G3 occur, evidence that different physical processes can create γ -ray flares can help explain why some flares would be correlated with optical while others are not. However, significantly more theoretical work is required to piece together a complete picture that explains the changes in pc-scale radio morphology and the multiwaveband variability.

3.6 Conclusions

Using the *Chandra* HETG, we present the first high-quality, high-resolution spectrum of NGC 1275 with minimal contamination from the ICM of the Perseus Cluster. We find $\sim 10\%$ variations in flux about the mean on day to week timescales. Generally, we find a ‘harder when brighter’ trend with possible evidence for loop-like motion in the flux-hardness plane, which we think can be used to assess changes in the relative contributions

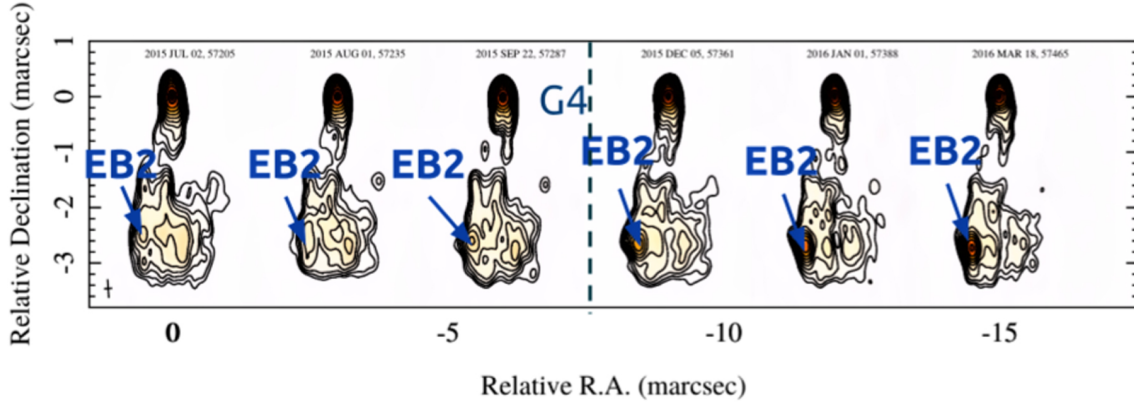


Figure 3.17: 43 GHz VLBI images of C1 and C3 in NGC 1275 showing the emergence of a new component, EB2, in C3. The emergence of the component is coincident with γ -ray flare G4, which exhibits correlated variability with optical emission. Figure reproduced from [Hodgson et al. \(2021\)](#).

to the X-ray from the jet and the disk/corona. Comparing with multiwaveband light curves, we report for the first time a strongly correlated flare in the optical and γ -ray where the optical leads the γ -ray emission by ~ 5 days. These flares are attributed to the emergence of a new component in the pc-scale core of the radio jet. Assuming that the optical emission is produced by synchrotron processes in the jet, the delay in the γ -ray emission could provide support for the picture whereby the γ -ray emission is produced by the Compton-upscattering of the synchrotron radiation (called synchrotron self-Compton) rather than the upscattering of external radiation. NGC 1275 continues to prove a complex and intriguing source for studying emission and feedback processes in AGN.

Chapter 4: *Chandra* Study of Rare Brightest Cluster Galaxy Quasar H1821+643

4.1 Object Overview

In our final case study, we present *Chandra* observations of H1821+643¹, an extremely rare example of a luminous broad-line radio-quiet quasar located in the brightest cluster galaxy (BCG) of a rich cool-core cluster. Located at a redshift of $z=0.297$, the only other comparable object in the local universe ($z < 0.5$) is the obscured quasar IRAS 09104+4109 (O’Sullivan et al., 2012). Among all objects with $z < 0.5$, H1821+643 is one of the most luminous with an estimated bolometric luminosity of 2×10^{47} erg s⁻¹ (Russell et al., 2010) and $m_V = 14.2$ (Kolman et al., 1991). Optical observations reveal that the quasar host galaxy is a large, featureless, and red elliptical galaxy (Hutchings & Neff, 1991).

With a 5 GHz radio luminosity of $10^{23.9}$ W Hz⁻¹ sr⁻¹, H1821+643 is considered ‘radio-quiet’, but its 151 MHz radio luminosity of $10^{25.3}$ W Hz⁻¹ sr⁻¹ is at the observed boundary of Fanaroff-Riley type I (FR I) and FR II structures (Blundell & Rawlings, 2001). Radio-quiet quasars are typically defined by $L_{5 \text{ GHz}} < 10^{24-25}$ W Hz⁻¹ sr⁻¹ (e.g. Wilson & Colbert 1995; Lacy et al. 2002) and are usually located in spiral host galaxies (Wilson & Colbert 1995 and references therein). Belying its radio-quiet classification, a

¹This object also appears in literature as HBN 1821+643, E1821+643, QSO 1821+643 and Q1821+643

1.4 GHz Very Large Array radio image of H1821+643 revealed a giant 300 kpc FR I radio source extending significantly beyond the host galaxy (Fig. 4.1, [Blundell & Rawlings 2001](#)).

H1821+643 is located at the center of a relaxed, cool core cluster where the temperature of the ICM drops from 7-8 keV at $r=100$ kpc down to 2-3 keV within 20 kpc ([Russell et al., 2010](#)). Additionally, the entropy of the core of the cluster is anomalously low compared to similar-mass cool-core clusters ([Walker et al., 2014](#)). The majority of BCGs in cool-core clusters contain at least a modest power radio-loud AGN ([Burns, 1990](#)), thus motivating the accepted solution to the “cooling flow problem” whereby mechanical feedback from AGN offsets the cooling by heating the ICM (see 1.3.2). Given the optical luminosity of H1821+643, previous studies suggest that the quasar may be in fact cooling the ICM via Compton-cooling which dominates the Bremsstrahlung cooling within 5 kpc ([Russell et al., 2010](#); [Walker et al., 2014](#)). A Compton-cooled ICM would make Bondi accretion a viable fuelling mechanism for central quasar, potentially facilitating the growth of an unusually massive black hole ($\gtrsim 10^{10} M_{\odot}$; [Walker et al. 2014](#)). H1821+643 and the surrounding cluster, therefore, provide a unique opportunity to study a highly unusual source which differs from our current understanding of clusters and AGN feedback and which may represent a short-lived phase in evolution of galaxy clusters.

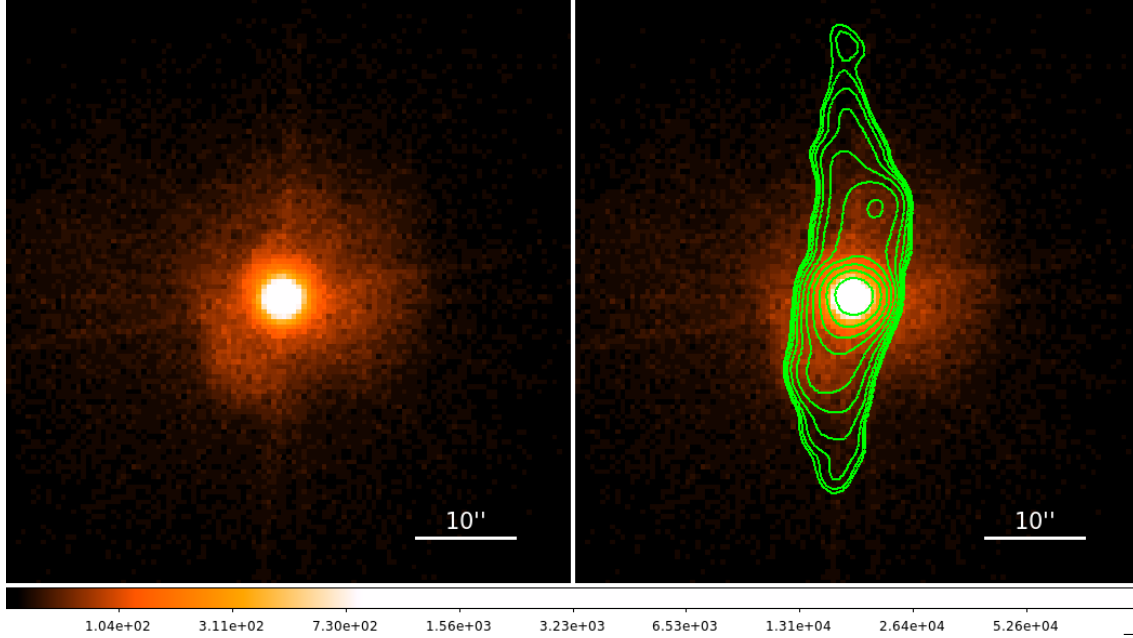


Figure 4.1: Left: Stacked image (~ 580 ks) of new *Chandra* observations of H1821+643 from 0.5-7.0 keV (aligned with ObsID 22106). Right: Stacked image of H1821+643 superimposed with 1.4 GHz VLA radio contours showing a ~ 300 kpc FR I structure (Blundell & Rawlings, 2001).

4.1.0.1 Review of Previous X-ray Observations

H1821+643 was first identified as an AGN when optical spectra revealed a broad-line quasar spectrum as the counterpart to a serendipitous 1980 *Einstein Observatory* X-ray source (Pravdo & Marshall, 1984). With further investigation, Pravdo & Marshall (1984) linked this new source with the previously unidentified observations from 1977-78 made by *HEAO-1/A2* Low Energy Detector labeled as H1814+63 (Nugent et al., 1983) and High Energy Detector labeled as H1824+644 (Marshall et al., 1979). The *HEAO-1* observations indicate an extremely soft X-ray spectrum with a photon index from 0.5-10 keV of 2.31 ± 0.3 , however the *Einstein* imaging proportional counter soft X-ray count rate was a factor of four less than would be expected based on *HEAO-1* observations three years prior (Pravdo & Marshall, 1984). This discrepancy has been explored as both

intrinsic spectral variation in the source or, less likely, as potential confusion with another source by the *HEAO-1* LED (Kolman et al., 1991; Warwick et al., 1989).

EXOSAT observations in 1984-1985 with the medium energy detector and low energy telescope led Warwick et al. 1989 to propose a two-component spectral model with a soft component (<2 keV) which had decreased by an order of magnitude in flux since *HEAO-1* and a hard component (2-10 keV) which had decreased by a factor of two. In this two-component model, both the *HEAO-1* and *EXOSAT* photon indices between 2-10 keV are consistent with a more canonical value of $\Gamma \sim 1.8$ (Warwick et al., 1989). Finally, Warwick et al. (1989) note uncorrelated variability in the soft and hard bands on a week to month timescale as well as the tentative detection of a 6.4 keV rest-frame iron line with an equivalent width of ~ 300 eV. None of the X-ray observations discussed above were able to resolve the cluster.

Schneider et al. (1992) provided spectroscopic evidence that H1821+643 was indeed located within a rich cluster of galaxies (Abell richness ~ 2 ; Lacy et al. 1992). *Ginga* observations from 1987-88 were the first to detect an iron emission line from the ICM at a rest-frame energy of 6.6 ± 0.3 keV and estimate an EW between 60-380 eV due to potential contribution from the galaxy cluster (Kii et al., 1991). The measured photon index of the AGN in these observations was $\Gamma \sim 1.9$ from 1.5-18 keV (Kii et al., 1991). A 1.8 ks observation with *BBXRT* in 1990 found a consistent $\Gamma \sim 1.8$, but did not report any iron emission (Yaqoob et al., 1993); however subsequent analyses found the upper limits on line emission from *BBXRT* to be consistent with *Ginga* emission measurements (Yamashita et al., 1997). Soft X-ray observations with the *ROSAT* High Resolution Imager (HRI; Hall et al. 1997) and Position Sensitive Proportional Counter (PSPC; Saxton

et al. 1997) provided the first definitive evidence that the cluster itself emitted in X-ray, thus marking a turning point in the X-ray literature where additional focus was placed on identifying and separating the quasar and cluster emission. *ASCA* observations confirmed the detection of a mildly broadened iron K emission line at a rest energy of 6.58 ± 0.05 keV and an upper limit of $\sigma < 180$ keV (Yamashita et al., 1997). The measured photon index from 1.5-10 keV was $\Gamma \sim 1.8$, consistent with previous observations, and the overall contribution of the cluster was estimated to be negligible (Yamashita et al., 1997).

With the advent of *Chandra*, the cluster and quasar emissions could more reliably separated. The first *Chandra* High Energy Transmission Grating (HETG) spectra in 2001 isolated the quasar emission and clearly resolved an iron emission line at ~ 6.43 keV (rest frame) with an equivalent width of ~ 100 eV (Fang et al., 2002). A weak detection of a feature at ~ 6.9 keV (rest frame) was also reported. The photon index from 2-10 keV is again broadly consistent with previous observations at $\Gamma = 1.75 \pm 0.05$. Notably, even with the HETG in place, the zeroth order image was piled up $\gtrsim 20\%$ (Fang et al., 2002). Analysis of the same HETG data by Yaqoob & Serlemitsos (2005) suggest a narrow, redshifted absorption line on the red wing of the iron emission line. Additionally, analysis of Low Energy Transmission Grating (LETG) data finds significant detections of two iron emission lines at at rest frame energies of ~ 6.4 keV and ~ 6.9 keV (Yaqoob & Serlemitsos, 2005).

XMM-Newton observations in 2002 confirm the 6.4 keV iron line and find a second ionized line tentatively associated with the cluster (Jiménez-Bailón et al., 2007). *Suzaku* observations in 2013 detect a 6.4 keV iron emission line and find the observed spectrum well-modeled with relativistic reflection (Reynolds et al., 2014). The best-fitting model

has a high inclination accretion disk ($i \sim 57^\circ$), a mild spin constraint of $a \gtrsim 0.4$, and strongly requires a sub-solar iron abundance ($Z \sim 0.4Z_\odot$). This low metallicity uncovers another unusual feature of H1821+643; studies of other similar-mass AGN report metallicities greater by a factor ~ 2 (Patrick et al. 2012; Walton et al. 2013). The sub-solar metallicity of Reynolds et al. (2014) is consistent with the reported iron abundance of the ICM (Russell et al., 2010), which is line with the idea that the H1821+643 is being directly fuelled by the Compton-cooled ICM.

A recent detailed analysis revisits archival *Chandra* grating data (both HETG and LETG) with improved data reduction and models the resulting spectra using relativistic reflection (Sisk-Reynés et al., 2022b, submitted). Relativistic reflection again provides a better fit to the data than simpler power law models with Gaussian emission lines. MCMC methods provide tighter constraints on several model parameters (90% errors): $a = 0.62_{-0.37}^{+0.22}$, $i = 44.6 \pm 3.3$ degrees, and iron abundance $A_{\text{Fe}} = 1.02_{-0.37}^{+1.33}Z_\odot$ (Sisk-Reynés et al., 2022b, submitted).

4.2 New *Chandra* Observations

H1821+643 was observed in Cycle 20 with *Chandra* ACIS-S for a total good exposure of time of ~ 582 ks split over 22 observations taken over the course of approximately one year. Table 4.1 provides information on the individual observations. A previous 90 ks ACIS-S observation of H1821+643 was significantly piled up (pileup fraction $\gtrsim 80\%$; Russell et al. 2010) which prevented any robust study of the central quasar. To mitigate pileup in this new observation, a custom 100 row subarray was selected

on the back-illuminated ACIS-S3 chip, thus reducing the frame time 0.3 seconds. This aggressive reduction in the frame time allows the pileup fraction to be reduced to $\sim 15\%$ (see §4.2.2), opening up the AGN emission for detailed study.

4.2.1 Data Reduction

Data were analyzed using CIAO (Fruscione et al., 2006) version 4.14.0 and CALDB version 4.9.6. The latest calibrations were applied to the raw data by running the standard `chandra_repro` script. Although they are default values, special care was taken to ensure that 1) the pixel randomization parameter was set to the EDSER algorithm (Li et al. 2004; `pix_adj=EDSER`) to allow for subpixel imaging, and 2) that the ACIS VFAINT background cleaning was not applied (`check_vf_pha=no`) due to a known issue where it can incorrectly remove real astronomical events from even moderately bright sources². For on-axis sources, the *Chandra* ACIS PSF is smaller than the ACIS CCD pixels (0.492'' square). The EDSER algorithm repositions events using grade information (which encapsulates the electron charge distribution of the event) to infer the location of an event photon within the pixel. Applying this correction reveals and enhances sub-arcsecond structure in astronomical sources, and for our case, can help better separate the point source from the surrounding cluster.

In order to separate the quasar and the very centrally peaked cluster for spectral extraction, care needed to be taken to determine the center of the quasar point source. To do this, a subpixelated image binned to 0.1 pixel (0.0492'') was created for each observation. Subpixelating the image introduced an unexpected image artifact due to the

²https://cxc.harvard.edu/ciao/why/aciscleanvf.html#real_events

Table 4.1: *Chandra* observation information for H1821+643. The background subtracted count rate is calculated between 0.8-7.0 keV (observed frame) using the 2'' circular source extraction region with standard good grade filtering.

ObsID	Start Date		Exposure (ks)	Count Rate (cnt/s)
	(yyyy-mm-dd)	(MJD)		
22105	2019-10-07	58763.7	36.3	1.09 ± 0.01
22106	2019-10-23	58779.5	45.4	0.98 ± 0.01
23054	2019-12-28	58845.6	41.8	1.16 ± 0.01
23211	2020-04-10	58949.2	18.2	1.19 ± 0.01
21559	2020-04-10	58949.9	25.5	1.19 ± 0.01
21558	2020-04-20	58959.3	42.7	1.16 ± 0.01
21561	2020-05-08	58977.8	24.1	1.04 ± 0.01
23240	2020-05-10	58979.2	22.7	1.03 ± 0.01
22108	2020-05-28	58997.9	13.7	1.07 ± 0.01
22107	2020-06-20	59020.6	34.4	1.18 ± 0.01
21560	2020-07-15	59045.1	32.7	1.18 ± 0.01
23319	2020-07-18	59048.0	20.4	1.16 ± 0.01
23239	2020-07-19	59049.2	39.1	1.13 ± 0.01
22104	2020-08-07	59068.0	20.9	1.08 ± 0.01
23339	2020-08-09	59070.9	14.6	1.08 ± 0.01
23053	2020-08-22	59083.6	22.7	1.10 ± 0.01
22103	2020-09-16	59108.5	13.7	1.08 ± 0.01
22109	2020-09-18	59110.5	22.7	1.05 ± 0.01
24612	2020-09-19	59111.2	27.6	1.05 ± 0.01
24639	2020-09-24	59116.3	30.9	1.03 ± 0.01
24641	2020-09-26	59118.5	22.7	1.01 ± 0.01
24661	2020-09-27	59119.7	9.1	1.00 ± 0.01

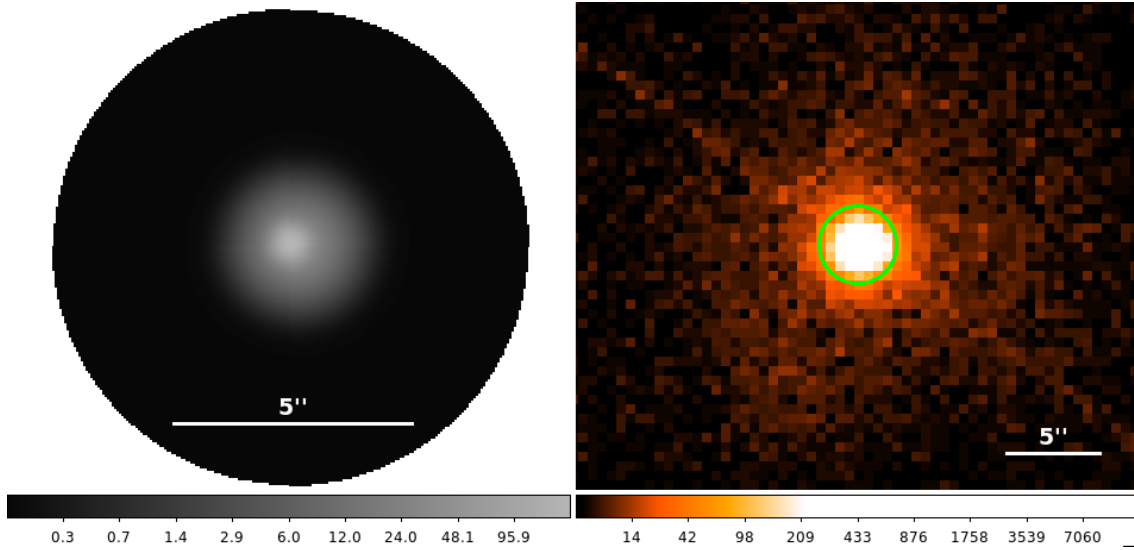


Figure 4.2: Left: The results of fitting two 2-dimensional Gaussians to model the quasar and cluster PSF. The cluster is not symmetric about the quasar, as reported by [Russell et al. 2010](#). Right: Image of observation corresponding to the Gaussian fitting shown. The green circle has a 2'' radius and is centered on centroid of the Gaussian modeling the quasar.

brightness of H1821+643 and *Chandra*'s dither pattern, however, it had minimal impact on the positioning of the point source. Two 2-dimensional Gaussians were fit to the subpixelated image to model the cluster and quasar PSF, and the mean of the centroid of the Gaussian modeling the quasar was used as the center for all subsequent imaging and spectral analyses. Fig. 4.2 shows an example result of the Gaussian fit to ObsID 22106. As previously reported by [Russell et al. 2010](#), the cluster is not symmetric about the quasar, thus producing a point source that appears off-center from the cluster emission. For full discussion of the cluster properties from these new observations, see Russell 2022, in prep.

Spectra and appropriate response files were generated using standard CIAO procedures for a pointlike source³. We consider three different source extraction regions throu-

³<https://exc.cfa.harvard.edu/ciao/threads/pointlike/>

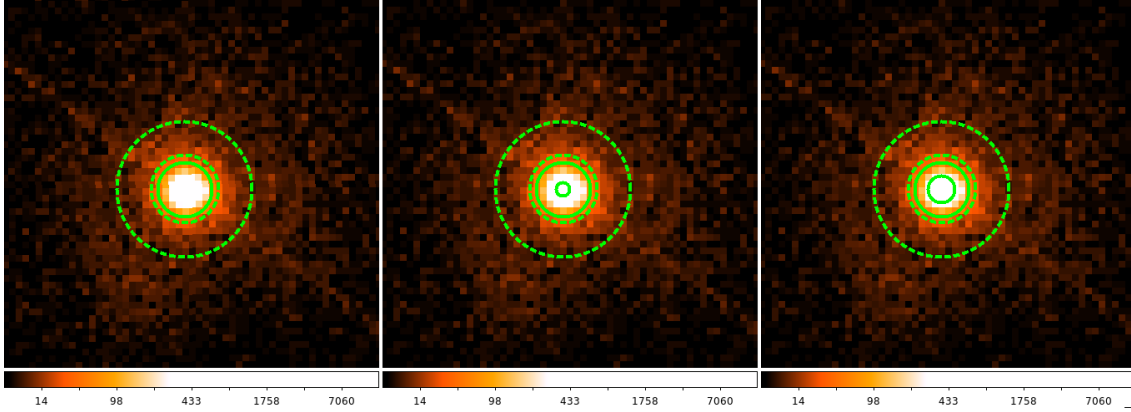


Figure 4.3: ObsID 22106 shown with three different source extraction regions (solid lines) from left to right: (1) a circle with a radius of $2''$, (2) an annulus with inner radius of $0.5''$ and outer radius of $2''$, and (3) an annulus with inner radius of $1.0''$ and outer radius of $2''$. Background annulus (inner radius $2.5''$, outer radius $5.0''$) is shown with dashed lines. The rectangular background region which removes the readout streak is not shown for visual purposes.

ghout our analysis, primarily to address pileup (see §4.2.2). The source regions, shown in Fig. 4.3, include (1) a circle with a radius of $2''$, (2) an annulus with inner radius of $0.5''$ and outer radius of $2''$, and (3) an annulus with inner radius of $1.0''$ and outer radius of $2''$. All source extraction regions used a background region consisting of an annulus with an inner radius of $2.5''$ and an outer radius of $5.0''$. Additionally, the background region excluded a $2''$ wide rectangle which was positioned for each observation to block the readout streak from the background annulus. The background region was chosen to include the cluster emission immediately surrounding the point source since we know the photons in the source region are actually a combination of the quasar and the cluster in which it is embedded. For time-averaged spectra, appropriate response files were created using CIAO `combine_spectra`. All extracted spectra were grouped to a minimum of one count per bin, and the Cash statistic (Cash, 1979) appropriate for Poisson distributed data and background was used for all spectral fitting.

4.2.2 Pileup Assessment

While these new observations were planned to mitigate pileup, WebPIMMS (Mukai, 1993) estimates $\sim 15\%$ pileup in our observations. Upon initial inspection, all of our individual observations contain a mild readout streak in the image, typical of bright sources but encouraging since heavily piled sources have significant readout streaks. There is no formal measure to quantify pileup, but to explore this we examine spectra by eye as well as calculate the ratio of good to bad event grades in radial annuli for each observation.

Fig. 4.4 shows the resulting data/model ratio for a single power law with Galactic absorption ($N_{\text{H}}=3.5 \times 10^{20} \text{ cm}^{-2}$; Kalberla et al. 2005). The data are identically binned for visual purposes. Since pileup is always greatest at the center of the PSF of a point source, our source regions were chosen to progressively remove more of the central PSF. This method removes piled photons at the expense of also removing all non-piled photons in the excluded region. In the top panel of Fig. 4.4 (black points) corresponding to the $2''$ circular extraction, the characteristic hard tail above the ratio=1 line indicative of pileup is clearly present. In subsequent panels where progressively more of the central point source is removed, the hard tail is noticeably diminished while excess flux appears below 1 keV. At least part of the soft excess below 2 keV may be due to emission from the core regions of the ICM. The relative contamination of the ICM will increase as we excise more of the PSF, consistent with the larger soft excess in the annular extractions. The difference in the soft X-ray flux between the circular and annular extractions is also partially explained by the energy migration caused by pileup whereby soft photons are shifted to higher energies.

ObsID 21560

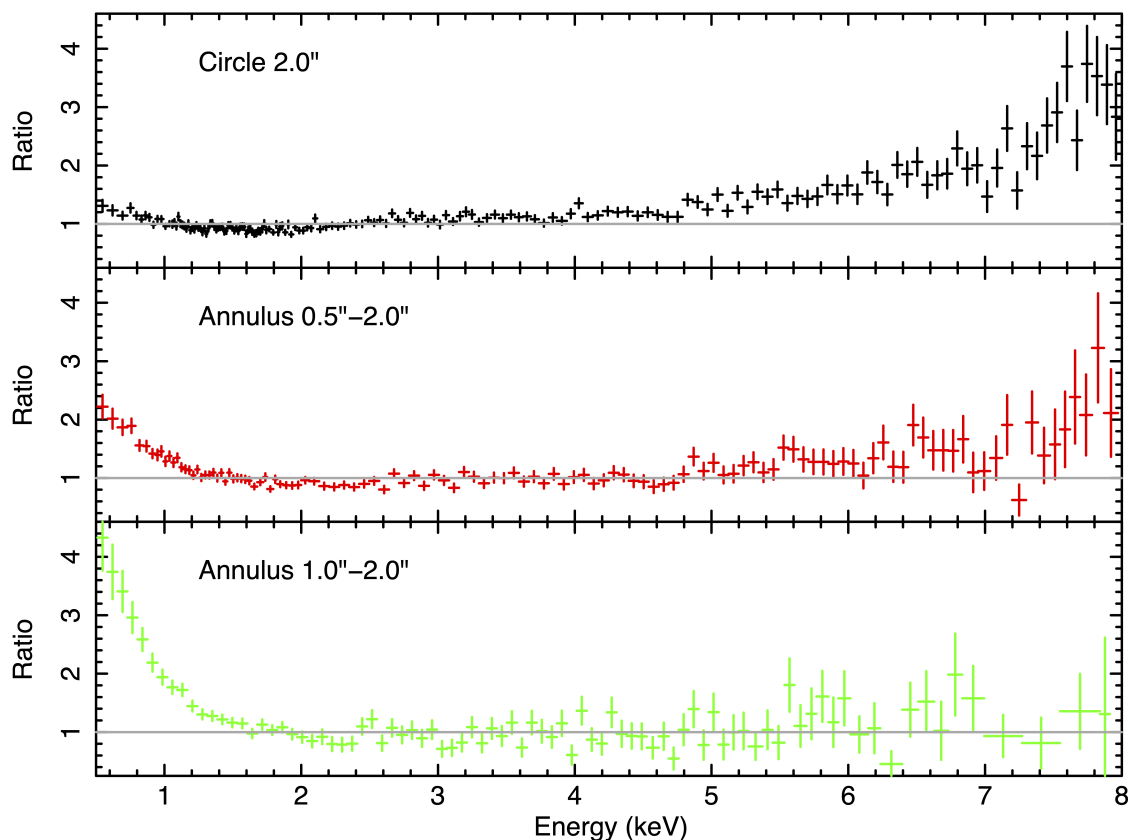


Figure 4.4: Data to model ratio for spectra created with three different source extraction regions and fit with a single power law with Galactic absorption. Energies are plotted in the observed frame. From top to bottom, more of the central PSF of the quasar point source is excluded, corresponding to both a decrease in residuals at high energies indicative of pileup but also the decrease in signal to noise. Spectra are visually binned at the same level.

The effect of also removing any non-piled photons in the annular extractions can be seen in the diminishing signal to noise from the top to bottom panel.

To provide a more rigorous examination of pileup, we compute the net counts in evenly spaced radial annuli for each observation. We then calculate the ratio of ‘bad’ grade (grades 1, 5, 7) to ‘good grade’ (grades 0, 2, 3, 4, 6) counts. This ratio can be used as a proxy to estimate pileup fraction due to event migration (see §1.5.2.1) and assuming that the majority of ‘bad’ grades are the result of piled up photons. Fig. 4.5

shows resulting bad/good ratio further separated by low and high energy bands for a lower count rate ObsID (a) and a higher count rate ObsID (b). The high energy counts are dominated by the quasar which is substantially brighter than the surrounding cluster and manifests as a larger bad/good count ratio at small radii. Since the amount of pileup is proportional to the count rate, the bad/good count ratio is also greater for the higher count rate observation. Assuming the bad/good ratio count rate at high energies is indicative of the pileup in the observed quasar emission, we estimate a pileup fraction of $\sim 20\%$, in line with the amount predicted by WebPIMMS.

Fig. 4.5 can be compared with Fig. 2 in [Russell et al. \(2010\)](#) where the bad/good grade count ratio for H1821+643 at high energy was nearly one. We note that while not ideal, a pileup fraction in the range of $\sim 15\text{-}20\%$ is considered mild, and the choice of subarray to decrease frame readout time was quite successful in reducing pileup for H1821+643. Specifically, it reduces pileup to a level that can be handled by the pileup model in XSPEC when performing spectral analysis (§4.5).

4.2.2.1 Grade 0 Spectrum

We explored creating spectra using only grade 0 events rather than the standard good grade filtering which includes grades 2, 3, 4, and 6. Since grade 0 events correspond to photon events that create a cloud charge in exactly one pixel only (see §1.5.2.1), we can be nearly certain that these photons are *not* piled up. This approach is unusual because grade 0 events are typically only a small fraction of the total good events, and limiting analysis to only grade 0 severely compromises the signal to noise ratio. However, it has

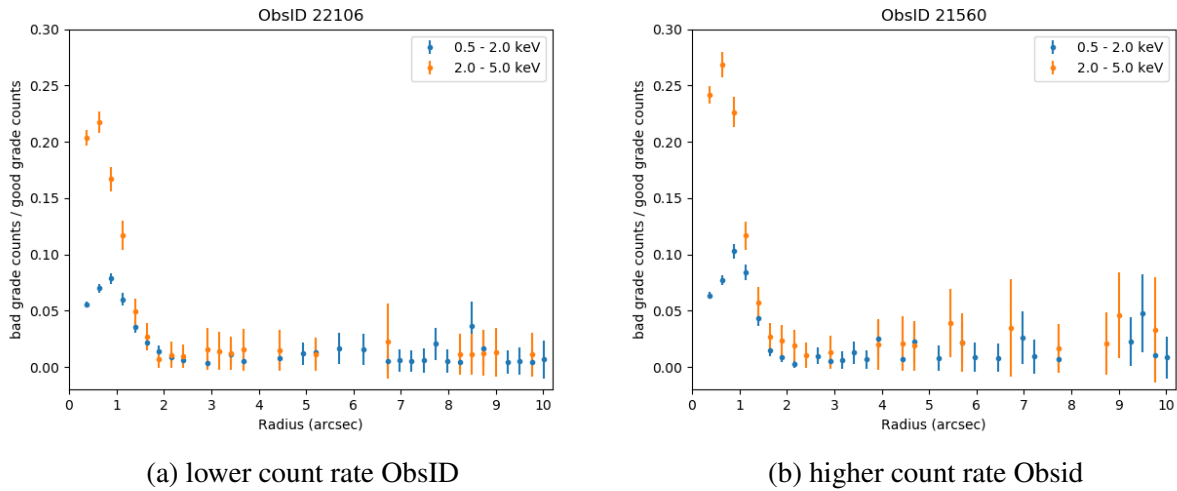


Figure 4.5: Ratio of ‘bad’ to ‘good’ event grades computed at increasing radial annuli for a lower count rate observation and higher count rate observation. The high energy ratio (orange) dominated by the quasar indicates a pileup fraction of $\sim 20\%$.

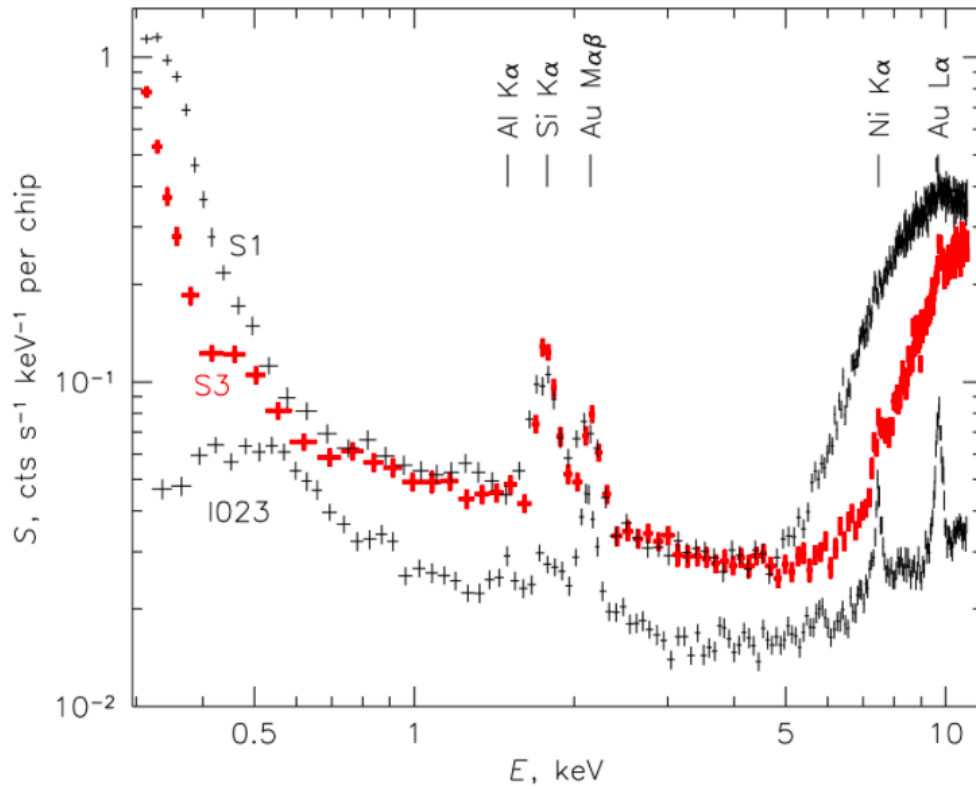
been applied with some success to the ACIS data on NGC 1275 by [Miller et al. \(2017\)](#). Between 0.5-5.0 keV (observed frame), grade 0 events comprise $\sim 24\%$ of the total good events. The percentage of grade 0 events between 0.5-2.0 keV and 2.0-5.0 is $\sim 35\%$ and $\sim 15\%$ respectively. As expected, there are fewer grade 0 events at higher energies which are dominated by the brighter and more piled quasar point source. Given that our source is extremely bright, we retain a reasonable signal to noise in spectra extracted with only grade 0 events. For grade 0 spectra, we use the 2” radius circular extraction since we have ostensibly removed all piled up photons and do not need to exclude any of the central PSF.

Upon inspection of the grade 0 spectrum, however, we discover that we become sensitive to the particle background of the ACIS detector (*Chandra* X-ray Center Helpdesk, private correspondence). At all times, the spacecraft is subject to the charged particle background which can interact and induce fluorescence of the actual detector

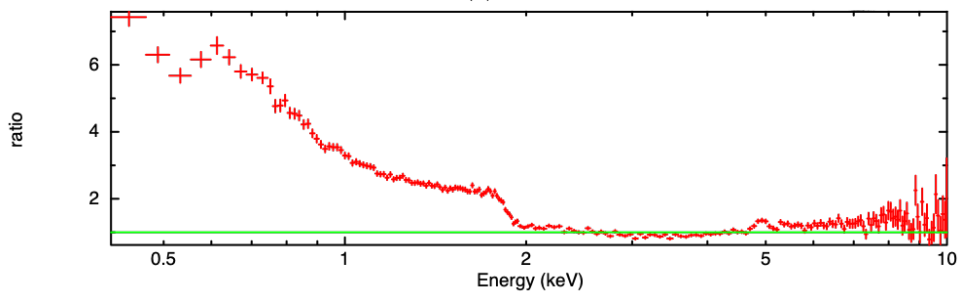
material. Fig. 4.6 shows the ACIS particle background spectrum which can be compared with our combined grade 0 spectrum. We fit our grade 0 spectrum with a single power law from 3-7 keV (observed frame), where the particle background is less noticeable, and then plot the residuals of that model across the full observed energy range. The Si $K\alpha$ fluorescent line at 1.83 keV is pronounced in our grade 0 spectrum. This feature is also visible in our individual observations.

In addition to the particle background, there are no calibration files specifically for grade 0 event filtering. The only available calibration files are for the set of standard good event grades and would not include the energy-dependence in the grade 0 ratio. Those calibration files are applied to all of our grade 0 spectra, and so some of the excess below 2 keV may well be an effect of improper calibration. Disentangling the contributions of the particle background, improper calibration, and the previously observed soft-excess intrinsic to the quasar is not trivial. We note that even just modeling the hard-band (>2 keV) grade 0 data gives a photon index far flatter than any previous measurement.

In short, we do not deem the grade 0 spectra suitable for detailed spectral modeling. We do note that the Fe $K\alpha$ line is clearly visible in the residuals shown in Fig. 4.6b. We do use the individual grade 0 spectra for broad-band modeling of the continuum (§4.3), but those results should be interpreted understanding the limitations of the grade 0 event filtering.



(a)



(b)

Figure 4.6: (a) Particle background spectrum of the ACIS detector in stowed position (CXC POG, 2021). (b) Combined 2'' source region spectrum filtered for grade 0 events fit with a single power law. Our observation was taken with the S3 chip. Model residuals are plotted in the observed frame. The edge around 1.8 keV corresponds to the Si $K\alpha$ line and is not astrophysical.

4.3 X-ray Light Curves

Having characterized the role of pileup in these new data, we proceed to examine the time variability of H1821+643 during the year of this campaign. Using a single power law spectra model with Galactic absorption ($N_{\text{H}}=3.5\times 10^{20} \text{ cm}^{-2}$), we fit our three source extraction regions with both the standard good grade filtering as well as our grade 0 spectra, considering three different energy bands (defined in the observed frame to best maximize our data quality): (1) broad 0.8-7.0 keV, (2) low 0.8-2.0 keV, and (3) high 2.0-7.0 keV. Table 4.2 presents the resulting fluxes and photon indices for each observation. Listed errors are $1-\sigma$. Light curves for each energy band and extraction region are presented in Fig. 4.7. In Fig. 4.7a, the effect of source extraction region on the calculated flux is clearly apparent with the maximum flux corresponding to the 2'' radius circle with all good grades and the minimum flux, a factor of five lower, corresponding to the 1.0''-2.0'' annular region.

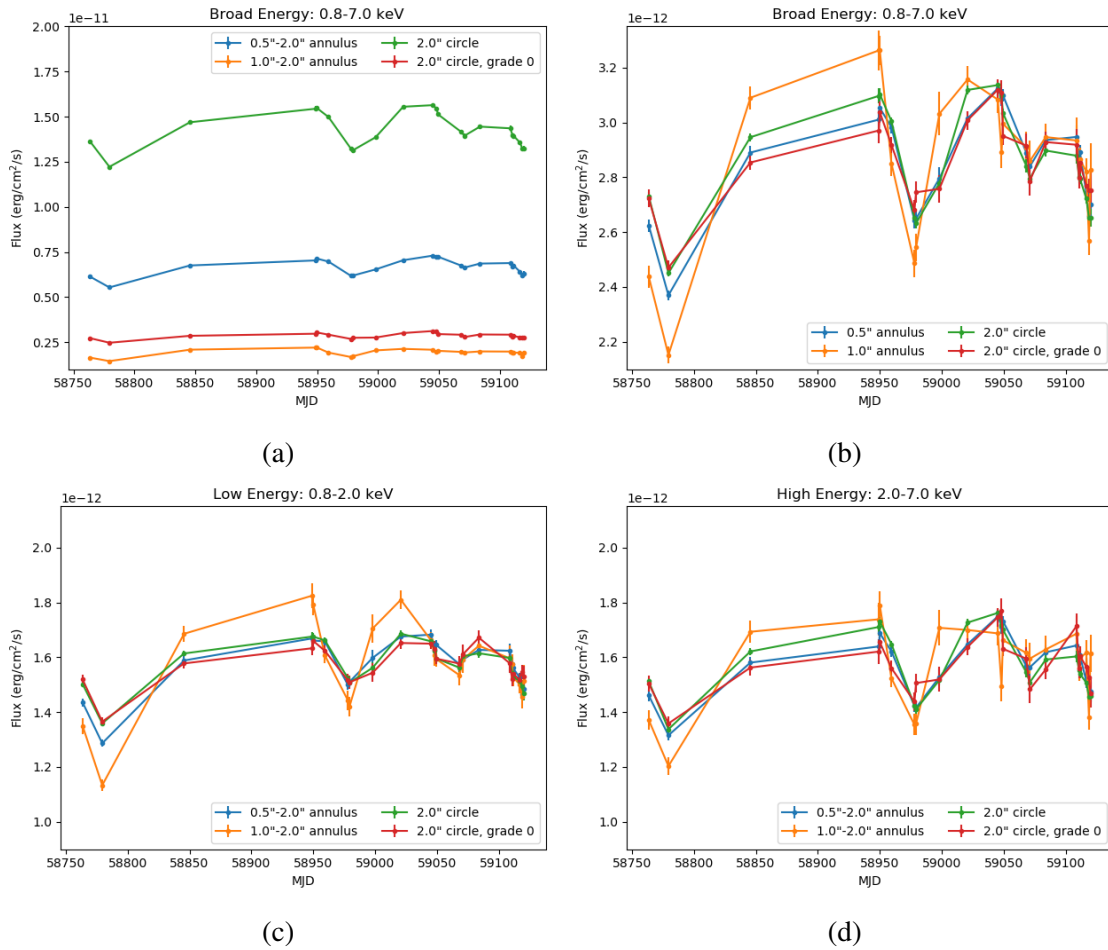


Figure 4.7: X-ray light curves for H1821+643 using four different spectral extractions. (a) shows the unnormalized flux to highlight the effect of the source extraction region and grade filtering. (b-d) show the flux normalized to the mean of the grade 0 light curve in the respective energy band for direct comparison between energy bands and spectral extractions. Energy bands are defined in the observed frame.

Table 4.2: Fluxes and photon indices in three observed frame energy bands (broad=[0.8-7.0] keV, low=[0.8-2.0] keV, high=[2.0-7.0] keV) for all source extraction regions fit using a single power law modified with Galactic absorption. Errors are quoted at a level of $1-\sigma$.

ObsID	Spectra	Γ_{broad}	F_{broad} (10^{-12} erg cm^{-2} s^{-1})	Γ_{low}	F_{low} (10^{-12} erg cm^{-2} s^{-1})	Γ_{high}	F_{high} (10^{-12} erg cm^{-2} s^{-1})
22105	2" circle	1.69 ± 0.01	13.60 ± 0.07	2.15 ± 0.03	4.64 ± 0.03	1.44 ± 0.02	9.57 ± 0.08
	0.5" annulus	1.98 ± 0.02	6.13 ± 0.05	2.61 ± 0.04	2.58 ± 0.02	1.56 ± 0.04	3.99 ± 0.06
	1.0" annulus	2.35 ± 0.04	1.65 ± 0.03	3.29 ± 0.08	0.87 ± 0.02	1.55 ± 0.09	0.99 ± 0.03
	grade 0	2.41 ± 0.02	2.72 ± 0.03	2.59 ± 0.05	1.52 ± 0.02	1.34 ± 0.06	1.50 ± 0.03
22106	2" circle	1.71 ± 0.01	12.20 ± 0.06	2.12 ± 0.03	4.20 ± 0.03	1.51 ± 0.02	8.47 ± 0.07
	0.5" annulus	1.98 ± 0.02	5.54 ± 0.04	2.58 ± 0.04	2.31 ± 0.02	1.58 ± 0.04	3.59 ± 0.05
	1.0" annulus	2.28 ± 0.03	1.45 ± 0.02	3.12 ± 0.08	0.73 ± 0.01	1.72 ± 0.08	0.87 ± 0.02
	grade 0	2.40 ± 0.02	2.47 ± 0.03	2.60 ± 0.05	1.37 ± 0.02	1.42 ± 0.06	1.36 ± 0.03
23054	2" circle	1.69 ± 0.01	14.70 ± 0.07	2.16 ± 0.03	4.99 ± 0.03	1.51 ± 0.02	10.26 ± 0.08
	0.5" annulus	2.00 ± 0.01	6.75 ± 0.05	2.60 ± 0.04	2.85 ± 0.03	1.68 ± 0.04	4.31 ± 0.05
	1.0" annulus	2.33 ± 0.03	2.09 ± 0.03	3.21 ± 0.07	1.09 ± 0.02	1.77 ± 0.08	1.22 ± 0.03
	grade 0	2.39 ± 0.02	2.85 ± 0.03	2.54 ± 0.05	1.58 ± 0.02	1.40 ± 0.06	1.56 ± 0.03
23211	2" circle	1.67 ± 0.01	15.40 ± 0.13	2.08 ± 0.04	5.18 ± 0.05	1.48 ± 0.03	10.83 ± 0.11
	0.5" annulus	2.00 ± 0.02	7.03 ± 0.08	2.57 ± 0.06	3.00 ± 0.04	1.65 ± 0.05	4.47 ± 0.07
	1.0" annulus	2.37 ± 0.04	2.20 ± 0.05	3.13 ± 0.10	1.18 ± 0.03	1.74 ± 0.11	1.25 ± 0.04
	grade 0	2.39 ± 0.03	2.97 ± 0.05	2.47 ± 0.07	1.63 ± 0.03	1.42 ± 0.08	1.62 ± 0.04

ObsID	Spectra	Γ_{broad}	F_{broad} (10^{-12} erg cm^{-2} s^{-1})	Γ_{low}	F_{low} (10^{-12} erg cm^{-2} s^{-1})	Γ_{high}	F_{high} (10^{-12} erg cm^{-2} s^{-1})
21559	2" circle	1.66 ± 0.01	15.50 ± 0.11	2.16 ± 0.03	5.18 ± 0.04	1.46 ± 0.03	10.95 ± 0.10
	0.5" annulus	1.97 ± 0.02	7.13 ± 0.06	2.61 ± 0.05	2.98 ± 0.04	1.67 ± 0.05	4.60 ± 0.07
	1.0" annulus	2.32 ± 0.04	2.20 ± 0.04	3.15 ± 0.09	1.16 ± 0.02	1.67 ± 0.09	1.29 ± 0.04
	grade 0	2.37 ± 0.03	3.04 ± 0.04	2.45 ± 0.06	1.66 ± 0.02	1.40 ± 0.07	1.66 ± 0.04
21558	2" circle	1.70 ± 0.01	15.00 ± 0.07	2.17 ± 0.03	5.13 ± 0.03	1.52 ± 0.02	10.43 ± 0.08
	0.5" annulus	2.01 ± 0.01	6.97 ± 0.05	2.63 ± 0.04	2.98 ± 0.03	1.71 ± 0.04	4.42 ± 0.06
	1.0" annulus	2.38 ± 0.03	1.92 ± 0.03	3.28 ± 0.07	1.04 ± 0.02	1.81 ± 0.07	1.10 ± 0.02
	grade 0	2.42 ± 0.02	2.92 ± 0.03	2.56 ± 0.05	1.62 ± 0.02	1.57 ± 0.06	1.56 ± 0.03
21561	2" circle	1.75 ± 0.01	13.20 ± 0.09	2.18 ± 0.04	4.71 ± 0.04	1.56 ± 0.03	9.02 ± 0.09
	0.5" annulus	2.04 ± 0.02	6.17 ± 0.07	2.61 ± 0.05	2.69 ± 0.04	1.67 ± 0.05	3.88 ± 0.06
	1.0" annulus	2.41 ± 0.04	1.68 ± 0.03	3.30 ± 0.10	0.93 ± 0.02	1.53 ± 0.11	0.97 ± 0.03
	grade 0	2.44 ± 0.03	2.68 ± 0.04	2.60 ± 0.07	1.52 ± 0.02	1.45 ± 0.08	1.44 ± 0.03
23240	2" circle	1.75 ± 0.01	13.10 ± 0.09	2.18 ± 0.04	4.66 ± 0.04	1.60 ± 0.03	8.93 ± 0.09
	0.5" annulus	2.05 ± 0.02	6.19 ± 0.07	2.68 ± 0.06	2.71 ± 0.03	1.73 ± 0.05	3.86 ± 0.06
	1.0" annulus	2.37 ± 0.04	1.72 ± 0.03	3.17 ± 0.10	0.92 ± 0.02	1.81 ± 0.11	0.98 ± 0.03
	grade 0	2.38 ± 0.03	2.75 ± 0.04	2.52 ± 0.07	1.51 ± 0.03	1.35 ± 0.08	1.51 ± 0.03
22108	2" circle	1.72 ± 0.02	13.90 ± 0.13	2.16 ± 0.05	4.82 ± 0.06	1.49 ± 0.04	9.60 ± 0.13
	0.5" annulus	2.03 ± 0.03	6.53 ± 0.10	2.73 ± 0.07	2.87 ± 0.05	1.58 ± 0.06	4.17 ± 0.08
	1.0" annulus	2.34 ± 0.05	2.05 ± 0.05	3.45 ± 0.13	1.10 ± 0.03	1.59 ± 0.13	1.23 ± 0.05
	grade 0	2.40 ± 0.04	2.76 ± 0.05	2.59 ± 0.09	1.54 ± 0.03	1.34 ± 0.10	1.52 ± 0.05

ObsID	Spectra	Γ_{broad}	F_{broad} (10^{-12} erg cm^{-2} s^{-1})	Γ_{low}	F_{low} (10^{-12} erg cm^{-2} s^{-1})	Γ_{high}	F_{high} (10^{-12} erg cm^{-2} s^{-1})
22107	2" circle	1.67 ± 0.01	15.50 ± 0.08	2.11 ± 0.03	5.21 ± 0.04	1.47 ± 0.02	10.93 ± 0.08
	0.5" annulus	2.00 ± 0.02	7.04 ± 0.06	2.63 ± 0.04	3.01 ± 0.03	1.66 ± 0.04	4.49 ± 0.06
	1.0" annulus	2.39 ± 0.03	2.13 ± 0.03	3.31 ± 0.08	1.17 ± 0.02	1.68 ± 0.08	1.22 ± 0.03
	grade 0	2.38 ± 0.02	3.01 ± 0.03	2.48 ± 0.05	1.65 ± 0.02	1.46 ± 0.06	1.64 ± 0.03
21560	2" circle	1.63 ± 0.01	15.60 ± 0.09	2.07 ± 0.03	5.12 ± 0.04	1.39 ± 0.02	11.15 ± 0.10
	0.5" annulus	1.94 ± 0.02	7.30 ± 0.06	2.55 ± 0.04	3.02 ± 0.04	1.53 ± 0.04	4.77 ± 0.06
	1.0" annulus	2.29 ± 0.03	2.08 ± 0.03	3.01 ± 0.08	1.07 ± 0.02	1.66 ± 0.08	1.21 ± 0.03
	grade 0	2.30 ± 0.02	3.12 ± 0.04	2.35 ± 0.06	1.65 ± 0.02	1.35 ± 0.06	1.75 ± 0.03
23319	2" circle	1.63 ± 0.01	15.40 ± 0.11	1.96 ± 0.04	5.01 ± 0.05	1.46 ± 0.03	10.88 ± 0.11
	0.5" annulus	1.92 ± 0.02	7.22 ± 0.07	2.38 ± 0.06	2.92 ± 0.04	1.60 ± 0.05	4.67 ± 0.07
	1.0" annulus	2.38 ± 0.04	1.95 ± 0.04	3.01 ± 0.10	1.04 ± 0.02	1.90 ± 0.11	1.08 ± 0.04
	grade 0	2.29 ± 0.03	3.11 ± 0.04	2.37 ± 0.07	1.63 ± 0.03	1.31 ± 0.08	1.77 ± 0.05
23239	2" circle	1.63 ± 0.01	15.10 ± 0.08	2.04 ± 0.03	4.93 ± 0.03	1.42 ± 0.02	10.76 ± 0.08
	0.5" annulus	1.93 ± 0.02	7.24 ± 0.05	2.48 ± 0.04	2.95 ± 0.03	1.57 ± 0.04	4.72 ± 0.05
	1.0" annulus	2.27 ± 0.03	2.02 ± 0.03	3.10 ± 0.07	1.03 ± 0.02	1.77 ± 0.08	1.20 ± 0.03
	grade 0	2.35 ± 0.02	2.95 ± 0.03	2.46 ± 0.05	1.59 ± 0.02	1.45 ± 0.06	1.63 ± 0.03
22104	2" circle	1.70 ± 0.01	14.20 ± 0.12	2.05 ± 0.04	4.82 ± 0.05	1.54 ± 0.03	9.78 ± 0.10
	0.5" annulus	1.98 ± 0.02	6.75 ± 0.08	2.46 ± 0.06	2.83 ± 0.04	1.67 ± 0.05	4.28 ± 0.07
	1.0" annulus	2.26 ± 0.04	1.96 ± 0.04	2.97 ± 0.10	0.99 ± 0.02	1.64 ± 0.11	1.16 ± 0.04
	grade 0	2.36 ± 0.03	2.92 ± 0.05	2.39 ± 0.07	1.58 ± 0.03	1.42 ± 0.08	1.59 ± 0.04

ObsID	Spectra	Γ_{broad}	F_{broad} (10^{-12} erg cm^{-2} s^{-1})	Γ_{low}	F_{low} (10^{-12} erg cm^{-2} s^{-1})	Γ_{high}	F_{high} (10^{-12} erg cm^{-2} s^{-1})
23339	2" circle	1.74 ± 0.02	13.90 ± 0.11	2.16 ± 0.05	4.95 ± 0.06	1.49 ± 0.04	9.55 ± 0.13
	0.5" annulus	2.00 ± 0.03	6.63 ± 0.08	2.67 ± 0.07	2.86 ± 0.05	1.59 ± 0.06	4.26 ± 0.09
	1.0" annulus	2.33 ± 0.05	1.93 ± 0.05	3.21 ± 0.12	1.03 ± 0.03	1.55 ± 0.13	1.15 ± 0.04
	grade 0	2.48 ± 0.04	2.79 ± 0.05	2.63 ± 0.08	1.61 ± 0.03	1.32 ± 0.10	1.48 ± 0.05
23053	2" circle	1.70 ± 0.01	14.40 ± 0.11	2.15 ± 0.04	4.99 ± 0.05	1.47 ± 0.03	10.08 ± 0.09
	0.5" annulus	1.99 ± 0.02	6.86 ± 0.07	2.64 ± 0.05	2.92 ± 0.04	1.63 ± 0.05	4.41 ± 0.07
	1.0" annulus	2.33 ± 0.04	1.99 ± 0.03	3.27 ± 0.10	1.06 ± 0.02	1.69 ± 0.10	1.17 ± 0.04
	grade 0	2.46 ± 0.03	2.93 ± 0.04	2.66 ± 0.07	1.67 ± 0.03	1.49 ± 0.08	1.56 ± 0.04
22103	2" circle	1.68 ± 0.02	14.40 ± 0.14	2.20 ± 0.05	4.93 ± 0.06	1.37 ± 0.04	10.15 ± 0.13
	0.5" annulus	1.97 ± 0.03	6.88 ± 0.10	2.59 ± 0.07	2.92 ± 0.05	1.49 ± 0.06	4.48 ± 0.09
	1.0" annulus	2.28 ± 0.05	1.98 ± 0.06	3.32 ± 0.13	1.03 ± 0.03	1.59 ± 0.13	1.21 ± 0.05
	grade 0	2.32 ± 0.04	2.92 ± 0.06	2.61 ± 0.09	1.58 ± 0.04	1.21 ± 0.10	1.71 ± 0.05
22109	2" circle	1.68 ± 0.01	14.00 ± 0.11	2.19 ± 0.04	4.76 ± 0.05	1.45 ± 0.03	9.83 ± 0.10
	0.5" annulus	1.97 ± 0.02	6.69 ± 0.07	2.71 ± 0.06	2.83 ± 0.04	1.61 ± 0.05	4.36 ± 0.07
	1.0" annulus	2.33 ± 0.04	1.92 ± 0.04	3.30 ± 0.10	1.02 ± 0.02	1.78 ± 0.11	1.12 ± 0.03
	grade 0	2.36 ± 0.03	2.80 ± 0.04	2.55 ± 0.07	1.52 ± 0.03	1.49 ± 0.08	1.56 ± 0.04
24612	2" circle	1.68 ± 0.01	13.90 ± 0.10	2.15 ± 0.04	4.72 ± 0.04	1.52 ± 0.03	9.75 ± 0.10
	0.5" annulus	1.95 ± 0.02	6.76 ± 0.06	2.57 ± 0.05	2.80 ± 0.03	1.61 ± 0.04	4.38 ± 0.06
	1.0" annulus	2.27 ± 0.04	1.93 ± 0.03	3.16 ± 0.09	0.99 ± 0.02	1.78 ± 0.09	1.15 ± 0.03
	grade 0	2.34 ± 0.03	2.85 ± 0.04	2.54 ± 0.06	1.54 ± 0.02	1.36 ± 0.07	1.61 ± 0.04

ObsID	Spectra	Γ_{broad}	F_{broad} (10^{-12} erg cm^{-2} s^{-1})	Γ_{low}	F_{low} (10^{-12} erg cm^{-2} s^{-1})	Γ_{high}	F_{high} (10^{-12} erg cm^{-2} s^{-1})
24639	2" circle	1.69 ± 0.01	13.60 ± 0.09	2.19 ± 0.03	4.68 ± 0.04	1.42 ± 0.03	9.54 ± 0.09
	0.5" annulus	1.99 ± 0.02	6.41 ± 0.06	2.61 ± 0.05	2.74 ± 0.03	1.56 ± 0.04	4.13 ± 0.07
	1.0" annulus	2.24 ± 0.04	1.90 ± 0.03	3.11 ± 0.09	0.97 ± 0.02	1.49 ± 0.09	1.16 ± 0.03
	grade 0	2.35 ± 0.03	2.77 ± 0.03	2.57 ± 0.06	1.52 ± 0.02	1.28 ± 0.07	1.57 ± 0.03
24641	2" circle	1.71 ± 0.01	13.20 ± 0.10	2.26 ± 0.04	4.61 ± 0.04	1.50 ± 0.03	9.21 ± 0.09
	0.5" annulus	1.98 ± 0.02	6.21 ± 0.07	2.69 ± 0.06	2.63 ± 0.04	1.59 ± 0.05	4.04 ± 0.06
	1.0" annulus	2.37 ± 0.05	1.73 ± 0.04	3.27 ± 0.11	0.94 ± 0.03	1.74 ± 0.11	0.99 ± 0.03
	grade 0	2.40 ± 0.03	2.75 ± 0.04	2.69 ± 0.07	1.55 ± 0.03	1.31 ± 0.08	1.53 ± 0.04
24661	2" circle	1.69 ± 0.02	13.20 ± 0.16	2.18 ± 0.06	4.54 ± 0.08	1.51 ± 0.05	9.23 ± 0.14
	0.5" annulus	1.99 ± 0.03	6.31 ± 0.12	2.58 ± 0.09	2.67 ± 0.06	1.70 ± 0.08	4.03 ± 0.10
	1.0" annulus	2.26 ± 0.07	1.91 ± 0.07	3.17 ± 0.16	0.98 ± 0.04	1.67 ± 0.17	1.16 ± 0.05
	grade 0	2.42 ± 0.05	2.75 ± 0.07	2.47 ± 0.11	1.53 ± 0.04	1.46 ± 0.12	1.47 ± 0.05

In Figs. 4.7b, 4.7c, and 4.7d, the fluxes have been normalized by a multiplicative constant to allow direct comparisons between the different source extraction regions. We note the remarkable similarity in the overall shape of the light curves regardless of the extraction region, indicating that while the absolute flux measurement is a strong function of extraction region and grade filtering, variability measures should be robust.

4.4 Time Series Analysis

Analysis of X-ray variability has long been key to studying characteristic timescales and structures of AGN. Early studies showed more X-ray luminous sources varied “less”, or more slowly (Barr & Mushotzky, 1986). *EXOSAT* long-look observations permitted the first use of Fourier analysis methods, namely the use of the power spectral density function (PSD), which revealed that most AGN light curves were well-described by red noise variability (Green et al., 1993; Lawrence & Papadakis, 1993). PSDs measure variability power $P(\nu)$ at frequency ν , related to time scale $\tau = 1/\nu$. Studies of high quality AGN PSDs show that they are well-fit on long timescales (low frequency) by a power law slope of -1 which breaks to a steeper slope $\gtrsim -2$ on shorter timescales (higher frequency). The location where the slope changes is referred to as the break frequency ν_{br} or break timescale τ_{br} . The break timescale is of interest since it can be used to probe physically interesting quantities like black hole mass and accretion rate. For example, Turner & Reynolds (2021) have recently examined theoretical models for accretion disk variability based on stochastically varying disk viscosity; they have shown that the break timescale is proportional to black hole mass and also dependent on the driving timescale

for the viscosity variability.

While PSD analysis is the ideal method for measuring characteristic timescales, it requires long, high quality, regular source monitoring which is only available for a few dozen objects. Given the nature of typical astronomical observations, other methods like fractional variability (excess variance) and structure functions are used instead. Below we employ both methods in the study of the *Chandra* X-ray light curve of H1821+643.

4.4.1 Fractional Variability

We calculate the fractional variability F_{var} , a common estimate of the intrinsic source variability that accounts for measurement error (Edelson et al. 2001, 2002; Nandra et al. 1997; Vaughan et al. 2003). The fractional variability is the square root of the normalized excess variance σ_{NXS}^2 , or the measured variability amplitude, which is also the integral of the PSD over a frequency window defined by the length and binning of the light curve. The two measures contain the same information but F_{var} is a linear statistic which gives the rms variability amplitude as a percentage, thus the choice of which to use is often stylistic (Vaughan et al., 2003). Taking the number of observations (N) of flux x_i each with $1\text{-}\sigma$ measurement uncertainty $\sigma_{\text{err},i}$, we calculate fractional variability

$$F_{\text{var}} = \sqrt{\sigma_{\text{NXS}}^2} = \sqrt{\frac{S^2 - \overline{\sigma_{\text{err}}^2}}{\bar{x}^2}}. \quad (4.1)$$

where $\overline{\sigma_{\text{err}}^2}$ is the mean square error defined as

$$\overline{\sigma_{\text{err}}^2} = \frac{1}{N} \sum_{i=1}^N \sigma_{\text{err},i}^2 \quad (4.2)$$

and S^2 is the sample variance defined as

$$S^2 = \frac{1}{N-1} \sum_{i=1}^N (\bar{x} - x_i)^2. \quad (4.3)$$

The appropriate uncertainty on σ_{NXS}^2 for observations with Poisson measurement errors is given by [Vaughan et al. \(2003\)](#) as

$$\text{err}(\sigma_{\text{NXS}}^2) = \sqrt{\left(\sqrt{\frac{2}{N}} \cdot \frac{\sigma_{\text{err}}^2}{\bar{x}^2}\right)^2 + \left(\sqrt{\frac{\sigma_{\text{err}}^2}{N}} \cdot \frac{2F_{\text{var}}}{\bar{x}}\right)^2}. \quad (4.4)$$

By extension, the uncertainty on F_{var} is given by [Poutanen et al. \(2008\)](#) as

$$\text{err}(F_{\text{var}}) = \sqrt{F_{\text{var}}^2 + \text{err}(\sigma_{\text{NXS}}^2)} - F_{\text{var}}. \quad (4.5)$$

Calculated values of F_{var} for each light curve corresponding to the three source extraction region and grade filtered spectra are given in [Table 4.3](#). We find the high energy band does vary slightly more than the soft band overall. This is not overly surprising given that the high energy band is dominated by the quasar which we would expect to vary more than the surrounding cluster which dominates the soft band.

Flux measurements from the 1.0''-2.0'' annular source region vary noticeably more than the other three spectra (orange lines in [Fig. 4.7](#)). First order analytic descriptions of ‘pileup fraction’ provided by the [CXC ABC Guide to Pileup \(2010\)](#) show that both the mean count rate and the fractional rms variability of a piled up light curve is decreased by a factor of $(1-\beta\Lambda)$ where $\beta \equiv (2-\alpha)/2$ as compared to the expected fractional rms of the

Table 4.3: Fractional variability for the three source extraction region and grade 0 spectra.

Spectral Extraction	$F_{\text{var},\text{broad}} (\%)$	$F_{\text{var},\text{low}} (\%)$	$F_{\text{var},\text{high}} (\%)$
2'' circle	6.70 ± 0.15	5.07 ± 0.20	7.51 ± 0.21
0.5''-2.0 annulus	6.59 ± 0.23	5.95 ± 0.28	6.89 ± 0.34
1.0''-2.0 annulus	9.40 ± 0.43	9.74 ± 0.52	9.14 ± 0.65
2'' circle, grade 0	5.12 ± 0.31	4.18 ± 0.35	5.79 ± 0.51

unpiled light curve. The analytic treatment of pileup fraction takes α to be an empirically determined grade migration parameter and Λ to be the counts per detector region per frame time *in the absence of pileup*. While α and Λ are not explicitly known, this first order treatment reveals that beyond reducing the mean count rate, pileup suppresses both positive and negative fluctuations about the mean. Given that the 1.0''-2.0'' annular source region removes the majority of piled up events, it is less susceptible to suppressed fractional variability. While the grade 0 spectrum also removes piled up events, it contains significantly more calibration uncertainties and particle background events (see §4.2.2.1) which likely propagate to the fractional variability measure.

4.4.2 Structure Function

The structure function (SF) is the Fourier transform of the PSD and provides another quantitative way of characterizing a light curve by exploring the range of time scales that contribute to the variability of a source. Initially adapted for use with astronomical data by [Simonetti et al. \(1985\)](#), the SF is now a popular measurement for AGN variability in the radio, optical, UV, and X-ray. The SF is advantageous given its suitability for unevenly and/or sparsely sampled data sets. One drawback, however, is the difficulty of assessing and interpreting relevant errors. The primary time scale of interest returned by

the SF is τ_{br} , the location at which the SF flattens and plateaus, considered a characteristic timescale beyond which variations are uncorrelated (see e.g. [Hughes et al. 1992](#)). τ_{br} in the SF is equivalent to $1/\nu_{\text{br}}$ measured in the PSD. We use the following definition of the structure function ([de Vries et al., 2003](#); [Hawkins, 2002](#)):

$$SF(\tau) = \left\{ \frac{1}{N(\tau)} \sum_{i < j} [m(t_j) - m(t_i)]^2 \right\}^{1/2} \quad (4.6)$$

where $m(t)$ is the flux at time t with the summation over all possible measurement pairs N for which $\tau = t_j - t_i$. If the light curve has n flux measurements, we form $n(n - 1)/2$ measurement pairs which we bin logarithmically in τ to calculate the SF. Below, we define k as the number of bins and N as the number of measurement pairs in a given bin. While the error of the estimated SF in each bin is ill-defined ([Emmanoulopoulos et al., 2010](#)), we approximate the error from the central limit theorem as

$$\sigma_{SF}(\tau) = \frac{SF(\tau)}{\sqrt{N}} \quad (4.7)$$

To assess the characteristic time t_{br} , we fit the SF with a simple model of the form

$$SF_{\text{mod}}(\tau) = A \left(\frac{(\tau/\tau_{\text{br}})^\alpha}{1 + (\tau/\tau_{\text{br}})^\alpha} \right). \quad (4.8)$$

such that $SF(\tau) \propto \tau^\alpha$ for small τ and plateaus to a constant for $\tau \gg \tau_{\text{br}}$. We choose to fit our SF model defined in Eq. 4.8 to our calculated structure functions in log-space taking $X(\tau) = \log_{10}(SF)$ and $\sigma_X(\tau) = \log_{10}(SF + \sigma_{SF}) - \log_{10}(SF)$. Converting to

log-space, we define our model SF as

$$M(\tau) = \log_{10}(SF_{mod}) = \log_{10}(A) + \log_{10}\left(\frac{(\tau/\tau_{br})^\alpha}{1 + (\tau/\tau_{br})^\alpha}\right) = \lambda + \beta. \quad (4.9)$$

To find the best-fitting model parameters, we minimize the χ^2 function defined by

$$\chi^2 = \sum_{i=1}^k \frac{(X - M)^2}{\sigma_X^2} = \sum_{i=1}^k \frac{(X - \beta - \lambda)^2}{\sigma_X^2}. \quad (4.10)$$

For a given α and τ_0 , β is specified. The value of λ which minimizes the χ^2 function can be found by setting $\delta\chi^2/\delta\lambda = 0$, which yields

$$\lambda = \frac{\sum_{i=1}^k \frac{X}{\sigma_X^2} - \sum_{i=1}^k \frac{\beta}{\sigma_X^2}}{\sum_{i=1}^k \frac{1}{\sigma_X^2}}. \quad (4.11)$$

We use the above χ^2 minimization to determine τ_{br} and α for structure functions calculated for the high energy light curves using the 0.5''-2.0'' annular and 2.0'' circular source extraction regions (Fig. 4.8a and 4.8c). The estimated SF with best fit is shown in Fig. 4.8b and 4.8d. With 1- σ error ranges, we find best fit values for the 0.5''-2.0'' annular source region of $\tau_{br} = 7.05^{+10.54}_{-2.93}$ days and $\alpha = 1.06^{+0.44}_{-0.38}$. For the 2.0'' circular source extraction, we find $\tau_{br} = 6.63^{+4.85}_{-2.42}$ days and $\alpha = 1.24^{+0.42}_{-0.34}$. We note that these values, especially τ_{br} , are less tightly constrained at the 90% level. Structure function analysis of the other light curves did not provide constrained measures of τ_{br} , which we attribute the decreased signal to noise in the 1.0''-2.0'' annular source region and 2'' circular source region filtered for grade 0 events. Interpretations of these results are discussed in §4.6.3.

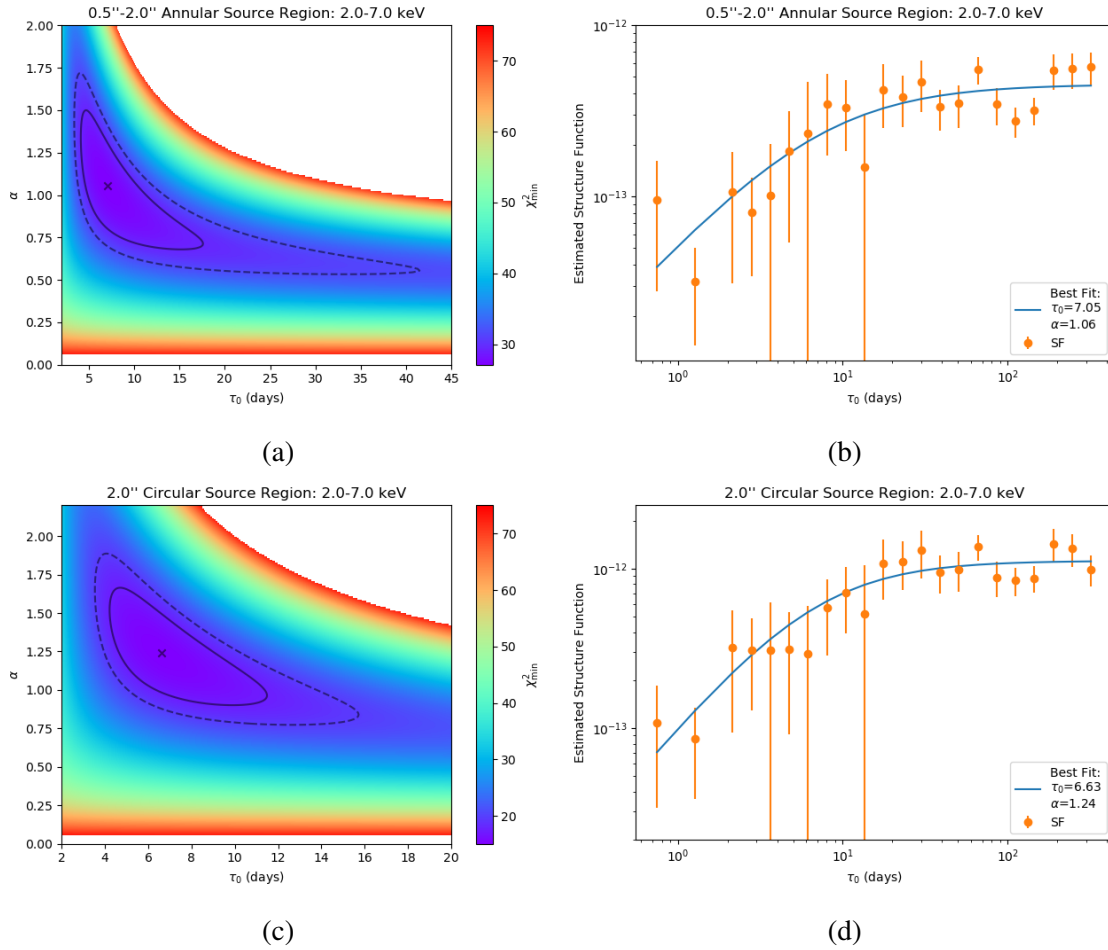


Figure 4.8: Structure function analysis of the high energy (2.0-7.0 keV) light curves with the 0.5''-2.0'' annular and 2.0'' circular source regions. In axis labels, τ_0 is τ_{br} . (a) and (c) show the results of a two parameter χ^2 minimization. The 'x' marks the χ^2 minimum, the solid and dashed lines indicate the 1- σ and 90% errors respectively. (b) and (d) show the resulting structure functions with best fits.

4.5 Spectral Analysis

We conduct a detailed spectral analysis of H1821+643 using the combined time-averaged spectrum with the 2'' circular source extraction region. Although the most heavily piled of the spectra, we must include the full extraction in order to utilize the existing XSPEC pileup⁴ spectral model. We explored spectral fitting with the annular source extraction regions, and although the pileup is much reduced (see Fig. 4.4), model residuals revealed hard tails which impact the continuum modeling. Given that the pileup is mild, the use of the pileup model was the best choice for obtaining robust results. The pileup model, however, assumes that the center of the PSF has not been removed, thus rendering our annular source regions inappropriate.

Spectral analysis was performed using XSPEC version 12.10.0c (Arnaud, 1996a). Best fits were found using the Cash statistic (C-statistic; Cash 1979) appropriate for Poisson distributed data. The spectrum was fit between 2-10 keV in the source rest frame ($z = 0.299$), and errors on model parameters are given at a $1-\sigma$ level.

We begin building our spectral model by starting with a basic single power law with Galactic absorption, then adding the pileup model. The pileup model is based on the analytic treatment of pileup presented in Davis (2001), and takes into account the frame time of the observations, the maximum number of photons to pileup, the event grade correction, the event grade morphing parameter, PSF fraction, the number of regions, and the FRACEXPO keyword. The frame time (`fr_time`) and maximum number of photons (`max_ph`) are set by the user, and should remain fixed. We set `max_ph=10`, the middle

⁴<https://heasarc.gsfc.nasa.gov/xanadu/xspec/manual/XSmodelPileup.html>

value between the minimum and maximum allowed by the model. We have verified that our results are insensitive to this choice. The grade correction (g) and morphing parameter (α) address the effects of grade migration, and the good grade fraction is assumed to be proportional to $\alpha^{(\text{max-ph}-1)}$. The grade correction is frozen at the default value of 1.0 while α is left as a free parameter. The PSF fraction is the fraction of counts in the source extraction region which are from the point source whose pile-up is being modeled, which is *not* the same as the fraction of the PSF included in the source extraction region. The model only works as intended when the source extraction region contains most of the PSF. This parameter is frozen at 0.95, the default value. The number of regions gives the number of regions to independently pile up, which we freeze at the appropriate and default value of 1. Finally, the FRACEXPO keyword is frozen at the value of the keyword given in the ARF.

Comparison of the residuals from the power law models without and with the pileup model (Fig. 4.9 a,b) reveals the drastic improvement of the continuum modeling above 7 keV when the pileup model is included (Δ C-stat = 1214). The initial power law fit without pileup correction is $\Gamma = 1.48 \pm 0.006$, quite low given the canonical photon index for AGN is $\Gamma \sim 2$ (see e.g. Turner & Pounds 1989, Mushotzky et al. 1993, Reeves & Turner 2000) and much lower than previously published measurements (§4.1.0.1). The inclusion of the pileup model results in $\Gamma = 1.7 \pm 0.01$, more in line with what we would expect. Next, we add a Gaussian line to model the iron $K\alpha$ emission. We find a narrow but unresolved line centered at $E = 6.405 \pm 0.02$ keV (rest frame) with a width of $\sigma = 0.06^{+0.03}_{-0.05}$ keV. This also greatly improves the fit of the model (Δ C-stat = 84). All model parameters are given in Table 4.5.

Motivated by the form of the remaining residuals and the recent work of Sisk-Reynés et al. (2022b, submitted), we next construct a model including relativistic reflection from the inner accretion disk using the *relxill* model (Dauser et al., 2014; García et al., 2014). This is the standard relativistic reflection model which models the irradiation of the accretion disk from above by an X-ray corona. We employ the `relxilllp` variant of this model which assumes that the X-ray corona has a ‘lamp post’ geometry, residing above the disk on the spin-axis of the black hole. The parameters of this model include: (1) h , the height of the corona in R_g , (2) a , the dimensionless spin of the black hole, (3) i , the inclination with respect to the normal to the accretion disk, (4) R_{in} , the inner radius of the accretion disk, (5) R_{out} , the outer radius of the accretion disk, (6) z , the cosmological redshift of the source, (7) Γ , the photon index of the primary continuum, (8) $\log \xi$, the ionization parameter of the accretion disk, (9) A_{Fe} , the iron abundance of the accretion disk, (10) E_{cut} , the observed high energy cutoff of the incident spectrum, (11) the reflection fraction (`refl_frac`), and (12) a model switch controlling the reflection fraction calculation (`fixReflFrac`). We freeze the inner edge of the disk to be the innermost stable circular orbit (ISCO). The outer radius is set to $400 r_g$, but the fit is very insensitive to this choice. We allow the reflection fraction to fit freely, rather than be set to the self-consistent value, by setting the parameter `fixReflFrac` = 0.

We find that the model is not sensitive to the spin parameter. Left to freely vary, it is pegged at the hard lower limit of the model $a = -0.998$, a maximum retrograde spin. Recent study by Sisk-Reynés et al. (2022, submitted) of the higher quality *Chandra* LETG and HETG grating observations from 2001 find a spin parameter $a = 0.62^{+0.22}_{-0.37}$ (90% errors). Given the quality of our data, we do not find fits with maximum retrograde

spin credible. In exploring the spin parameter space, we find a noticeable, albeit not statistically significant, local minimum in the C-statistic with a spin parameter $a = 0.7$. The spin parameter is in good agreement with previous findings so we choose to freeze the spin parameter at $a = 0.7$ in order to better constrain remaining model parameters.

Model parameters from our best fitting model are presented in Table 2.5. We find that the inclination of the disk is constrained at the $1\text{-}\sigma$ level at $i = 51.8^\circ \pm 10.4^\circ$, in good agreement with Reynolds et al. (2014) and Sisk-Reynés et al. (2022b, submitted) who find $i \sim 57^\circ$ and $i \sim 41^\circ - 56^\circ$, respectively. Our model provides tight constraints on the photon index, $\Gamma = 1.9 \pm 0.02$, well in line with previously published measurements. The ionization parameter is defined as $\xi = L_{\text{ion}}/(n_e R^2)$ where L_{ion} is the ionizing luminosity from 1-1000 Ryd, n_e is electron density, and R is the distance of the illuminated gas from the ionizing source. We find $\log \xi = 2.7_{-0.27}^{+0.07}$, which is higher than found by Reynolds et al. (2014) but consistent with Sisk-Reynés et al. (2022b, submitted) who finds an upper limit of $\log \xi \lesssim 3.07$ when modeling the HETG data. We find an approximately solar iron abundance, which is interesting given multiple previous publications reporting sub-solar abundances for the accretion disk Reynolds et al. (2014) and sub-solar estimates for the surrounding ICM (Russell et al., 2010). Finally, we find that the model is not sensitive to the height of the corona. The model prefers $h \sim 33 R_g$, but subsequent evaluations with `steppar` where the C-statistic of the model is evaluated over a range of fixed values of h do not yield any constraints on the value.

Included in this model is a Gaussian emission line for the iron $K\alpha$ emission from cold, slowly moving gas further from the central region. Our model well constrains the energy of the line at $E = 6.399 \pm 0.024$ keV (rest frame). The width of the line is

$\sigma = 0.06_{-0.05}^{+0.03}$ keV. The parameters of the iron line are nearly identical in the power law model and the relativistic reflection model, demonstrating the robustness of these values. The energy of the line is consistent with modern X-ray observations.

The discrepancies in ionization parameter and iron abundance with [Reynolds et al. \(2014\)](#) can be partially attributed to appreciable updates in the `relxill` package in the last several years which have been shown to impact abundance measurements. Additionally, the PSF of the `textitSuzaku` observations presented in [Reynolds et al. \(2014\)](#) does not allow for rigorous separation of the ICM and AGN, thus the measurement of the ionization parameter is wholly dependent on the ability to disentangle the line emission in the iron band. The modeling process was further complicated by gain shifts caused by poor calibration. We do not consider our results in tension with those of [Reynolds et al. \(2014\)](#) given the reasons stated above likely affect the robustness of their detailed conclusions.

Overall, modeling the spectrum of H1821+643 with a relativistic reflection and a Gaussian emission line improves the overall fit of the model (Δ C-stat = 105). Visually, we note the improved residuals between panels (c) and (d) in Fig. 4.9. Residuals in the power law models show curvature in the continuum below 7 keV with noticeable excess around 3 keV and deficit around 5.5 keV. While the relativistic reflection model does not perfectly address these deviations, it is significantly improved.

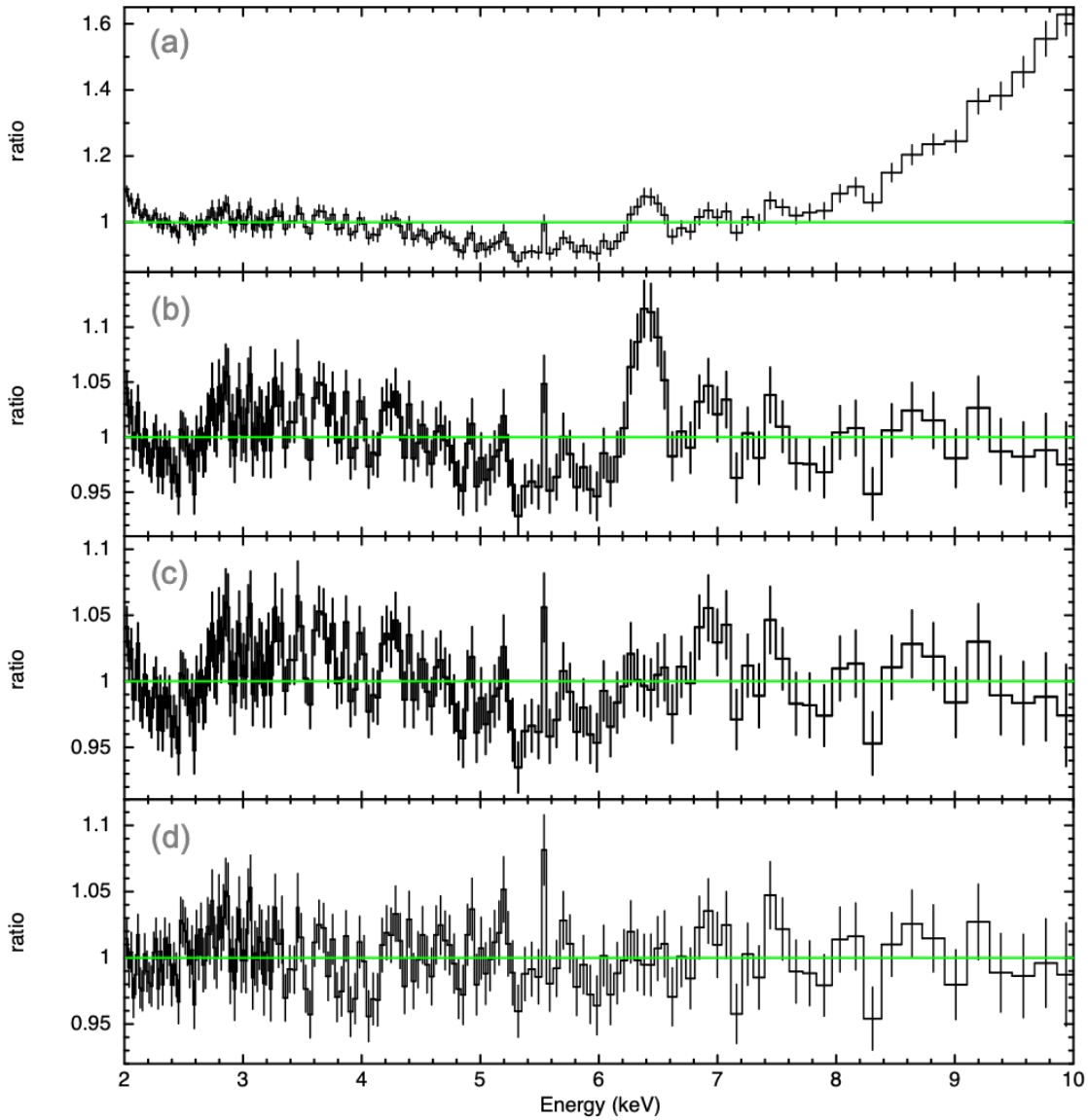


Figure 4.9: Data to model ratios for spectral models fit to the 2'' circular source region combined spectrum. Energies are plotted in the rest frame ($z = 0.299$) and have been rebinned for visual purposes. (a) A single power law with Galactic absorption. The pronounced excess above 7 keV is indicative of pileup. (b) The model applied in (a) with the addition of the XSPEC pileup model which well-models the excess above 7 keV. (c) The model in (b) now including a Gaussian emission line to model the 6.4 keV iron $K\alpha$ emission line. (d) The combined spectrum fit with the pileup model, Gaussian emission line, and relativistic reflection with *relxill*. While high energy residuals are similar to those in (c), the curvature in the continuum from 2-7 keV is better modeled.

Table 4.4: Best-fitting model parameters for models including pileup, a single power law, and a Gaussian emission line. Models are fit to the combined 2'' circular source region spectrum. The inclusion of the pileup model addresses the hard tail (Fig 4.9) and results in a more reasonable photon index $\Gamma = 1.7$. The iron emission line is centered at 6.4 keV (rest frame), the expected energy of the neutral or low-ionization iron $K\alpha$ line.

Model Component	Parameter	Unit	Value	C-statistic	Δ C-statistic
TBabs powerlaw	N_{H}^{a}	10^{22}	0.035		
	Γ		1.48 ± 0.006	1857.97	...
	norm		$2.5 \times 10^{-3} \pm 1.7 \times 10^{-5}$		
pileup	fr_time ^a	s	0.3		
	max_ph ^a		10.0		
	g0 ^a	1.0			
	α		0.206 ± 0.006		
	psfrac ^a		0.95	643.95	1214.02
	nregions ^a	(scale)	1.0		
	fracexpo ^a	(scale)	1.0		
TBabs powerlaw	N_{H}^{a}	10^{22}	0.035		
	Γ		1.69 ± 0.01		
	norm		$5.3 \times 10^{-2} \pm 6 \times 10^{-4}$		
pileup	fr_time ^a	s	0.3		
	max_ph		10.0 ^a		
	g0 ^a	1.0			
	α		0.209 ± 0.006		
	psfrac ^a		0.95		
	nregions ^a	(scale)	1.0		
	fracexpo ^a	(scale)	1.0	559.77	84.18
TBabs powerlaw	N_{H}^{a}	10^{22}	0.035		
	Γ		1.70 ± 0.01		
	norm		$5.3 \times 10^{-2} \pm 6 \times 10^{-4}$		
zgauss	LineE	keV	6.405 ± 0.02		
	σ	keV	$0.06^{+0.03}_{-0.05}$		
	z^{a}		0.299		
	norm		$1.4 \times 10^{-4} \pm 3 \times 10^{-5}$		

^a Parameters frozen at their stated values.

Table 4.5: Best-fitting relativistic reflection model parameters to the 2'' circular source combined spectrum. The photon index Γ of the quasar is consistent with previously published values. While the model is not sensitive to spin (a) or the height of the corona (h), we find that the inclination of the disk (i), ionization parameter ($\log \xi$), iron abundance (A_{Fe}), and reflection fraction are well-constrained at the 1- σ level.

Model Component	Parameter	Unit	Value	C-statistic	Δ C-statistic
pileup	fr_time ^a	s	0.3		
	max_ph ^a		10.0		
	g0 ^a	1.0			
	α		0.59 ± 0.04		
	psfrac ^a		0.95		
	nregions ^a	(scale)	1.0		
	fracexpo ^a	(scale)	1.0		
TBabs	N_{H} ^a	10^{22}	0.035		
zgauss	LineE	keV	6.399 ± 0.024		
	σ	keV	$0.06^{+0.03}_{-0.06}$		
relxill	z^{a}		0.299		
	norm		$1.2 \times 10^{-5} \pm 3 \times 10^{-6}$	454.67	105.1 ^b
	h^{c}	GM/c^2	32.98		
	a^{a}		0.70		
	i	deg	51.84 ± 10.4		
	R_{in} ^a	R_{ISCO}	-1.0		
	R_{out} ^a	R_{g}	400.0		
	z^{a}		0.299		
	Γ		1.924 ± 0.015		
	$\log \xi$		$2.70^{+0.07}_{-0.27}$		
	A_{Fe}		$1.01^{+1.18}_{-0.28}$		
	E_{cut} ^a	keV	300.0		
refl_frac		$1.00^{+0.47}_{-0.36}$			
fixReflFrac ^a		0.0			
norm		$(1.06 \times 10^{-4})^{+1.9 \times 10^{-5}}_{-1.2 \times 10^{-5}}$			

^a Parameters frozen at their stated values.

^b Compared to last model in Table 4.5

^c Model is not sensitive to this parameter. Stated values reflect the best-fitting model's preferred value, but are not statistically significant.

4.6 Discussion

4.6.1 Variability

We observe that the flux of H1821+643 can vary modestly on timescales of order 5-10 days. It is useful to compare this to the light crossing time of the black hole, $t_{\text{cross}} = GM/c^3 = 4.9 \times 10^{-6} (M_{\text{BH}}/M_{\odot})$ seconds. If we place the inner accretion disk at a radius of $\sim 20R_g$ and assume a black hole mass for H1821+643 of $1-3 \times 10^9 M_{\odot}$ (see §4.6.3), then $t_{\text{cross}} \sim 1 - 3.5$ days. Thus the high-cadence nature of our new *Chandra* observations reveals that this source is in fact varying on timescales nearly as short as physically possible.

4.6.2 Source Stability

Spectral analysis of new *Chandra* ACIS-S imaging data provide the first well-isolated spectrum of H1821+643 in ~ 20 years. While we find modest flux variability over course on one year, the overall spectral properties of H1821+643 have remained remarkably constant. This finding is important to underpin future observing proposals of H1821+643 with upcoming missions.

4.6.3 Black Hole Mass Estimates

The SMBH in H1821+643 is thought to be one of the most massive in the local universe. Some of our most reliable methods of black hole mass estimates (i.e. stellar kinematics and water masers) are not technically feasible for an object at this distance.

Shapovalova et al. (2016) does find a black hole mass estimate of $M_{\text{BH}} \sim 2.6 \times 10^9 M_{\odot}$ using reverberation mapping of the $\text{H}\beta$ emission line. Historically, however, many other methods have been used to estimate the SMBH mass. Kolman et al. (1991) use a turnover on the high frequency side of the UV SED to constrain a thin accretion disk model assuming a nonrotating black hole which provides an estimate of $M_{\text{BH}} = (3 \pm 0.5) \times 10^9 M_{\odot}$. Using *Hubble Space Telescope* observations and the $M_{\text{BH}} - L_{\text{bulge}}$ relation (see e.g. McLure & Dunlop 2002), Floyd et al. (2004) report estimates of $M_{\text{BH}} = 2.46 \times 10^9 M_{\odot}$.

A common method for estimating black hole mass utilizes optical/UV emission linewidths and the optical/UV continuum luminosity as proxies for the velocity and size of the broad line region, thus allowing the mass to be estimated from the virial theorem, $M_{\text{BH}} = R_{\text{BLR}} V^2 / G$ (see McGill et al. 2008 for a summary scaling relationships). Kim et al. (2008), Russell et al. (2010), and Capellupo et al. (2017) find virial mass estimates of $M_{\text{BH}} = 1.2 \times 10^9 M_{\odot}$, $M_{\text{BH}} \sim 3 \times 10^9 M_{\odot}$, and $M_{\text{BH}} \sim 2.5 \times 10^9 M_{\text{BH}}$, respectively. Extending the virial argument to the narrow line region and IR emission lines, Dasyra et al. (2011) estimate $M_{\text{BH}} = (1.2 \pm 0.62) \times 10^9 M_{\odot}$. Walker et al. (2014) lay out a theoretical framework which permits the SMBH in H1821+643 to reach an enormous mass of $M_{\text{BH}} \sim 3 \times 10^{10} M_{\odot}$. Using their best-fitting relativistic reflection model, Reynolds et al. (2014) estimate the Eddington luminosity and use that to estimate $M_{\text{BH}} \sim 3 - 6 \times 10^9 M_{\text{BH}}$.

Empirically, the characteristic break timescale of the PSD increases with increasing black hole mass (Markowitz et al. 2003, Papadakis 2004, McHardy et al. 2006, González-Martín & Vaughan 2012). In most published scaling relationships, mass depends only on τ_{br} . McHardy et al. (2006), however, explores an additional dependence on the mass

accretion rate by using bolometric luminosity as a proxy. In Table 4.6, we compile multiple published scaling relationships between τ_{br} and M_{BH} and use those to estimate the mass of the black hole in H1821+643 assuming $\tau_{\text{br}} \sim 7$ days, a rough average of the value found in our structure functions in §4.4.2.

Using these scaling relationships yields somewhat lower mass estimates for the SMBH compared to other published estimates for H1821+643. We note several factors that could explain the difference. First, these relationships are derived using narrow and broad line Seyfert 1 galaxies with a strong preference with those with reverberation mapped mass measurements available. As a consequence, the relationships are derived using only 10-20 sources with few, if any, having masses greater than $10^8 M_{\odot}$. Given the highly unusual nature of H1821+643, it is not surprising it may not fall on the same relationship as that of Seyfert 1 AGN. Additionally, efforts to derive a $\tau_{\text{br}}-M_{\text{BH}}$ relationship are often interested in using the measure as a way to connect Galactic black holes with SMBH. The inclusion of such low mass systems ($10-100 M_{\odot}$) without inclusion of high mass ($\gtrsim 10^8 M_{\text{BH}}$) systems could skew the relationship in such a way that it does not provide a good fit for high mass systems. Regardless, applying $\tau_{\text{br}}-M_{\text{BH}}$ scaling relationships to provide another way to compare H1821+643 with more typical AGN.

There is also a well-documented anticorrelation between excess variance and black hole mass; σ_{NXS}^2 decreases with increasing M_{BH} (Bian & Zhao, 2003; Lu & Yu, 2001; McHardy, 2010; O’Neill et al., 2005; Papadakis, 2004; Ponti et al., 2012). Since excess variance can be calculated for large samples of objects, these relationships are likely more appropriate to apply to H1821+643. The existing literature, however, derive the $\sigma_{\text{NXS}}^2-M_{\text{BH}}$ relation using short light curves (10, 20, 40, or 80 ks) evenly binned to ~ 250 s.

Table 4.6: We compile published $\tau_{\text{br}}-M_{\text{BH}}$ scaling relationships and use them to estimate the black hole mass for H1821+643 using $\tau_{\text{br}} \sim 7$ days (§4.4.2). The units of the black hole mass in solar mass is denoted by the subscript (e.g. $M_{\text{BH},6}$ is mass units of $10^6 M_{\odot}$). The bolometric luminosity is in units of 10^{44} erg s $^{-1}$. We find black hole mass estimates for H1821+643 that are much smaller than previously published values. We largely attribute this discrepancy to the samples used to derive the scaling relationship, which are small and comprised of Seyfert 1 galaxies.

References: (1) [Markowitz et al. 2003](#), (2) [Papadakis 2004](#), (3) [McHardy et al. 2006](#), and (4) [González-Martín & Vaughan 2012](#).

Ref	$\tau_{\text{br}} - M_{\text{BH}}$ Relationship	M_{BH} Estimate
(1)	$\tau_{\text{br,days}} = M_{\text{BH}}/M_{6.5}$	$2.2 \times 10^7 M_{\odot}$
(2)	$\nu_{\text{br}} = C/M_{\text{BH},7}$ $C = 1.7 \times 10^{-6}$ $C = 3.4 \times 10^{-5}$	$1.0 \times 10^7 M_{\odot}$ $2.1 \times 10^8 M_{\odot}$
(3)	$\log(\tau_{\text{br,days}}) = A \log(M_{\text{BH},6}) - B \log(L_{\text{bol},44}) + C$ $A = 2.17^{+0.32}_{-0.25}$ $A = 2.10 \pm 0.15$ $B = 0.90^{+0.3}_{-0.2}$ $B = 0.98 \pm 0.15$ $C = -2.42^{+0.22}_{-0.25}$ $C = -2.32 \pm 0.2$	$7.5 \times 10^8 M_{\odot}$ $1.1 \times 10^9 M_{\odot}$
(4)	$\log(\tau_{\text{br,days}}) = A \log(M_{\text{BH},6}) + C$ $A = 1.09 \pm 0.21$ $C = -1.70 \pm 0.29$ $\log(\tau_{\text{br,days}}) = A \log(M_{\text{BH},6}) - B \log(L_{\text{bol},44}) + C$ $A = 1.34 \pm 0.36$ $B = -0.24 \pm 0.28$ $C = -1.88 \pm 0.36$	$2.2 \times 10^8 M_{\odot}$ $2.8 \times 10^7 M_{\odot}$

While *Chandra* provides unrivaled spatial resolution permitting the separation of the point source and the cluster, it does not provide the signal to noise to produce such light curves. Fractional variability still provides a quantitative measure of the overall variability of H1821+643, but using our measurements with published scaling relationships would not be appropriate. Exploring how H1821+643 fits into these temporal relationships should be included in future study of this object.

4.7 Conclusion

We present new *Chandra* observations of the highly unusual quasar H1821+643 residing in the BCG of a cool-core cluster at a redshift of $z = 0.299$. Our high cadence yearlong campaign reveals modest flux variations on the order of 5-10 days which roughly corresponds to the light crossing time for the inner accretion disk. The fractional variability finds that the higher energies vary slightly more than the lower energies. Calculation of the structure function yields a characteristic timescale of ~ 7 days. Spectral analysis of the combined time-averaged spectra reveal the neutral iron $K\alpha$ and photon index of $\Gamma \sim 1.9$, in good agreement with previously published values. Additionally, our best fit strongly requires relativistic reflection from the inner accretion disk. This is the first observation in ~ 20 years to reliably separate the cluster emission from the quasar emission and revealing that the spectral properties of the quasar have remained remarkably constant.

Chapter 5: Conclusions

This thesis presents three case studies of AGN believed to be actively producing feedback processes which impact the evolution of either their host galaxy or their galaxy cluster. Chapter 2 presents evidence from X-ray observations for an ultrafast outflow which could be driving the observed galaxy-scale molecular outflow in the ultraluminous infrared host galaxy IRASF05189-2524. Chapter 3 presents new *Chandra* observations of NGC 1275, the BCG of the Perseus Cluster. Observations reveal rapid variability on intraweek timescales, and using archival X-ray observations, show a general trend to have a harder photon index when brighter. We also find the first robust evidence for highly correlated time-delayed emission where an optical flare leads a γ -ray flare by ~ 5 days. In addition to providing insight into the physical size of the emitting region, this result is suggestive of synchrotron self-Compton producing the observed γ -ray emission. Finally, in Chapter 4, we again present new *Chandra* observations of the very rare, optically luminous, radio-quiet BCG H1821+643. The high-cadence observing campaign reveals rapid variability on timescales of order of the light crossing time of the inner accretion disk. Modeling of the time-averaged spectrum is indicative of relativistic reflection. The overall spectral properties are remarkably consistent with observations taken decades prior.

5.1 Future Prospects

X-ray astronomy has much to look forward to as we anticipate entering the era of microcalorimeter spectroscopy. In contrast to traditional grating spectroscopy, a microcalorimeter absorbs incident X-rays and converts the energy to heat which is then measured to ‘detect’ the photons. This new technology will improve on the energy resolution at $E > 2$ keV of the *Chandra* HETG and permit high-resolution spectroscopy of diffuse systems. The significant increase in energy resolution in the iron-band will open on entirely new areas of study for AGN in X-ray while furthering our understanding of the complex iron line region.

In the spring of 2023, we eagerly anticipate the launch of *Xrism*, a joint endeavor by NASA and JAXA. The microcalorimeter will have an energy resolution of ≤ 7 eV from 0.3-12 keV. *Xrism* will have a spatial resolution of $\sim 1.5'$ and an (energy dependent) effective area ranging from $\sim 160 - 300$ cm². A taste of what to expect may be found in the *Hitomi* Collaboration publications.

We then look to the next decade to the launch of *Athena*, ESA’s large class X-ray telescope targeted to launch in 2034. The microcalorimeter will have an energy resolution of ~ 2 eV from 0.3-12 keV, an enormous (energy dependent) collecting area ranging from 0.25-2 m², and a spatial resolution of $\sim 10''$ or better. The capabilities of *Athena* will truly open new realms of X-ray astronomy enabling imaging and spectroscopy of objects at low flux levels and large distances that are not fathomable with current instrumentation.

Finally, NASA’s 2020 Astrophysics Decadal Survey created a new ‘probe’ class with a budget cap of \$1.5 billion to fill the gap between small Explorer and large Flagship

missions. The survey identified X-ray and far infrared as priorities for the new mission class. With *Chandra* nearing its 23rd year of operation (far beyond its initial expected lifetime of 5 years), the X-ray community is optimistic about probe proposals which would complement *Athena* while maintaining NASA research capabilities at high energies. In particular, *AXIS* is designed with similar energy resolution to *Chandra*, but with six times the effective area and a spatial resolution of $\sim 1''$, 5-10 times better than *Athena*.

Bibliography

- Abdo, A. A., Ackermann, M., Ajello, M., et al. 2009, *ApJ*, 699, 31, doi: 10.1088/0004-637X/699/1/31
- Aleksić, J., Alvarez, E. A., Antonelli, L. A., et al. 2012, *A&A*, 539, L2, doi: 10.1051/0004-6361/201118668
- Aleksić, J., Ansoldi, S., Antonelli, L. A., et al. 2014, *A&A*, 564, A5, doi: 10.1051/0004-6361/201322951
- Allen, S. W., Dunn, R. J. H., Fabian, A. C., Taylor, G. B., & Reynolds, C. S. 2006, *MNRAS*, 372, 21, doi: 10.1111/j.1365-2966.2006.10778.x
- Angel, J. R. P., & Stockman, H. S. 1980, *ARA&A*, 18, 321, doi: 10.1146/annurev.aa.18.090180.001541
- Antonucci, R. 1993, *ARA&A*, 31, 473, doi: 10.1146/annurev.aa.31.090193.002353
- Arnaud, K. A. 1996a, in *Astronomical Society of the Pacific Conference Series*, Vol. 101, *Astronomical Data Analysis Software and Systems V*, ed. G. H. Jacoby & J. Barnes, 17
- Arnaud, K. A. 1996b, in *Astronomical Society of the Pacific Conference Series*, Vol. 101, *Astronomical Data Analysis Software and Systems V*, ed. G. H. Jacoby & J. Barnes, 17
- Arnaud, M. 2009, *A&A*, 500, 103, doi: 10.1051/0004-6361/200912150
- Asada, K., Kamenno, S., Shen, Z.-Q., et al. 2006, *PASJ*, 58, 261, doi: 10.1093/pasj/58.2.261
- Asplund, M., Grevesse, N., Sauval, A. J., & Scott, P. 2009, *ARA&A*, 47, 481, doi: 10.1146/annurev.astro.46.060407.145222
- Astropy Collaboration, Robitaille, T. P., Tollerud, E. J., et al. 2013, *A&A*, 558, A33, doi: 10.1051/0004-6361/201322068
- Astropy Collaboration, Price-Whelan, A. M., Sipőcz, B. M., et al. 2018, *AJ*, 156, 123, doi: 10.3847/1538-3881/aabc4f

- Atwood, W. B., Abdo, A. A., Ackermann, M., et al. 2009, *ApJ*, 697, 1071, doi: 10.1088/0004-637X/697/2/1071
- Ballet, J. 1999, *A&AS*, 135, 371, doi: 10.1051/aas:1999179
- Barr, P., & Mushotzky, R. F. 1986, *Nature*, 320, 421, doi: 10.1038/320421a0
- Beckmann, V., & Shrader, C. 2012, in Proceedings of “An INTEGRAL view of the high-energy sky (the first 10 years)” - 9th INTEGRAL Workshop and celebration of the 10th anniversary of the launch (INTEGRAL 2012). 15-19 October 2012. Bibliotheque Nationale de France, 69
- Bellocchi, E., Arribas, S., Colina, L., & Miralles-Caballero, D. 2013, *A&A*, 557, A59, doi: 10.1051/0004-6361/201221019
- Berg, M., Conlon, J. P., Day, F., et al. 2017, *ApJ*, 847, 101, doi: 10.3847/1538-4357/aa8b16
- Bian, W., & Zhao, Y. 2003, *MNRAS*, 343, 164, doi: 10.1046/j.1365-8711.2003.06650.x
- Bîrzan, L., Rafferty, D. A., McNamara, B. R., Wise, M. W., & Nulsen, P. E. J. 2004, *ApJ*, 607, 800, doi: 10.1086/383519
- Bischetti, M., Piconcelli, E., Feruglio, C., et al. 2019, *A&A*, 628, A118, doi: 10.1051/0004-6361/201935524
- Blundell, K. M., & Rawlings, S. 2001, *ApJL*, 562, L5, doi: 10.1086/337970
- Braito, V., Reeves, J. N., Matzeu, G. A., et al. 2018, *MNRAS*, 479, 3592, doi: 10.1093/mnras/sty1697
- Brown, A. M., & Adams, J. 2011, *MNRAS*, 413, 2785, doi: 10.1111/j.1365-2966.2011.18351.x
- Burns, J. O. 1990, *AJ*, 99, 14, doi: 10.1086/115307
- Burrows, D. N., Hill, J. E., Nousek, J. A., et al. 2005, *SSRv*, 120, 165, doi: 10.1007/s11214-005-5097-2
- Canizares, C. R., Davis, J. E., Dewey, D., et al. 2005, *PASP*, 117, 1144, doi: 10.1086/432898
- Capellupo, D. M., Wafflard-Fernandez, G., & Haggard, D. 2017, *ApJL*, 836, L8, doi: 10.3847/2041-8213/aa5cac
- Cash, W. 1979, *ApJ*, 228, 939, doi: 10.1086/156922
- Cavaliere, A., & Fusco-Femiano, R. 1976, *A&A*, 49, 137

- Chandra X-ray Center. 2021, The *Chandra* Proposers' Observatory Guide, 24.0. <https://cxc.harvard.edu/proposer/POG/html/index.html>
- Chandra X-ray Science Center - Science Data Systems. 2010, The *Chandra* ABC Guide to Pileup, 2.2. https://cxc.harvard.edu/ciao/download/doc/pileup_abc.pdf
- Churazov, E., Forman, W., Jones, C., & Böhringer, H. 2003, *ApJ*, 590, 225, doi: 10.1086/374923
- Cicone, C., Maiolino, R., Sturm, E., et al. 2014, *A&A*, 562, A21, doi: 10.1051/0004-6361/201322464
- Connolly, S. D. 2016, DELightcurveSimulation: Light curve simulation code. <http://ascl.net/1602.012>
- Crenshaw, D. M., & Kraemer, S. B. 2012, *ApJ*, 753, 75, doi: 10.1088/0004-637X/753/1/75
- Crummy, J., Fabian, A. C., Brandt, W. N., & Boller, T. 2005, *MNRAS*, 361, 1197, doi: 10.1111/j.1365-2966.2005.09258.x
- Czerny, B., Nikolajuk, M., Róžańska, A., et al. 2003, *A&A*, 412, 317, doi: 10.1051/0004-6361:20031441
- Dasyra, K. M., Ho, L. C., Netzer, H., et al. 2011, *ApJ*, 740, 94, doi: 10.1088/0004-637X/740/2/94
- Dasyra, K. M., Tacconi, L. J., Davies, R. I., et al. 2006, *ApJ*, 651, 835, doi: 10.1086/507834
- Dauser, T., Garcia, J., Parker, M. L., Fabian, A. C., & Wilms, J. 2014, *MNRAS*, 444, L100, doi: 10.1093/mnrasl/slul25
- Davis, J. E. 2001, *ApJ*, 562, 575, doi: 10.1086/323488
- Davis, J. E., Bautz, M. W., Dewey, D., et al. 2012, in Society of Photo-Optical Instrumentation Engineers (SPIE) Conference Series, Vol. 8443, Space Telescopes and Instrumentation 2012: Ultraviolet to Gamma Ray, ed. T. Takahashi, S. S. Murray, & J.-W. A. den Herder, 84431A
- de Vries, W. H., Becker, R. H., & White, R. L. 2003, *AJ*, 126, 1217, doi: 10.1086/377486
- Di Matteo, T., Springel, V., & Hernquist, L. 2005, *Nature*, 433, 604, doi: 10.1038/nature03335
- Dutson, K. L., Edge, A. C., Hinton, J. A., et al. 2014, *MNRAS*, 442, 2048, doi: 10.1093/mnras/stu975

- Edelson, R., Griffiths, G., Markowitz, A., et al. 2001, *ApJ*, 554, 274, doi: 10.1086/321332
- Edelson, R., Turner, T. J., Pounds, K., et al. 2002, *ApJ*, 568, 610, doi: 10.1086/323779
- Edelson, R. A., & Krolik, J. H. 1988, *ApJ*, 333, 646, doi: 10.1086/166773
- Emmanoulopoulos, D., McHardy, I. M., & Papadakis, I. E. 2013, *MNRAS*, 433, 907, doi: 10.1093/mnras/stt764
- Emmanoulopoulos, D., McHardy, I. M., & Uttley, P. 2010, *MNRAS*, 404, 931, doi: 10.1111/j.1365-2966.2010.16328.x
- Fabian, A. C. 1994, *ARA&A*, 32, 277, doi: 10.1146/annurev.aa.32.090194.001425
- . 1999, *MNRAS*, 308, L39, doi: 10.1046/j.1365-8711.1999.03017.x
- . 2006, *Astronomische Nachrichten*, 327, 943, doi: 10.1002/asna.200610669
- . 2012, *ARA&A*, 50, 455, doi: 10.1146/annurev-astro-081811-125521
- Fabian, A. C., Reynolds, C. S., Taylor, G. B., & Dunn, R. J. H. 2005, *MNRAS*, 363, 891, doi: 10.1111/j.1365-2966.2005.09484.x
- Fabian, A. C., Walker, S. A., Pinto, C., Russell, H. R., & Edge, A. C. 2015, *MNRAS*, 451, 3061, doi: 10.1093/mnras/stv1134
- Fabian, A. C., Sanders, J. S., Ettori, S., et al. 2000, *MNRAS*, 318, L65, doi: 10.1046/j.1365-8711.2000.03904.x
- Fabian, A. C., Sanders, J. S., Allen, S. W., et al. 2011, *MNRAS*, 418, 2154, doi: 10.1111/j.1365-2966.2011.19402.x
- Fang, T., Davis, D. S., Lee, J. C., et al. 2002, *ApJ*, 565, 86, doi: 10.1086/324602
- Faucher-Giguère, C.-A., & Quataert, E. 2012, *MNRAS*, 425, 605, doi: 10.1111/j.1365-2966.2012.21512.x
- Ferrarese, L., & Merritt, D. 2000, *ApJL*, 539, L9, doi: 10.1086/312838
- Feruglio, C., Fiore, F., Carniani, S., et al. 2015, *A&A*, 583, A99, doi: 10.1051/0004-6361/201526020
- Feruglio, C., Ferrara, A., Bischetti, M., et al. 2017, *A&A*, 608, A30, doi: 10.1051/0004-6361/201731387
- Fiore, F., Feruglio, C., Shankar, F., et al. 2017, *A&A*, 601, A143, doi: 10.1051/0004-6361/201629478

- Floyd, D. J. E., Kukula, M. J., Dunlop, J. S., et al. 2004, *MNRAS*, 355, 196, doi: 10.1111/j.1365-2966.2004.08315.x
- Fluetsch, A., Maiolino, R., Carniani, S., et al. 2019, *MNRAS*, 483, 4586, doi: 10.1093/mnras/sty3449
- Freeman, P., Doe, S., & Siemiginowska, A. 2001, in *Society of Photo-Optical Instrumentation Engineers (SPIE) Conference Series*, Vol. 4477, *Astronomical Data Analysis*, ed. J.-L. Starck & F. D. Murtagh, 76–87
- Freyberg, M. J., Briel, U. G., Dennerl, K., et al. 2004, in *Society of Photo-Optical Instrumentation Engineers (SPIE) Conference Series*, Vol. 5165, *X-Ray and Gamma-Ray Instrumentation for Astronomy XIII*, ed. K. A. Flanagan & O. H. W. Siegmund, 112–122
- Fruscione, A., McDowell, J. C., Allen, G. E., et al. 2006, in *Society of Photo-Optical Instrumentation Engineers (SPIE) Conference Series*, Vol. 6270, *Society of Photo-Optical Instrumentation Engineers (SPIE) Conference Series*, ed. D. R. Silva & R. E. Doxsey, 62701V
- Fukazawa, Y., Shiki, K., Tanaka, Y., et al. 2018, *ApJ*, 855, 93, doi: 10.3847/1538-4357/aaabc0
- García, J., Dauser, T., Lohfink, A., et al. 2014, *ApJ*, 782, 76, doi: 10.1088/0004-637X/782/2/76
- García-Burillo, S., Combes, F., Usero, A., et al. 2014, *A&A*, 567, A125, doi: 10.1051/0004-6361/201423843
- Gaspari, M., Brighenti, F., D’Ercole, A., & Melioli, C. 2011, *MNRAS*, 415, 1549, doi: 10.1111/j.1365-2966.2011.18806.x
- Gaspari, M., Ruszkowski, M., & Oh, S. P. 2013, *MNRAS*, 432, 3401, doi: 10.1093/mnras/stt692
- Gaspari, M., Temi, P., & Brighenti, F. 2017, *MNRAS*, 466, 677, doi: 10.1093/mnras/stw3108
- Gebhardt, K., Bender, R., Bower, G., et al. 2000, *ApJL*, 539, L13, doi: 10.1086/312840
- Gehrels, N., Chincarini, G., Giommi, P., et al. 2004, *ApJ*, 611, 1005, doi: 10.1086/422091
- Ghez, A. M., Morris, M., Becklin, E. E., Tanner, A., & Kremenek, T. 2000, *Nature*, 407, 349, doi: 10.1038/35030032
- Gierliński, M., & Done, C. 2004, *MNRAS*, 349, L7, doi: 10.1111/j.1365-2966.2004.07687.x

- Giovannini, G., Savolainen, T., Orienti, M., et al. 2018, *Nature Astronomy*, 2, 472, doi: 10.1038/s41550-018-0431-2
- Gofford, J., Reeves, J. N., McLaughlin, D. E., et al. 2015, *MNRAS*, 451, 4169, doi: 10.1093/mnras/stv1207
- Gofford, J., Reeves, J. N., Tombesi, F., et al. 2013, *MNRAS*, 430, 60, doi: 10.1093/mnras/sts481
- González-Alfonso, E., Fischer, J., Spoon, H. W. W., et al. 2017, *ApJ*, 836, 11, doi: 10.3847/1538-4357/836/1/11
- González-Martín, O., & Vaughan, S. 2012, *A&A*, 544, A80, doi: 10.1051/0004-6361/201219008
- Graham, J., Fabian, A. C., & Sanders, J. S. 2008, *MNRAS*, 386, 278, doi: 10.1111/j.1365-2966.2008.13027.x
- Gravity Collaboration, Abuter, R., Aymar, N., et al. 2022, *A&A*, 657, L12, doi: 10.1051/0004-6361/202142465
- Green, A. R., McHardy, I. M., & Lehto, H. J. 1993, *MNRAS*, 265, 664, doi: 10.1093/mnras/265.3.664
- Gu, M., & Cao, X. 2009, *MNRAS*, 399, 349, doi: 10.1111/j.1365-2966.2009.15277.x
- Hall, P. B., Ellingson, E., & Green, R. F. 1997, *AJ*, 113, 1179, doi: 10.1086/118336
- Harris, C. R., Millman, K. J., van der Walt, S. J., et al. 2020, *Nature*, 585, 357, doi: 10.1038/s41586-020-2649-2
- Hawkins, M. R. S. 2002, *MNRAS*, 329, 76, doi: 10.1046/j.1365-8711.2002.04939.x
- Heinz, S., Choi, Y.-Y., Reynolds, C. S., & Begelman, M. C. 2002, *ApJL*, 569, L79, doi: 10.1086/340688
- Henden, A., & Munari, U. 2014, *Contributions of the Astronomical Observatory Skalnaté Pleso*, 43, 518
- Hitomi Collaboration, Aharonian, F., Akamatsu, H., et al. 2016, *Nature*, 535, 117, doi: 10.1038/nature18627
- . 2018, *PASJ*, 70, 13, doi: 10.1093/pasj/psx147
- Ho, L. C., Filippenko, A. V., & Sargent, W. L. W. 1997, *ApJS*, 112, 315, doi: 10.1086/313041
- Hodgson, J. A., Rani, B., Lee, S.-S., et al. 2018, *MNRAS*, 475, 368, doi: 10.1093/mnras/stx3041

- Hodgson, J. A., Rani, B., Oh, J., et al. 2021, *ApJ*, 914, 43, doi: 10.3847/1538-4357/abf6dd
- Hopkins, P. F., & Elvis, M. 2010, *MNRAS*, 401, 7, doi: 10.1111/j.1365-2966.2009.15643.x
- Hopkins, P. F., Hernquist, L., Cox, T. J., et al. 2006, *ApJS*, 163, 1, doi: 10.1086/499298
- Hopkins, P. F., Torrey, P., Faucher-Giguère, C.-A., Quataert, E., & Murray, N. 2016, *MNRAS*, 458, 816, doi: 10.1093/mnras/stw289
- Hudson, D. S., Mittal, R., Reiprich, T. H., et al. 2010, *A&A*, 513, A37, doi: 10.1051/0004-6361/200912377
- Hughes, P. A., Aller, H. D., & Aller, M. F. 1992, *ApJ*, 396, 469, doi: 10.1086/171734
- Hunter, J. D. 2007, *Computing in Science & Engineering*, 9, 90, doi: 10.1109/MCSE.2007.55
- Hutchings, J. B., & Neff, S. G. 1991, *AJ*, 101, 2001, doi: 10.1086/115824
- Imazato, F., Fukazawa, Y., Sasada, M., & Sakamoto, T. 2021, *ApJ*, 906, 30, doi: 10.3847/1538-4357/abc7bc
- Ishibashi, W., Fabian, A. C., & Maiolino, R. 2018, *MNRAS*, 476, 512, doi: 10.1093/mnras/sty236
- Jiménez-Bailón, E., Santos-Lleó, M., Piconcelli, E., et al. 2007, *A&A*, 461, 917, doi: 10.1051/0004-6361:20065566
- Joye, W. A., & Mandel, E. 2003, in *Astronomical Society of the Pacific Conference Series*, Vol. 295, *Astronomical Data Analysis Software and Systems XII*, ed. H. E. Payne, R. I. Jedrzejewski, & R. N. Hook, 489
- Kalberla, P. M. W., Burton, W. B., Hartmann, D., et al. 2005, *A&A*, 440, 775, doi: 10.1051/0004-6361:20041864
- Kallman, T., & Bautista, M. 2001, *ApJS*, 133, 221, doi: 10.1086/319184
- Kallman, T. R., Palmeri, P., Bautista, M. A., Mendoza, C., & Krolik, J. H. 2004, *ApJS*, 155, 675, doi: 10.1086/424039
- Kardashev, N. S., Khartov, V. V., Abramov, V. V., et al. 2013, *Astronomy Reports*, 57, 153, doi: 10.1134/S1063772913030025
- Kataoka, J., Stawarz, Ł., Cheung, C. C., et al. 2010, *ApJ*, 715, 554, doi: 10.1088/0004-637X/715/1/554
- Kii, T., Williams, O. R., Ohashi, T., et al. 1991, *ApJ*, 367, 455, doi: 10.1086/169641

Kim, M., Ho, L. C., Peng, C. Y., et al. 2008, *ApJ*, 687, 767, doi: 10.1086/591663

King, A. 2003, *ApJL*, 596, L27, doi: 10.1086/379143

King, A., & Pounds, K. 2015, *ARA&A*, 53, 115, doi: 10.1146/annurev-astro-082214-122316

King, A. R., & Pounds, K. A. 2003, *MNRAS*, 345, 657, doi: 10.1046/j.1365-8711.2003.06980.x

Kino, M., Ito, H., Wajima, K., et al. 2017, *ApJ*, 843, 82, doi: 10.3847/1538-4357/aa7336

Kino, M., Wajima, K., Kawakatu, N., et al. 2018, *ApJ*, 864, 118, doi: 10.3847/1538-4357/aad6e3

Kochanek, C. S., Shappee, B. J., Stanek, K. Z., et al. 2017, *PASP*, 129, 104502, doi: 10.1088/1538-3873/aa80d9

Kolman, M., Halpern, J. P., Shrader, C. R., & Filippenko, A. V. 1991, *ApJ*, 373, 57, doi: 10.1086/170022

Kormendy, J., & Richstone, D. 1995, *ARA&A*, 33, 581, doi: 10.1146/annurev.aa.33.090195.003053

Koss, M., Mushotzky, R., Baumgartner, W., et al. 2013, *ApJL*, 765, L26, doi: 10.1088/2041-8205/765/2/L26

Krichbaum, T. P., Witzel, A., Graham, D. A., et al. 1992, *A&A*, 260, 33

Lacy, M., Rawlings, S., & Hill, G. J. 1992, *MNRAS*, 258, 828, doi: 10.1093/mnras/258.4.828

Lacy, M., Ridgway, S., & Trentham, N. 2002, *NewAR*, 46, 211, doi: 10.1016/S1387-6473(01)00182-8

Laha, S., Reynolds, C. S., Reeves, J., et al. 2021, *Nature Astronomy*, 5, 13, doi: 10.1038/s41550-020-01255-2

Lawrence, A., & Papadakis, I. 1993, *ApJL*, 414, L85, doi: 10.1086/187002

Li, J., Kastner, J. H., Prigozhin, G. Y., et al. 2004, *ApJ*, 610, 1204, doi: 10.1086/421866

Liu, H., Pinto, C., Fabian, A. C., Russell, H. R., & Sanders, J. S. 2019, *MNRAS*, 485, 1757, doi: 10.1093/mnras/stz456

Longinotti, A. L., Krongold, Y., Guainazzi, M., et al. 2015, *ApJL*, 813, L39, doi: 10.1088/2041-8205/813/2/L39

- Lott, B., Escande, L., Larsson, S., & Ballet, J. 2012, *A&A*, 544, A6, doi: 10.1051/0004-6361/201218873
- Lu, Y., & Yu, Q. 2001, *MNRAS*, 324, 653, doi: 10.1046/j.1365-8711.2001.04344.x
- Luminari, A., Piconcelli, E., Tombesi, F., et al. 2018, *A&A*, 619, A149, doi: 10.1051/0004-6361/201833623
- Markowitz, A., Edelson, R., Vaughan, S., et al. 2003, *ApJ*, 593, 96, doi: 10.1086/375330
- Marr, J. M., Backer, D. C., Wright, M. C. H., Readhead, A. C. S., & Moore, R. 1989, *ApJ*, 337, 671, doi: 10.1086/167138
- Marshall, F. E., Boldt, E. A., Holt, S. S., et al. 1979, *ApJS*, 40, 657, doi: 10.1086/190600
- Mattox, J. R., Bertsch, D. L., Chiang, J., et al. 1996, *ApJ*, 461, 396, doi: 10.1086/177068
- Matzeu, G. A., Reeves, J. N., Nardini, E., et al. 2016, *MNRAS*, 458, 1311, doi: 10.1093/mnras/stw354
- McConnell, N. J., & Ma, C.-P. 2013, *ApJ*, 764, 184, doi: 10.1088/0004-637X/764/2/184
- McDonald, M., Allen, S. W., Bayliss, M., et al. 2017, *ApJ*, 843, 28, doi: 10.3847/1538-4357/aa7740
- McGill, K. L., Woo, J.-H., Treu, T., & Malkan, M. A. 2008, *ApJ*, 673, 703, doi: 10.1086/524349
- McHardy, I. 2010, in *Lecture Notes in Physics*, Berlin Springer Verlag, ed. T. Belloni, Vol. 794, 203
- McHardy, I. M., Koerding, E., Knigge, C., Uttley, P., & Fender, R. P. 2006, *Nature*, 444, 730, doi: 10.1038/nature05389
- McLure, R. J., & Dunlop, J. S. 2002, *MNRAS*, 331, 795, doi: 10.1046/j.1365-8711.2002.05236.x
- Miller, J. M., Bautz, M. W., & McNamara, B. R. 2017, *ApJL*, 850, L3, doi: 10.3847/2041-8213/aa9566
- Million, E. T., Werner, N., Simionescu, A., et al. 2010, *MNRAS*, 407, 2046, doi: 10.1111/j.1365-2966.2010.17220.x
- Mirzoyan, R. 2016, *The Astronomer's Telegram*, 9689, 1

- . 2017, *The Astronomer's Telegram*, 9929, 1
- Mizumoto, M., Izumi, T., & Kohno, K. 2019, *ApJ*, 871, 156, doi: 10.3847/1538-4357/aaf814
- Mukai, K. 1993, *Legacy*, 3, 21
- Mukherjee, R., & VERITAS Collaboration. 2016, *The Astronomer's Telegram*, 9690, 1
- . 2017, *The Astronomer's Telegram*, 9931, 1
- Mushotzky, R. F., Done, C., & Pounds, K. A. 1993, *ARA&A*, 31, 717, doi: 10.1146/annurev.aa.31.090193.003441
- Nagai, H., Chida, H., Kino, M., et al. 2016, *Astronomische Nachrichten*, 337, 69, doi: 10.1002/asna.201512267
- Nagai, H., Suzuki, K., Asada, K., et al. 2010, *PASJ*, 62, L11, doi: 10.1093/pasj/62.2.L11
- Nagai, H., Haga, T., Giovannini, G., et al. 2014, *ApJ*, 785, 53, doi: 10.1088/0004-637X/785/1/53
- Nagai, H., Onishi, K., Kawakatu, N., et al. 2019, *ApJ*, 883, 193, doi: 10.3847/1538-4357/ab3e6e
- Nandra, K., George, I. M., Mushotzky, R. F., Turner, T. J., & Yaqoob, T. 1997, *ApJ*, 476, 70, doi: 10.1086/303600
- Nandra, K., & Pounds, K. A. 1994, *MNRAS*, 268, 405, doi: 10.1093/mnras/268.2.405
- Nardini, E., Wang, J., Fabbiano, G., et al. 2013, *ApJ*, 765, 141, doi: 10.1088/0004-637X/765/2/141
- Nardini, E., Reeves, J. N., Gofford, J., et al. 2015, *Science*, 347, 860, doi: 10.1126/science.1259202
- NASA High Energy Astrophysics Science Archive Research Center. 2014, HEASoft: Unified Release of FTOOLS and XANADU, Astrophysics Source Code Library, record ascl:1408.004. <http://ascl.net/1408.004>
- Netzer, H. 2015, *ARA&A*, 53, 365, doi: 10.1146/annurev-astro-082214-122302
- Nugent, J. J., Jensen, K. A., Nousek, J. A., et al. 1983, *ApJS*, 51, 1, doi: 10.1086/190838
- O'Neill, P. M., Nandra, K., Papadakis, I. E., & Turner, T. J. 2005, *MNRAS*, 358, 1405, doi: 10.1111/j.1365-2966.2005.08860.x

- O'Sullivan, E., Giacintucci, S., Babul, A., et al. 2012, MNRAS, 424, 2971, doi: 10.1111/j.1365-2966.2012.21459.x
- Padovani, P., Alexander, D. M., Assef, R. J., et al. 2017, A&A Rv, 25, 2, doi: 10.1007/s00159-017-0102-9
- Paggi, A., Fabbiano, G., Risaliti, G., et al. 2017, ApJ, 841, 44, doi: 10.3847/1538-4357/aa713b
- Papadakis, I. E. 2004, MNRAS, 348, 207, doi: 10.1111/j.1365-2966.2004.07351.x
- Parker, M. L., Pinto, C., Fabian, A. C., et al. 2017, Nature, 543, 83, doi: 10.1038/nature21385
- Patrick, A. R., Reeves, J. N., Porquet, D., et al. 2012, MNRAS, 426, 2522, doi: 10.1111/j.1365-2966.2012.21868.x
- Pauliny-Toth, I. I. K., Preuss, E., Witzel, A., et al. 1976, Nature, 259, 17, doi: 10.1038/259017a0
- Pedlar, A., Booler, R. V., & Davies, R. D. 1983, MNRAS, 203, 667, doi: 10.1093/mnras/203.3.667
- Pedlar, A., Ghataure, H. S., Davies, R. D., et al. 1990, MNRAS, 246, 477
- Peterson, J. R., & Fabian, A. C. 2006, PhR, 427, 1, doi: 10.1016/j.physrep.2005.12.007
- Ponti, G., Papadakis, I., Bianchi, S., et al. 2012, A&A, 542, A83, doi: 10.1051/0004-6361/201118326
- Poutanen, J., Zdziarski, A. A., & Ibragimov, A. 2008, MNRAS, 389, 1427, doi: 10.1111/j.1365-2966.2008.13666.x
- Pravdo, S. H., & Marshall, F. E. 1984, ApJ, 281, 570, doi: 10.1086/162131
- Pronik, I. I., Merkulova, N. I., & Metik, L. P. 1999, A&A, 351, 21
- Ptak, A., Heckman, T., Levenson, N. A., Weaver, K., & Strickland, D. 2003, ApJ, 592, 782, doi: 10.1086/375766
- Readhead, A. C. S., Hough, D. H., Ewing, M. S., Walker, R. C., & Romney, J. D. 1983a, ApJ, 265, 107, doi: 10.1086/160657
- Readhead, A. C. S., Mason, C. R., Mofett, A. T., et al. 1983b, Nature, 303, 504, doi: 10.1038/303504a0
- Reeves, J. N., & Turner, M. J. L. 2000, MNRAS, 316, 234, doi: 10.1046/j.1365-8711.2000.03510.x

- Reimer, O., Pohl, M., Sreekumar, P., & Mattox, J. R. 2003, *ApJ*, 588, 155, doi: 10.1086/374046
- Remillard, R. A., & McClintock, J. E. 2006, *ARA&A*, 44, 49, doi: 10.1146/annurev.astro.44.051905.092532
- Reynolds, C. S. 1997, *MNRAS*, 286, 513, doi: 10.1093/mnras/286.3.513
- Reynolds, C. S., Lohfink, A. M., Babul, A., et al. 2014, *ApJL*, 792, L41, doi: 10.1088/2041-8205/792/2/L41
- Reynolds, C. S., Marsh, M. C. D., Russell, H. R., et al. 2020, *ApJ*, 890, 59, doi: 10.3847/1538-4357/ab6a0c
- Reynolds, C. S., Smith, R. N., Fabian, A. C., et al. 2021, *MNRAS*, 507, 5613, doi: 10.1093/mnras/stab2507
- Richings, A. J., & Faucher-Giguère, C.-A. 2018, *MNRAS*, 478, 3100, doi: 10.1093/mnras/sty1285
- Riffel, R. A., Storchi-Bergmann, T., Zakamska, N. L., & Riffel, R. 2020, *MNRAS*, 496, 4857, doi: 10.1093/mnras/staa1922
- Risaliti, G., Gilli, R., Maiolino, R., & Salvati, M. 2000, *A&A*, 357, 13. <https://arxiv.org/abs/astro-ph/0002460>
- Robertson, D. R. S., Gallo, L. C., Zoghbi, A., & Fabian, A. C. 2015, *MNRAS*, 453, 3455, doi: 10.1093/mnras/stv1575
- Rothberg, B., Fischer, J., Rodrigues, M., & Sanders, D. B. 2013, *ApJ*, 767, 72, doi: 10.1088/0004-637X/767/1/72
- Rupke, D. S., Veilleux, S., & Sanders, D. B. 2005, *ApJ*, 632, 751, doi: 10.1086/444451
- Rupke, D. S. N., Gültekin, K., & Veilleux, S. 2017, *ApJ*, 850, 40, doi: 10.3847/1538-4357/aa94d1
- Rupke, D. S. N., & Veilleux, S. 2013, *ApJ*, 768, 75, doi: 10.1088/0004-637X/768/1/75
- Russell, H. R., Fabian, A. C., Sanders, J. S., et al. 2010, *MNRAS*, 402, 1561, doi: 10.1111/j.1365-2966.2009.16027.x
- Sanders, D. B., Soifer, B. T., Elias, J. H., et al. 1988, *ApJ*, 325, 74, doi: 10.1086/165983
- Saxton, R. D., Barstow, M. A., Turner, M. J. L., et al. 1997, *MNRAS*, 289, 196, doi: 10.1093/mnras/289.1.196

- Scharwächter, J., McGregor, P. J., Dopita, M. A., & Beck, T. L. 2013, MNRAS, 429, 2315, doi: 10.1093/mnras/sts502
- Schmidt, M. 1963, Nature, 197, 1040, doi: 10.1038/1971040a0
- Schneider, D. P., Bahcall, J. N., Gunn, J. E., & Dressler, A. 1992, AJ, 103, 1047, doi: 10.1086/116122
- Severgnini, P., Risaliti, G., Marconi, A., Maiolino, R., & Salvati, M. 2001, A&A, 368, 44, doi: 10.1051/0004-6361:20000522
- Seyfert, C. K. 1943, ApJ, 97, 28, doi: 10.1086/144488
- Shapovalova, A. I., Popović, L. Č., Chavushyan, V. H., et al. 2016, ApJS, 222, 25, doi: 10.3847/0067-0049/222/2/25
- Shappee, B. J., Prieto, J. L., Grupe, D., et al. 2014, ApJ, 788, 48, doi: 10.1088/0004-637X/788/1/48
- Silk, J., & Rees, M. J. 1998, A&A, 331, L1. <https://arxiv.org/abs/astro-ph/9801013>
- Simionescu, A., Allen, S. W., Mantz, A., et al. 2011, Science, 331, 1576, doi: 10.1126/science.1200331
- Simonetti, J. H., Cordes, J. M., & Heeschen, D. S. 1985, ApJ, 296, 46, doi: 10.1086/163418
- Sisk-Reynés, J., Matthews, J. H., Reynolds, C. S., et al. 2022, MNRAS, 510, 1264, doi: 10.1093/mnras/stab3464
- Smith, R. N., Tombesi, F., Veilleux, S., Lohfink, A. M., & Luminari, A. 2019, ApJ, 887, 69, doi: 10.3847/1538-4357/ab4ef8
- Sobolewska, M. A., & Papadakis, I. E. 2009, MNRAS, 399, 1597, doi: 10.1111/j.1365-2966.2009.15382.x
- Strong, A. W., & Bignami, G. F. 1983, ApJ, 274, 549, doi: 10.1086/161469
- Sturm, E., González-Alfonso, E., Veilleux, S., et al. 2011, ApJL, 733, L16, doi: 10.1088/2041-8205/733/1/L16
- Suzuki, K., Nagai, H., Kino, M., et al. 2012, ApJ, 746, 140, doi: 10.1088/0004-637X/746/2/140
- Tarter, C. B., Tucker, W. H., & Salpeter, E. E. 1969, ApJ, 156, 943, doi: 10.1086/150026
- Teng, S. H., Veilleux, S., & Baker, A. J. 2013, ApJ, 765, 95, doi: 10.1088/0004-637X/765/2/95

- Teng, S. H., Veilleux, S., Anabuki, N., et al. 2009, *ApJ*, 691, 261, doi: 10.1088/0004-637X/691/1/261
- Teng, S. H., Rigby, J. R., Stern, D., et al. 2015, *ApJ*, 814, 56, doi: 10.1088/0004-637X/814/1/56
- Tombesi, F., & Cappi, M. 2014, *MNRAS*, 443, L104, doi: 10.1093/mnrasl/slu091
- Tombesi, F., Cappi, M., Reeves, J. N., & Braito, V. 2012, *MNRAS*, 422, L1, doi: 10.1111/j.1745-3933.2012.01221.x
- Tombesi, F., Cappi, M., Reeves, J. N., et al. 2013, *MNRAS*, 430, 1102, doi: 10.1093/mnras/sts692
- . 2011, *ApJ*, 742, 44, doi: 10.1088/0004-637X/742/1/44
- . 2010, *A&A*, 521, A57, doi: 10.1051/0004-6361/200913440
- Tombesi, F., Meléndez, M., Veilleux, S., et al. 2015, *Nature*, 519, 436, doi: 10.1038/nature14261
- Tombesi, F., Veilleux, S., Meléndez, M., et al. 2017, *ApJ*, 850, 151, doi: 10.3847/1538-4357/aa9579
- Tremaine, S., Gebhardt, K., Bender, R., et al. 2002, *ApJ*, 574, 740, doi: 10.1086/341002
- Turner, S. G. D., & Reynolds, C. S. 2021, *MNRAS*, 504, 469, doi: 10.1093/mnras/stab875
- Turner, T. J., & Pounds, K. A. 1989, *MNRAS*, 240, 833, doi: 10.1093/mnras/240.4.833
- Unwin, S. C., Mutel, R. L., Phillips, R. B., & Linfield, R. P. 1982, *ApJ*, 256, 83, doi: 10.1086/159885
- Urry, C. M., & Padovani, P. 1995, *PASP*, 107, 803, doi: 10.1086/133630
- Uttley, P., & Mchardy, I. M. 2004, *Progress of Theoretical Physics Supplement*, 155, 170, doi: 10.1143/PTPS.155.170
- Vaughan, S. 2005, *A&A*, 431, 391, doi: 10.1051/0004-6361:20041453
- Vaughan, S., Edelson, R., Warwick, R. S., & Uttley, P. 2003, *MNRAS*, 345, 1271, doi: 10.1046/j.1365-2966.2003.07042.x
- Veilleux, S., Bolatto, A., Tombesi, F., et al. 2017, *ApJ*, 843, 18, doi: 10.3847/1538-4357/aa767d
- Veilleux, S., Cecil, G., & Bland-Hawthorn, J. 2005, *ARA&A*, 43, 769, doi: 10.1146/annurev.astro.43.072103.150610

- Veilleux, S., Kim, D. C., & Sanders, D. B. 1999a, *ApJ*, 522, 113, doi: 10.1086/307634
- . 2002, *ApJS*, 143, 315, doi: 10.1086/343844
- Veilleux, S., Sanders, D. B., & Kim, D. C. 1999b, *ApJ*, 522, 139, doi: 10.1086/307635
- Veilleux, S., Teng, S. H., Rupke, D. S. N., Maiolino, R., & Sturm, E. 2014, *ApJ*, 790, 116, doi: 10.1088/0004-637X/790/2/116
- Veilleux, S., Kim, D. C., Peng, C. Y., et al. 2006, *ApJ*, 643, 707, doi: 10.1086/503188
- Veilleux, S., Rupke, D. S. N., Kim, D. C., et al. 2009a, *ApJS*, 182, 628, doi: 10.1088/0067-0049/182/2/628
- Veilleux, S., Kim, D. C., Rupke, D. S. N., et al. 2009b, *ApJ*, 701, 587, doi: 10.1088/0004-637X/701/1/587
- Veilleux, S., Meléndez, M., Sturm, E., et al. 2013, *ApJ*, 776, 27, doi: 10.1088/0004-637X/776/1/27
- Vermeulen, R. C., Readhead, A. C. S., & Backer, D. C. 1994, *ApJL*, 430, L41, doi: 10.1086/187433
- Véron-Cetty, M. P., & Véron, P. 2010, *A&A*, 518, A10, doi: 10.1051/0004-6361/201014188
- Virtanen, P., Gommers, R., Oliphant, T. E., et al. 2020, *Nature Methods*, 17, 261, doi: 10.1038/s41592-019-0686-2
- Wagner, A. Y., Bicknell, G. V., & Umemura, M. 2012, *ApJ*, 757, 136, doi: 10.1088/0004-637X/757/2/136
- Wagner, A. Y., Umemura, M., & Bicknell, G. V. 2013, *ApJL*, 763, L18, doi: 10.1088/2041-8205/763/1/L18
- Walker, R. C., Dhawan, V., Romney, J. D., Kellermann, K. I., & Vermeulen, R. C. 2000, *ApJ*, 530, 233, doi: 10.1086/308372
- Walker, R. C., Romney, J. D., & Benson, J. M. 1994, *ApJL*, 430, L45, doi: 10.1086/187434
- Walker, S. A., Fabian, A. C., Russell, H. R., & Sanders, J. S. 2014, *MNRAS*, 442, 2809, doi: 10.1093/mnras/stu1067
- Walton, D. J., Nardini, E., Fabian, A. C., Gallo, L. C., & Reis, R. C. 2013, *MNRAS*, 428, 2901, doi: 10.1093/mnras/sts227
- Warwick, R. S., Barstow, M. A., & Yaqoob, T. 1989, *MNRAS*, 238, 917, doi: 10.1093/mnras/238.3.917

- Westmoquette, M. S., Clements, D. L., Bendo, G. J., & Khan, S. A. 2012, *MNRAS*, 424, 416, doi: 10.1111/j.1365-2966.2012.21214.x
- White, D. A., Jones, C., & Forman, W. 1997, *MNRAS*, 292, 419, doi: 10.1093/mnras/292.2.419
- Wilman, R. J., Edge, A. C., & Johnstone, R. M. 2005, *MNRAS*, 359, 755, doi: 10.1111/j.1365-2966.2005.08956.x
- Wilms, J., Allen, A., & McCray, R. 2000, *ApJ*, 542, 914, doi: 10.1086/317016
- Wilson, A. S., & Colbert, E. J. M. 1995, *ApJ*, 438, 62, doi: 10.1086/175054
- Wolter, H. 1952a, *Annalen der Physik*, 445, 94, doi: 10.1002/andp.19524450108
- . 1952b, *Annalen der Physik*, 445, 286, doi: 10.1002/andp.19524450410
- Wright, M. C. H., Backer, D. C., Carlstrom, J. E., et al. 1988, *ApJL*, 329, L61, doi: 10.1086/185177
- Xu, Y., Baloković, M., Walton, D. J., et al. 2017, *ApJ*, 837, 21, doi: 10.3847/1538-4357/aa5df4
- Yamashita, A., Matsumoto, C., Ishida, M., et al. 1997, *ApJ*, 486, 763, doi: 10.1086/304554
- Yaqoob, T., & Serlemitsos, P. 2005, *ApJ*, 623, 112, doi: 10.1086/428432
- Yaqoob, T., Serlemitsos, P. J., Mushotzky, R. F., et al. 1993, *ApJ*, 418, 638, doi: 10.1086/173423
- Younes, G., Porquet, D., Sabra, B., & Reeves, J. N. 2011, *A&A*, 530, A149, doi: 10.1051/0004-6361/201116806
- Zhang, D., & Davis, S. W. 2017, *ApJ*, 839, 54, doi: 10.3847/1538-4357/aa6935
- Zhuravleva, I., Churazov, E., Schekochihin, A. A., et al. 2014, *Nature*, 515, 85, doi: 10.1038/nature13830
- Zubovas, K., & King, A. 2012, *ApJL*, 745, L34, doi: 10.1088/2041-8205/745/2/L34